*eXPRESS Polymer Letters Vol.3, No.12 (2009) 752*
*Available online at www.expresspolymlett.com*
*DOI: 10.3144/expresspolymlett.2009.93*

# Editorial corner – a personal view

## Plastics' key role in energy-efficient building

*P. Krawczak*[*]

Department of Polymers and Composites Technology & Mechanical Engineering, Ecole des Mines de Douai, 941 rue Charles Bourseul, BP 10838, 59508 DOUAI, France

Plastics-based solutions are widespread in the building industry, as the benefits they brought are multiple: insulation, protection from wind and weather, easy refurbishment, attractive new design or efficient energy management.

Plastic pipes for heating and water have proved to be superior to conventional piping systems (more flexible, rust-free, anti-scale deposits, etc.) for a long time. Window frame profiles made of polyvinyl chloride (PVC), one of the most widely used plastic in building industry, provide better thermal insulation, making them suitable for use in passive houses as the energy consumption is reduced dramatically. Other polymer systems may also improve energy management for façades, walls and roofs. Composites or sandwich elements made of expanded polystyrene (EPS) filled with graphite particles or polyurethane (PU) rigid foams are used on walls or on roofs, as well as below the ceiling to provide climatic regulation. The surface of front doors, window frames and façades can be coated with UV-resistant acrylonitrile styrene acrylate (ASA) films so as to guarantee long-term protection against weathering. Roof glazing with thermal protection made of polymethyl methacrylate (PMMA) or polycarbonate (PC) multi-wall sheets enables interior spaces to stay pleasantly cool without having to dispense with daylight, and reduces the cost for heating and cooling.

Moreover, as the solar heating market is steadily growing, the very promising field of large area, light-weight organic photovoltaic panels has emerged for plastics. Polyvinyl fluoride (PVF) films have been used successfully for the backsheet of photovoltaic modules thanks to their weather and UV-resistance, and high barrier properties against moisture. Light-resistant thermoplastic polyurethanes (TPU) are expected to permit to switch from batch-manufacturing to continuous production, lowering expenses accordingly. Furthermore, new efficient manufacturing methods for large-surface modules on flexible low-cost substrates are under development. Finally, intensive research efforts are currently going on into semiconducting organic materials with high thermal and photochemical resistance, which are intended to replace today's silicon, whereby they absorb sunlight and convert it into electric power.

At last, organic Phase Change Materials (PCM) such as HDPE or paraffin compounds provide a new horizon for passive thermal energy storage in bioclimatic architecture, and will contribute to make buildings even more energy-efficient in the future.

Prof. Dr. Patricia Krawczak
Member of International Advisory Board

---

[*]Corresponding author, e-mail: krawczak@ensm-douai.fr

*eXPRESS Polymer Letters Vol.3, No.12 (2009) 753–768*
*Available online at www.expresspolymlett.com*
*DOI: 10.3144/expresspolymlett.2009.94*

# Experimental and theoretical studies of agglomeration effects in multi-walled carbon nanotube-polycarbonate melts

*S. Richter*[1]*, M. Saphiannikova**[1]*, D. Jehnichen*[1]*, M. Bierdel*[2]*, G. Heinrich*[1]

[1]Leibniz Institute of Polymer Research, Hohe Str. 6, 01069 Dresden, Germany
[2]Bayer Technology Services GmbH, 51368 Leverkusen, Germany

*Received 7 July 2009; accepted in revised form 2 September 2009*

**Abstract.** In this study we report on morphological and rheological characterization of multi-walled carbon nanotube (MWNT)-polycarbonate composites produced by injection molding. The main focus is to carry out nonlinear viscoelastic experiments that allow following the structural rearrangements of carbon nanotubes in the polycarbonate melt. Small angle X-ray scattering reveals only a slight orientation of MWNTs in the as-received samples, i.e. after application of extremely high shear rates. Thus, the main structural effect observed during the stress growth experiment is the breakage of MWNT agglomerates. To study this effect in detail a flocculation experiment, in which the sample undergoes oscillatory deformation first at a small strain amplitude in the linear regime succeeded by higher amplitudes in the nonlinear regime, has been carried out. The agglomeration process manifests itself in an increase of the storage and loss moduli in the linear regime, whereas the deagglomeration process does vice versa. The corresponding effects can be described in the frame of a superposition approach that takes into account the stress contribution of the polycarbonate matrix, the hydrodynamic reinforcement due to embedded nanotubes and the viscoelastic stress due to the presence of a MWNT-network.

***Keywords:*** *nanocomposites, rheology, modeling*

## 1. Introduction

In the last two decades, polymer nanocomposites have drawn serious attention both from industry and academic research. On the one hand, significant improvements in various properties at low filler concentration are very attractive to industry. On the other hand, researchers show growing interest in studying the influence of nanoscopic filler particles on thermal, electrical and mechanical properties of the composites [1].

A theoretical description of the viscoelastic properties of filled polymer melts represents a great challenge. Here, one must take into account that most filler particles possess an active surface, tend to build agglomerates and at high loadings even a network-like superstructure [2–4]. This network is very fragile and can be easily broken in external flow fields. However, in the quiescent state the filler particles agglomerate again and restore slowly a network superstructure. Additionally to the agglomeration process, one observes noticeable orientation effects, as the particles of interest are highly anisometric and thus tend to orient along the flow direction [5, 6]. The process of orientation is partly reversible because in the quiescent state the filler particles slowly return towards an isotropic orientation state. It is important to note that both agglomeration and orientation processes have much shorter relaxation times in the presence of flow than in the quiescent state [7].

---

*Corresponding author, e-mail: grenzer@ipfdd.de

Recently, we proposed a superposition approach for description of the viscoelastic properties of low density polyethylene nanocomposites filled with layered double hydroxide particles [8]. In that study the total stress was represented by a superposition of the viscoelastic stress arising in the hydrodynamically reinforced polymer matrix and a stress contribution due to the presence of filler network structure. In the present paper we report on the first attempts to apply the superposition approach to polycarbonate (PC) filled with multi-walled carbon nanotubes (MWNTs). All rheological measurements were carried out with samples produced by injection molding technique at Bayer AG (Germany).

Taking into account excluded volume interactions, the overlap concentration for nanotubes with the persistence length of about 1 µm is estimated to be 0.005 volume fraction (1 wt%) which is in agreement with the experiment [9]. Above the overlap concentration, one obtains a semidilute solution of increasingly entangled nanotubes, i.e. a highly elastic network structure. The boundary between dilute and semidilute regimes is often referred in the literature as the rheological percolation threshold [10]. It is well-known that low values of percolation threshold can be found only in the case of a good dispersion of carbon nanotubes (CNTs) in a polymer matrix. One simple way to control the quality of dispersion is to measure the frequency dependence of storage modulus [3]. Already nanocomposites with 2 wt% of well-dispersed CNTs exhibit a low-frequency plateau which extends to higher frequencies with further increase of CNT concentration. This plateau was observed in other, at first sight, quite different systems including filled polymer melts [11, 12], molecular glasses [13] and colloidal suspensions [14]. In all these systems, the particles interact with each other attractively, which causes a non-equilibrium transition from a liquid-like to a solid-like state at high particles densities.

To gain insight into the physics of this process, we have undertaken a relatively simple nonlinear viscoelastic investigation, herein after referred to as the flocculation experiment. In this experiment the structural changes in the filled polymer melt are followed by measuring the time evolution of storage and loss moduli after application different strain amplitudes to the sample, below and above the critical strain. We already reported on the flocculation experiment in our previous paper [8] about low density polyethylene nanocomposites filled with layered double hydroxide particles. Here, we make a step further and try to reproduce the measured data theoretically, with the help of a superposition approach in which the contributions from the polymer matrix and the CNT phase are accounted for separately.

## 2. Materials and sample preparation

Polycarbonate, Macrolon® type 2805, ($T_G$ = 145°C, melt flow index (MFI) = 10 g/10 min at 300°C, $\rho$ = 1.2 g/cm$^3$) was produced by Bayer Material Science AG, Leverkusen, Germany. Values for the molecular weights and the polydispersity index of this polymer measured by size exclusion chromatography (polystyrene calibration, chloroform solvent) are as follows:$M_w = 4.40 \cdot 10^4$ g/mol, $M_n = 1.19 \cdot 10^4$ g/mol and polydispersity index (PDI) = $(M_w/M_n) = 3.7$. The polymer is of linear structure and amorphous according to the manufacturer specification.

The multi-walled carbon nanotubes used in this study were Baytubes® from Bayer Material Science AG with max. 5% inorganic impurities. The mean diameter is of about 13–16 nm and the tube length varies between 1 and 10 µm. Thus, the aspect ratio of about 50 can be expected for this polydisperse product.

The MWNT-polycarbonate composites were produced by the melt-mixing process in a twin screw extruder (ZSK 26 MC from Coperion Werner & Pfleiderer, Stuttgart, Germany) in one processing step. Both, the polycarbonate and the MWNTs were fed into the main feeder of the extruder. The total mass flow was in the range of 24 to 27 kg/h depending on the MWNT content which was varied in the range between 3 and 5 wt%. The screw speed was set to 400 rpm. All barrels of the twin screw extruder were set to a heating temperature of 280°C except the barrels of the melting zone which were set to 160 and 205°C. After compounding, the MWNT-polycarbonate composites were cooled down in a water bath and were finally granulated with a pelletizer. The granulates were used to prepare disk-shaped CNT-polycarbonate plates with a diameter of 80 mm and a thickness of 2 mm by injection molding technique at the Thermoplastic Testing Center of Bayer Material Science AG, Leverkusen, Germany. During the injection molding the melt temperature was held at 340°C, the mold temperature was held at 120°C. The flow rate during the filling process was set to approximately 5 $cm^3/s$.

To check the long-term stability of samples at elevated temperatures, thermogravimetric analysis has been carried out. The pure PC samples as well as those filled with 5 wt% CNTs were found to be very stable, exhibiting the weight loss less than 0.5% after 4 hours annealing at 230°C.

## 3. Sample characterization

### 3. 1. TEM analysis

The ultra-thin sections for transmission electron microscopy (TEM) were cut both near the surface of the injection-molded plate and in its interior by microtome at room temperature. The images were taken by Tecnai 20 (FEI Company, Hillsboro, Oregon, USA). The TEM image taken from the interior of the injection-molded plate shows a fine dispersion of MWNTs with the presence of small clusters (Figure 1a). The size of the MWNT clusters is estimated to be less than 200 nm. A similar TEM image has been obtained near the sample surface (not shown here). With the naked eye, one sees no orientation of MWNTs in the injection-molded plates obtained at process conditions mentioned above. Also, it is difficult to find noticeable changes in the size of clusters after one hour annealing of the sample at the elevated temperature of 300°C (Figure 1b), although the long-term annealing leads to considerably higher storage and loss moduli as will be shown further (see Flocculation experiment).

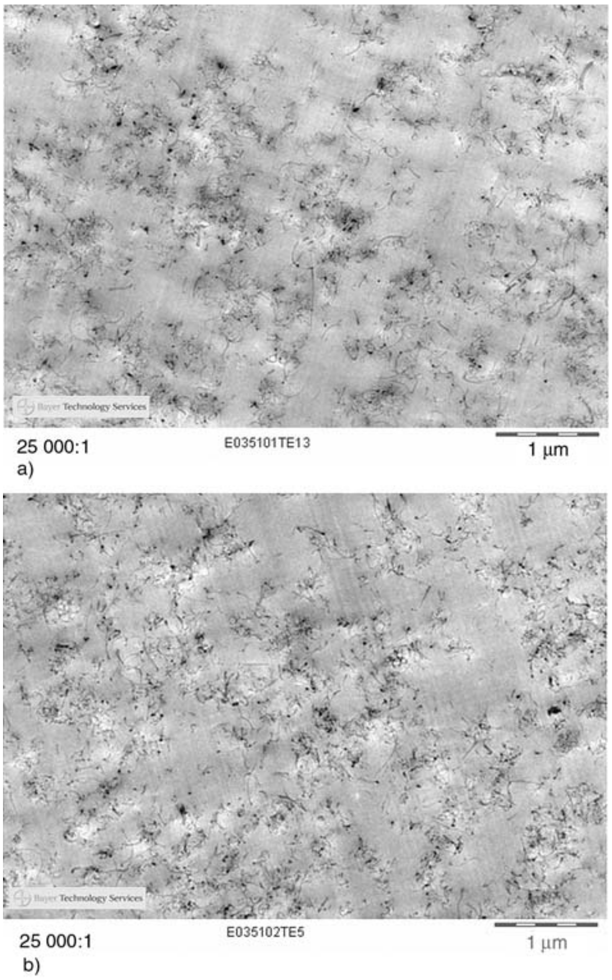

**Figure 1.** a) TEM picture of the sample as-received, b) TEM picture of the sample annealed one hour at 300°C

### 3.2. X-ray scattering analysis

The wide angle X-ray scattering (WAXS) pattern for the pure MWNT powder has been measured over $2\theta = 2 \ldots 60°$ using XRD 3003 Θ/Θ (Seifert-FPM Freiberg/Sa.) with Cu-$K_\alpha$ radiation ($\lambda = 0.154$ nm, monochromatization by primary multilayer system). The WAXS patterns for the pure and filled with 5 wt% MWNT polycarbonate have been measured over $2\theta = 0 \ldots 40.5°$ using X-ray diffractometer P4 (BRUKER *axs* Karlsruhe, Germany) with Cu-$K_\alpha$ radiation ($\lambda = 0.154$ nm, monochromatization by primary graphite crystal). The small angle X-ray scattering (SAXS) patterns for the filled polycarbonate have been measured using a self-constructed 3fold pin-hole system with a RIGAKU rotating anode generating Cu-$K_\alpha$ radiation (monochromatization by primary OSMIC confocal optic). The scattering range over $2\theta = 0.065 \ldots 2.5°$ ($d \approx 135 \ldots 3.5$ nm) has been explored by a marCCD X-ray detector system (Mar USA, Inc.). The primary beam stop of 2 mm diameter has been positioned 1650 mm away from the sample.

The WAXS patterns of pure polycarbonate do not contain any crystalline reflections (Figure 2a, unfilled symbols). Also, no particle scattering, typical for polycrystalline samples, has been found in the SAXS measurements of pure polycarbonate (Figure 2b, unfilled symbols). Thus, both scattering methods confirm that polycarbonate is amorphous. To check the state of PC orientation in the injection-molded plates, the WAXS patterns were measured at three different positions on the same plate at the direction perpendicular to the plate plane and along the injection molding direction (see Fig-

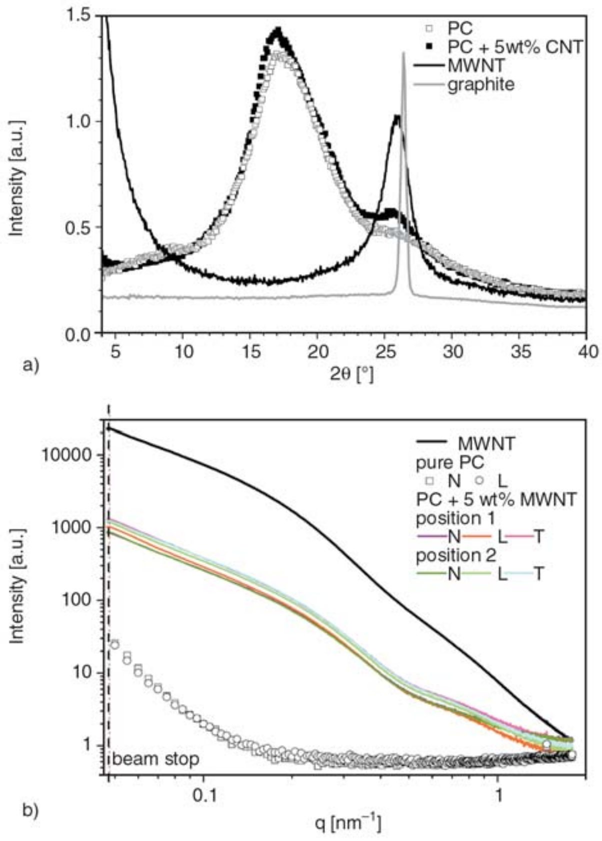

**Figure 2.** a) Typical WAXS curves for pure polycarbonate and polycarbonate filled with 5 wt% MWNTs. For comparison, the WAXS curves for pure MWNT powder and pure graphite are shown. b) SAXS curves for pure polycarbonate, measured at two transmission directions, and polycarbonate filled with 5 wt% MWNTs, measured at the positions 1 and 2 at three transmission directions. For comparison, the SAXS curve for pure MWNT powder is shown.

ure 3). At all positions and directions a wide halo was observed (not shown here). On the WAXS curves (Figure 2a) this halo manifests itself as a wide peak at about 2θ = 17–18°, corresponding to a length of about 0.51 nm in the real space. Such a halo is typical for amorphous scattering from organic polymers. Its form is nearly spherical and hence only negligible orientation of the PC has been detected in the injection-molded samples.

In the WAXS patterns of filled systems one observes an additional peak at about 2θ = 26°. To find a nature of this peak, we performed the WAXS measurement with a pure MWNT powder (Figure 2a, black curve) and compared it with the measurement on pure graphite (Figure 2a, gray curve). The sample of graphite exhibits a sharp peak at 26.6° originating from the scattering on the stacked graphite layers that have a 0.335 nm distance. The MWNT peak is shifted to a slightly smaller angle of 2θ = 26.0° compared to the graphite peak and is noticeably wider than the latter. This means that the peak in MWNT powder originates from the scattering between the MWNT walls that are about 0.342 ± 0.15 nm from one another.

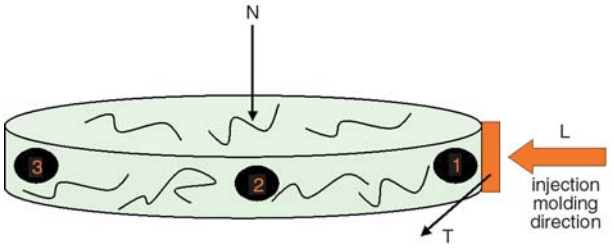

**Figure 3.** Disk-shaped plate, injection-molded from a side. Here (**N**) is the direction normal to the plate surface, (**L**) is the longitudinal direction parallel to that of injection molding, (**T**) is the transverse direction which is perpendicular to the directions (**N**) and (**L**). The samples for the X-ray studies were cut from the plate near its edges at the positions 1, 2 and 3.

To check the state of MWNT orientation in the injection-molded plates, the SAXS patterns were measured at two different positions on the same plate (near the injection point and 90° degrees from it) at three different directions as shown in Figure 3. When the transmission direction is chosen to be perpendicular to the plate surface (**N** direction in Figure 2), one observes a spherical halo in the SAXS patterns for the filled system (Figure 4a). However, in the two other directions, the halo appears to be slightly elliptical that together indicates on slight orientation of MWNTs in the plane of the injection-molded plate. The curves accumulated at two different positions are found to be very similar (Figure 2b) and thus we expect the same degree of MWNT orientation at both positions.

### 3.3. Linear viscoelastic analysis

All oscillatory shear experiments described in this paper were conducted on a controlled strain rate rheometer (ARES rheometer, Rheometrics Scientific) using the plate-plate geometry (diameter of 25 mm, gap between the plates 1–2 mm) in a nitrogen environment. Most studies were performed at 230°C, although some of linear viscoelastic measurements were conducted in the range 200–300°C to allow the time-temperature superposition. All test specimens were cut from the injection-molded

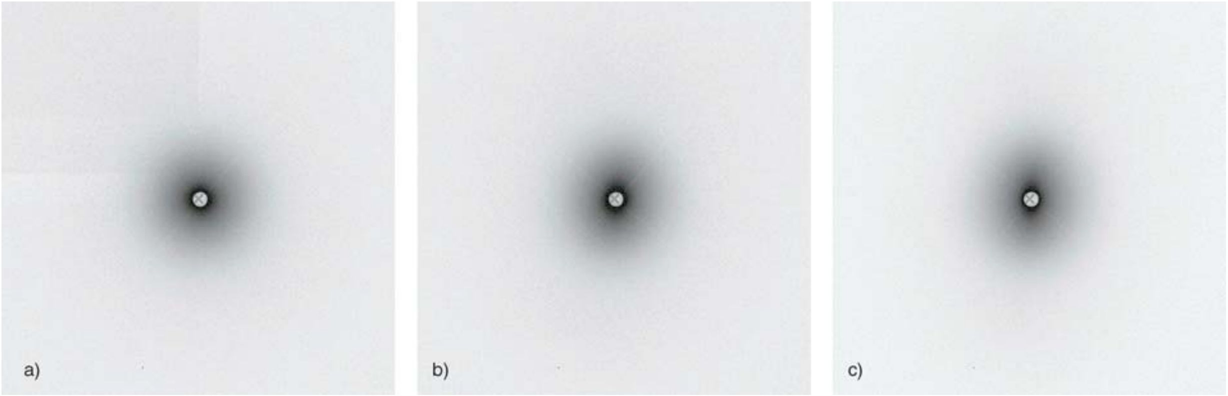

**Figure 4.** SAXS 2D-pattern for the nanocomposite in different transmission directions: normal (**N**) to the surface of the plate (a), longitudinal (**L**) = parallel to the injection molding direction (b), transversal (**T**) = perpendicular to the injection molding direction (c). The sample was cut at position 1 near the injection molding point. All three directions are depicted in Figure 3.

plates. For the linear and nonlinear viscoelastic measurements, except the 'flocculation' experiment, all the samples were equilibrated in the rheometer after loading at the desired temperature for 15 min prior to testing.

To determine the boundary of linear regime, the strain amplitude sweep tests have been carried out at a constant frequency of 10 rad/s (≈1.6 Hz) and temperature 230°C. Figure 5a presents the strain dependencies of the storage modulus, *G'*, for the pure polycarbonate and two composite systems filled with 3 and 5 wt% CNTs. It is apparent that the unfilled polycarbonate melt exhibits linear behavior up to much larger strains compared to the filled system, with the critical strain found within 0.3–0.4 of the strain range. In the case of CNT-polycarbonate composites, the critical strain decreases with increasing CNT content, presumably due to the presence of a filler network superstructure. However, for the nanocomposites with CNT concentration up to 5 wt%, the strain range below 0.01 can be taken as a safe one to study the linear viscoelastic behavior. Interestingly, the nanocomposites show the lower storage modulus than that of the unfilled polycarbonate melt at high-strain region, the tendency clearly increasing with the CNT content. Such behaviour can be presumably explained by interplay of two effects: 1) the filler network structure becomes totally destroyed at such high strains and does not contribute into the modulus, 2) local strains in the matrix should be effectively higher than the applied strains due to the presence of hard particles, i.e. due to the effect of strain amplification which was also observed in the case of low density polyethylene nanocomposites filled with layered double hydroxide particles [8].

The linear viscoelastic response of CNT-polycarbonate composites has been studied using the constant strain amplitude of $\gamma_0 = 0.005$ and frequency sweep from 0.01 to 100 rad/s. In the case of unfilled

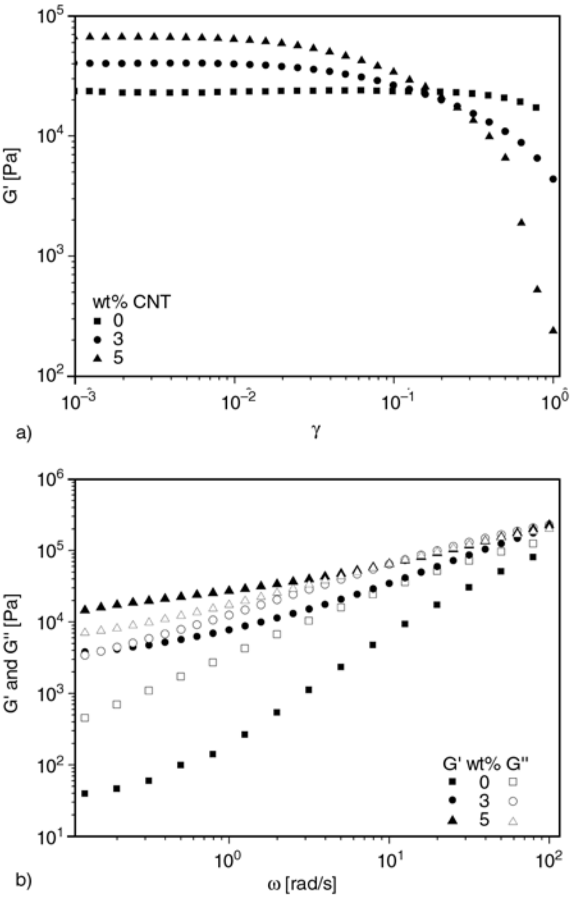

**Figure 5.** a) Strain amplitude sweeps for the storage modulus *G′* of CNT-polycarbonate composites. ω = 10 rad/s. *T* = 230°C. b) Frequency sweeps of the storage *G′* and loss *G″* moduli of CNT-polycarbonate composites. $\gamma_0 = 0.005$. *T* = 230°C.

polycarbonate, the storage modulus $G'$ is found to be considerably lower than the loss modulus $G''$ within the experimental frequency range (Figure 5b). This means that the unfilled polycarbonate melt has dominant viscous character at 230°C. Upon addition of 3 wt% CNTs, both moduli noticeably increase, nevertheless $G'$ stays lower than $G''$ except the regions with the lowest and highest frequencies. Only when 5 wt% CNTs is added to the polymer matrix, the storage modulus becomes approximately three times larger than the loss modulus up to the frequencies of about 2 rad/s. At higher frequencies $G'$ and $G''$ have similar values.

Typically, the polymer melts filled with CNTs exhibit the transition from liquid-like to solid-like behavior at considerably lower values of the CNT loading, somewhere about 1 wt% [9, 10]. Presumably, the behavior observed is caused by very high shear rates during the injection molding resulting in a total destruction of the filler network structure, which is thought by most scientists to be responsible for the liquid-solid transition. This assumption is supported by the TEM images presented in Figure 1a which show the CNT clusters to be very small.

In the case of unfilled polycarbonate, the frequency sweeps from 0.01 to 100 rad/s were measured, additionally, at three different temperatures: 200, 250 and 300°C. To obtain reliable data at higher temperatures, the strain amplitude was increased to 0.05 at 250°C and to 0.1 at 300°C. The frequency sweeps at different temperatures have been used to construct the master curves at the reference temperature of 230°C (Figure 6). For further analysis, the master curves for $G'(\omega)$ and $G''(\omega)$ for unfilled polycarbonate have been converted into the discrete relaxation time spectrum using the commercial software 'IRIS Rheo-Hub 2007' [15]. IRIS expresses the relaxation modulus $G(t)$ as a sum of $N$ Maxwell modes, as shown by Equation (1):

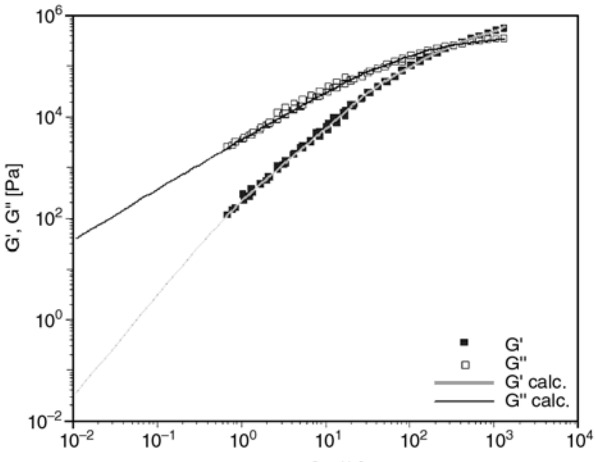

**Figure 6.** Master curves at 230°C obtained from the data measured at four different temperatures: 200, 230, 250 and 300°C. Also shown are the fits of $G'$ and $G''$ obtained from conversion of the PC relaxation spectrum (see Table 1).

**Table 1.** Relaxation spectrum of PC at 230°C

| i | $g_i$ [Pa] | $\lambda$ [s] |
|---|---|---|
| 1 | $6.116\cdot10^{5}$ | $6.377\cdot10^{-4}$ |
| 2 | $2.698\cdot10^{5}$ | $4.125\cdot10^{-3}$ |
| 3 | $6.365\cdot10^{4}$ | $2.313\cdot10^{-2}$ |
| 4 | $2.563\cdot10^{3}$ | $1.703\cdot10^{-1}$ |
| 5 | $2.227\cdot10^{2}$ | $9.205\cdot10^{-1}$ |

$$G(t) = \sum_{i=1}^{N} g_i \exp\left(-\frac{t}{\lambda_i}\right) \tag{1}$$

The weight coefficients, $g_i$, and the relaxation times, $\lambda_i$, in Equation (1) are determined by the Baumgärtel's method [16]. This method is based on two major premises. These are (1) the simultaneous fitting of $G'$ and $G''$ in order to robust the numerical algorithm, and (2) the prevention of 'overfitting' by choosing the admissible number of modes per decade depending on the noise in the data.

Weight coefficients $g_i$ and relaxation times $\lambda_i$ of the discrete relaxation spectrum for the PC 2805 at 230°C are summarized in Table 1. The longest relaxation time is about 1 s and the zero-shear viscosity is $\eta_0 = 3620$ Pa·s. It can be seen from Figure 6 that a back conversion from the time domain to the frequency domain provides a perfect fit of the storage and loss moduli.

## 4. Model description

If the polymer melt is filled with attractively interacting nanoparticles, its rheological behaviour can be relatively well described in the framework of superposition approach originally proposed by Leonov [17]. In this approach the total stress tensor, $\boldsymbol{\sigma}$, is represented by a sum of two stresses, as shown by Equation (2):

$$\boldsymbol{\sigma} = X\boldsymbol{\sigma}_p + \boldsymbol{\sigma}_f^{Net} \tag{2}$$

where $\boldsymbol{\sigma}_p$ is the viscoelastic stress arising in the matrix due to orientation of polymer strands. This component is described in our study by the Doi-Edwards model proposed for the linear polymer chains [18]. Hydrodynamic reinforcement of the polymer matrix is taken into account by multiplying $\boldsymbol{\sigma}_p$ by the hydrodynamic amplification factor, $X$. In the case of highly elongated CNT particles, which we consider here in the first approximation as prolate spheroids, $X$ is given by Equation (3) [19]:

$$X = 1 + 2\phi\left(1 + \frac{A}{15}\right) \tag{3}$$

Equation (3) is valid in the case of isotropic orientation of elongated particles, $\phi$ is the volume fraction of the filler particles and $A$ is the stress-shape coefficient (Equation (4)):

$$A = \frac{r^2}{2\ln r}, \quad r >> 1 \tag{4}$$

which depends only on the particle aspect ratio $r = L/d$ ($L$ is the particle length and $d$ is its diameter). The second component on the right side of Equation (2), $\boldsymbol{\sigma}_f^{Net}$, arises due to attractive interactions between the particles. It is described by a modified viscoelastic Maxwell model containing a structural parameter that reflects the state of the particle network at particular shear conditions [17]. Thus, we consider only hydrodynamic interactions between CNTs and the polymer matrix and neglect possible attractive interactions between them. Although the latter can be also taken in to account (for example using the formalism proposed by [20]), it will complicate the description considerably.

## 4.1. Doi-Edwards model for large-strain viscoelasticity

Doi and Edwards developed a constitutive equation for entangled polymer melts that combines the linear viscoelastic response for a reptating chain with a nonlinear response to large deformations [18]. The stress tensor of the Doi-Edwards (DE) theory with the assumption of independent alignment (IA) of the polymer strands is described by Equation (5):

$$\boldsymbol{\sigma}_p(t) = \int_{-\infty}^{t} \frac{\partial G(t-t')}{\partial t'} \mathbf{S}^{IA}(t,t')\mathrm{d}t, \quad \mathbf{S}^{IA} = 5\mathbf{S}_2 \tag{5}$$

where $G(s)$ is the stress relaxation modulus at time $s = t - t'$ and $\mathbf{S}^{IA}$ is the nonlinear viscoelastic strain tensor. The factor of 5 is introduced into the definition so that $\mathbf{S}^{IA}$ equals the linear viscoelastic strain tensor $\gamma(t,t')$, when the strain is small. $\mathbf{S}_2$ has a meaning of the second-order orientation tensor of polymer strands (Equation (6)):

$$\mathbf{S}_2 = \int \frac{(\mathbf{E}\cdot\mathbf{u})(\mathbf{E}\cdot\mathbf{u})}{|\mathbf{E}\cdot\mathbf{u}|^2} \mathrm{d}\mathbf{u} \tag{6}$$

where $\mathbf{u}$ is the unit vector parallel to the end-to-end vector of a strand and $\mathbf{E}(t,t')$ is the displacement-gradient tensor [21]. It is important to note that the deformed vector $\mathbf{E}\cdot\mathbf{u}$ in Equation (6) is normalized on its magnitude. This means that in the original DE model the polymer strand is assumed to be oriented by the flow but not stretched.

In this study Equations (5) and (6) were solved using the commercial software IRIS Rheo-Hub 2007 [15]. First, we followed the approach proposed for polydisperse linear polymer melts [22]. In this approach, an actually measured relaxation spectrum for a particular polymer is used instead of the original DE expression for a reptational relaxation spectrum. However, if one takes the relaxation spectrum extracted from the master curves for PC 2805, i.e. $\{g_i, \lambda_i\}$ given in Table 1, it is impossible to predict the stress growth curves measured in a relatively narrow interval of shear rates, $0.05\ \mathrm{s}^{-1} \le \dot{\gamma}_0 \le 1\ \mathrm{s}^{-1}$ (see Figure 7a). First, the theoretically predicted curves lay considerably lower than the experimentally measured ones. So, the value of stationary viscosity at $0.05\ \mathrm{s}^{-1}$, at the lowest shear rate used, is found to be about 8000 Pa·s. This means that the value of zero-shear viscosity extracted from the stress growth experiment is approximately two times higher than that extracted from the linear data. Why PC 2805, the polycarbonate batch used in this study, exhibits such a discrepancy is presently not clear. Second, none of the predicted curves exhibits a shear overshoot observed clearly at least for two middle shear rates. Thus, it seems that the approach based on the original DE equation (Equation (5)) does not work well in the case of PC 2805, although the polydispersity effects have been taken into account via an actually measured relaxation spectrum. Recently, it has been shown that a very good description of the experimental data of polydisperse polyethylene melts can be obtained in the frame of molecular stress function (MSF) theory which accounts for the process of convective constraint release [23].

In the following, we will restrict ourselves to the simplified description of matrix behaviour based on the original DE model with the single relaxation mode $g_1 = 8\cdot10^4$ Pa and $\lambda_1 = 0.1$ s$^{-1}$. This relaxation mode with the zero-shear viscosity of $\eta_0 = 8000$ Pa·s describes reasonably well the overall course of stress growth curves, although it is not able to predict the shear overshoots observed at middle shear rates (see Figure 7b). Nevertheless, we will use this single relaxation mode for the description of transient viscosity, $\eta_p$, of the polycarbonate matrix in the stress growth experiment with filled systems. The transient viscosity is defined by Equation (7) as the ratio of shear component, $\sigma_p$, of the stress tensor $\boldsymbol{\sigma}_p$ (Equation (5)) to the constant shear rate, i.e. (Equation (7)):

$$\eta_p(t) = \frac{\sigma_p(t)}{\dot{\gamma}_0} \tag{7}$$

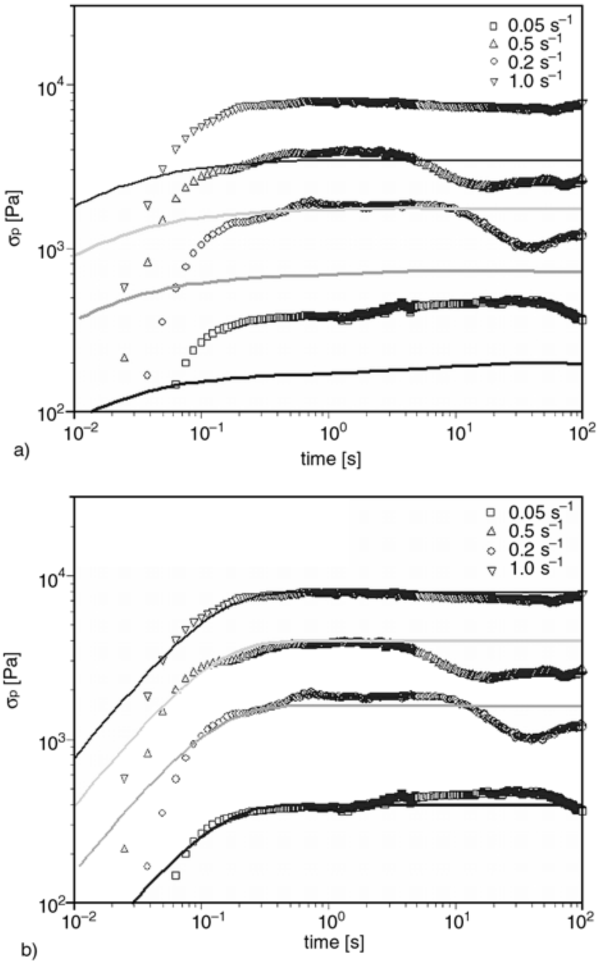

**Figure 7.** a) Stress growth curves for unfilled PC at four different shear rates: open symbols – experiment, lines – fit using Equation (5) and the relaxation spectrum given by Table 1. b) Stress growth curves for unfilled PC at four different shear rates: open symbols – experiment, lines – fit using Equation (5) and the single relaxation mode (see text).

## 4.2. Modified viscoelastic Maxwell model

Let us consider the CNT network as a viscoelastic structure. We assume that the stress experienced by the filler structure can be described by a modified viscoelastic Maxwell model given by Equation (8):

$$(\boldsymbol{\sigma}_f^{Net})_{(1)} + \frac{G_f}{\eta(\xi_b)}\boldsymbol{\sigma}_f^{Net} = G_f\dot{\boldsymbol{\gamma}} \tag{8}$$

where $\dot{\boldsymbol{\gamma}}$ is the rate-of-strain tensor and $(\boldsymbol{\sigma}_f^{Net})_{(1)}$ denotes the upper-convected time derivative of a tensor $\boldsymbol{\sigma}_f^{Net}$ [21]. Here $G_f$ is the effective elastic modulus of the filler network. Usually, it is considerably lower than the Young modulus of one filler particle. For example, the Young modulus of about 0.2–1 TPa has been reported for single carbon nanotubes [24], while in the present study $G_f$ is found to be of about 50 kPa. The term $\eta$ is the effective viscosity of the filler network which depends on the structural parameter $\xi_b$. Thus, Equation (8) implies a process-dependent relaxation time which is an intrinsic feature of the thixotropic systems [25, 26]. The modified Maxwell model provides a phenomenological description of the structural rearrangements in the filler network structure. It is however physically motivated. To ascribe a simple physical meaning to $\xi_b$, let us assume that the filler structure is stabilized by a number of physical bonds that can be broken by the shearing in a nonlinear regime and can be again re-built during the quiescent time. These physical bonds represent attractive interactions between the multi-walled carbon tubes being part of the percolating filler network which bears a stress. This simple physical interpretation for example implies that the irreversible attractive interactions in primary agglomerates should not contribute into the structural parameter. Further, it is assumed that the total number of bonds – broken and unbroken – is not changing. Hence, a usual kinetic equation (Equation (9)) can be written for the change of the fraction of broken bonds $\xi_b$:

$$\frac{\mathrm{d}}{\mathrm{d}t}\xi_b = a|\dot{\gamma}_0|(1-\xi_b)^n - \lambda_0^{-1}\xi_b \tag{9}$$

where the first term on the right side describes the bond rupture in a flow with the shear rate $\dot{\gamma}_0$, while the second term allows for the bond re-building driven by strong attractive interactions between the particles. Here $a$ is the rupture strength and $\lambda_0$ is the relaxation time in the quiescent state. The exponent $n$ describes the order of the kinetic process. We tried both the first-order kinetics with $n = 1$ and the second-order kinetics with $n = 2$ and obtained very similar results. Therefore, for the sake of simplicity, we consider further only the case with $n = 1$.

On the start-up of shear flow, the fraction of broken bonds increases according to Equation (10):

$$\xi_b(t) = a\dot{\gamma}_0\lambda_\gamma\left(1 - e^{\frac{-t}{\lambda_\gamma}}\right) \quad \text{with} \quad \lambda_\gamma = \frac{\lambda_0}{1 + a\dot{\gamma}_0\lambda_0} \tag{10}$$

where $\lambda_\gamma$ is the relaxation time in the presence of flow. During the relaxation process, when the flow is switched off, the time dependence is given by Equation (11):

$$\xi_b(t) = a\dot{\gamma}_0\lambda_\gamma e^{\frac{-t}{\lambda_0}} \tag{11}$$

In the nonlinear regime, i.e. at high shear rates, $\lambda_\gamma$ may become significantly lower than $\lambda_0$ which results in two totally different time scales in the system [27].

The time-dependent effective viscosity can be now defined by Equation (12):

$$\eta(\xi_b) = \frac{\eta_f}{m(\xi_b(t))} \tag{12}$$

where $\eta_f$ is the viscosity parameter and $m(\xi_b)$ is the mobility function. There are different ways to define the mobility function in literature [26, 28]. To choose an appropriate one, it is important to satisfy a number of criteria:

1) Highly filled polymer nanocomposites exhibit the transition to solid-like behavior in the limit of vanishing shear rates. A typical manifestation of such transition is the appearance of low-frequency plateau for the storage modulus $G'$ on Figure 5b. Hence, $m(\xi_b) \to 0$ if $\xi_b \to 0$.
2) At high shear rates, a typical viscoelastic liquid behavior is observed. Hence, $\eta(\xi_b)$ should be a decreasing function of the structural parameter, i.e. $\mathrm{d}m(\xi_b)/\mathrm{d}\xi_b > 0$.

The following form, given by Equation (13), proposed by [29]:

$$m(\xi_b) = \frac{(1-\xi_b)^{-d} - 1}{d}, \quad d > 0 \tag{13}$$

meets the above criteria. Equation (13) predicts a perfect elastic response of the undamaged filler structure, i.e. the loss modulus of filler structure $G_f''$ vanishes at $\omega \to 0$. This is hardly the case as the loss modulus of highly filled polymer nanocomposites considerably exceeds that of a polymer matrix at small and intermediate frequencies and even exhibits a kind of low-frequency plateau as can be seen from Figure 5b. To describe a non-vanishing $G_f''$ at small frequencies, one should add to the left side of Equation (13) the residual parameter $\alpha$ [17], see Equation (14):

$$m(\xi_b) = \alpha + \frac{(1-\xi_b)^{-d} - 1}{d}, \quad \alpha < 1 \tag{14}$$

This expression for mobility function will be used in the modeling of stress growth curves as well as of time-dependent viscoelastic moduli in the flocculation experiment.

To calculate the latter let us consider the oscillatory shearing described by Equation (15):

$$\gamma = \gamma_0 \sin \omega t \tag{15}$$

The changes in the structural parameter $\xi_b(t)$ can be calculated using Equations (10) and (11) in which instead of $\dot{\gamma}_0$ one should put the effective shear rate (Equation (16)):

$$\dot{\gamma}_{eff} = \frac{2}{\pi}\gamma_0\omega \tag{16}$$

defined as an average over half period of the instantaneous shear rate $\dot{\gamma} = \gamma_0\omega\cos\omega t$. Thus, we neglect small oscillatory fluctuations of the structural constant around its stationary value, as they do not influence the values of $G_f'$ and $G_f''$ that are the averages over at least one oscillation period $T = 2\pi/\omega$.

Let us now rewrite Equation (8) for the shear component of $\boldsymbol{\sigma}_f^{Net}$ in the case of oscillatory shearing, obtaining Equation (17):

$$\frac{\mathrm{d}}{\mathrm{d}t}\sigma_f^{Net} + \frac{m(\xi_b)}{\tau_f}\sigma_f^{Net} = G_f\gamma_0\omega\cos\omega t \tag{17}$$

Here we made use of Equation (13) and introduced $\tau_f = \eta_f/G_f$. The time-dependent solution of Equation (17) can be found in the form of Equation (18):

$$\sigma_f^{Net} = \gamma_0\{G'_f(t)\sin\omega t + G''_f t)\sin\omega t\} \tag{18}$$

using the Matlab software. The stationary values of $G'_f$ and $G''_f$, which are measured in the strain or frequency sweep experiments, can be defined analytically using the stationary value of the structural parameter, given by Equation (19):

$$\xi_b(\gamma_0,\omega) = \frac{a\dot{\gamma}_{eff}}{a\dot{\gamma}_{eff} + \lambda_0^{-1}} \tag{19}$$

This results in Equations (20):

$$G_f^{'} = G_f \frac{\Omega^2}{\Omega_0^2 + \Omega^2} \quad \text{and} \quad G_f^{"} = G_f \frac{\Omega_0\Omega}{\Omega_0^2 + \Omega^2} \tag{20}$$

where $\Omega = \omega\tau_f$ is the dimensionless frequency and is given by Equation (21):

$$\Omega_0 = \alpha + \frac{(1 + a\lambda_0\dot{\gamma}_{eff})^d - 1}{d} \tag{21}$$

One can see that in the limit of very small strain amplitudes, i.e. when $\dot{\gamma}_{eff} \to 0$, $\Omega_0 \to \alpha$, and thus both the storage and the loss modulus have a non-zero value.

## 5. Results and discussion

### 5.1. Stress growth experiment

Figure 8 shows comparison between the shear growth curves measured for unfilled and filled with 5 wt% CNTs polycarbonate melt at 230°C. To avoid long memory effects typical for highly filled polymer systems [8], a new sample has been taken for every measurement and annealed during 15 minutes at 230°C before application of the shear flow. As expected, at all shear rates the transient stress for the filled system considerably exceeds that for the polymer matrix. This reinforcement effect is especially pronounced at the smallest shear rate used, i.e. $\dot{\gamma}_0 = 0.05\ \text{s}^{-1}$. Further, we found out that the viscosity of filled PC increases monotonically with time for all shear rates except that of $0.5\ \text{s}^{-1}$ (the weak maximum observed at this shear rate is most likely an experimental artefact), reaching a stationary value after the strain of about 1 (Figure 8). This is a potentially significant finding that deserves a careful consideration. Usually, in highly filled systems one observes a pronounced shear overshoot that can be ascribed to the orientation of anisometric filler particles along the flow direction [7], or alternatively to the breakage of filler network structure under shear [8].

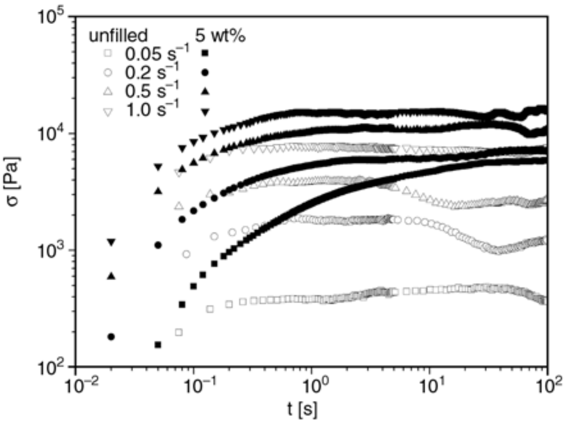

**Figure 8.** Stress growth curves at four different shear rates: open symbols – unfilled PC, filled symbols – PC filled with 5 wt% CNTs

Let us first consider the orientation scenario. The morphological characterization with the help of X-ray scattering and TEM studies provides the following information about the orientation state of CNTs after the injection molding. TEM images show no visible orientation of CNTs in the injection-molded plates (Figure 1a), even near the plate surfaces where the shear rates can be as high as $10^3$–$10^4\ \text{s}^{-1}$. According to the X-ray measurements the CNTs are only slightly oriented in the plane of the injection-molded plate, i.e. after application of extremely high shear rates. Therefore, we assume that there is no further orientation of CNTs in the ARES rheometer, i.e. under relatively small shear rates up to $1\ \text{s}^{-1}$. Hence, we can use a constant value of the hydrodynamic amplification factor $X$ (the ratio of stationary viscosity of the filled system to that of the pure polymer matrix) given in the case of isotropic orientation of elongated particles by Equation (3).

The best fit of the upper curve ($\dot{\gamma}_0 = 1.0\ \text{s}^{-1}$) in Figure 9a is obtained if one takes the particle aspect ratio of about 35. This corresponds to a value of the reinforcement factor $X \approx 1.9$ (Equation (3)). Thus, we have shown that the hydrodynamic reinforcement is relatively small for these polycarbonate composites filled with 5 wt% of CNTs. Although, one obtains a very good agreement between the predicted and measured data at $\dot{\gamma}_0 = 1.0\ \text{s}^{-1}$, the discrepancy between the theory and the experiment increases with decrease of the shear rate. This can

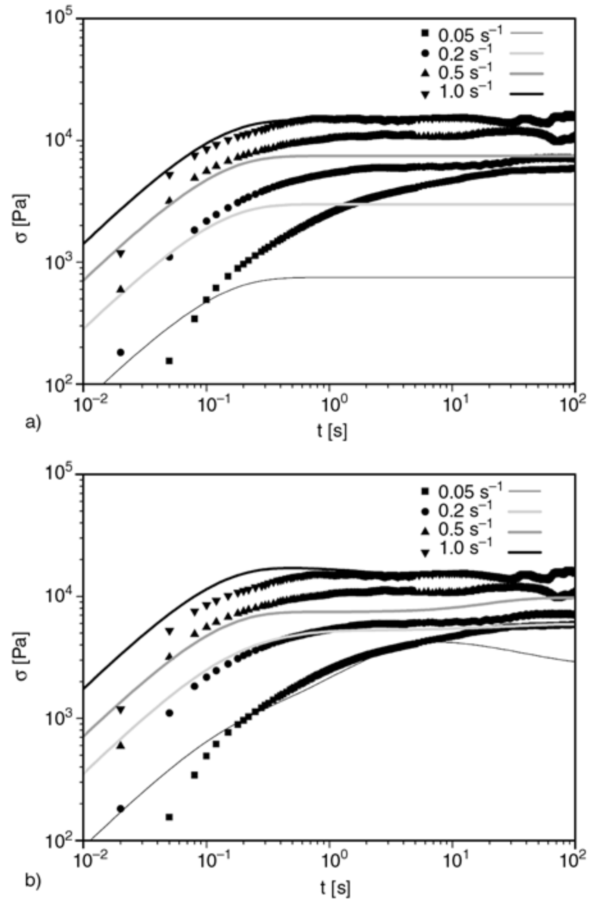

**Figure 9.** Stress growth curves for the PC filled with 5 wt% CNTs at four different shear rates: filled symbols – experiment, lines – fit using Equation (8). $r = 35$. CNT agglomeration is neglected (a), taken into account (b).

be explained by the presence of CNT agglomerates that either survived the process of injection molding or were formed in the injection-molded samples during the thermal treatment in the ARES cell (15 minutes at 230°C). At the smallest shear rate used, $\dot{\gamma}_0 = 0.05\ \text{s}^{-1}$, the agglomerates cannot be effectively destroyed and thus they contribute into the total stress via the component $\sigma_f^{Net}$ described by Equation (8). With the increase of shear rate, $\sigma_f^{Net}$ decreases and becomes negligible at $\dot{\gamma}_0 = 1.0\ \text{s}^{-1}$.

The best fit of shear growth curves in the presence of CNT agglomeration is shown in Figure 9b. Here we used a set of parameters extracted from the fitting of the 'flocculation' experiment that will be discussed in the following section. The relevant parameter for our discussion is the initial value of structural parameter $\xi_b$ which is taken here to be equal to 0.4. This means that 40% of physical bonds between CNTs are broken in the composite samples which were annealed during 15 minutes at 230°C before shearing in the ARES cell. To achieve a fully relaxed initial state with $\xi_b$=0, one needs to anneal the sample at least two hours at 230°C prior application of the shear flow (see the next section). Figure 9b indicates a satisfactory agreement between the predicted and measured data, with the only exception that the predicted transient shear stress slightly decreases at longer times for the curve with $\dot{\gamma}_0 = 0.05\ \text{s}^{-1}$. Obviously, this slight decrease is a manifestation of breakage of CNT agglomerates.

## 5.2. Flocculation experiment

The dynamic oscillatory shearing at constant frequency shows that at low strain amplitudes both storage and loss moduli of the CNT/polycarbonate composites remain constant and independent of the applied strain (Figure 10), whereas above a critical strain $\gamma_{cr} \sim 0.01$ both moduli decrease with increasing strain. At two applied frequencies, $G'$ decreases faster than $G''$. So, at $\omega = 10$ rad/s, below $\gamma_{cr}$ the loss modulus is found to be only slightly lower than the storage modulus, whereas above $\gamma_{cr}$ it becomes noticeably higher than the storage modulus. At $\omega = 1$ rad/s, this transition to the more viscous behavior takes place at a higher value of strain amplitude $\gamma_0 \sim 0.1$ as the initial value of $G'$ at this frequency is 1.5 times higher than that of $G''$. In the following $\omega = 1$ rad/s has been chosen to study the structural changes in the filled polycarbonate melt by subjecting it to different strain amplitudes, below and above the critical strain. An investigation which will be addressed shortly as the 'flocculation' experiment.

At the first stage of the flocculation experiment an injection-molded sample is subjected to the oscillatory shearing with a strain amplitude $\gamma_0 = 0.005$. It is chosen to be so low that the sample at this stage can be considered to be in the quasi-quiescent state. The slight oscillatory perturbation is only necessary to detect the changes in $G'$ and $G''$ with time. Thus, at the first stage one is able to follow in-situ the re-agglomeration of the CNT clusters destroyed previously in the process of injection molding. When the stationary state is nearly attained, the sample is subjected to shearing with high strain amplitude at which the CNT clusters are effectively destroyed. Here, we chose a two-step shear-induced breakage of the filler structure, first at $\gamma_1 = 0.05$ and then at

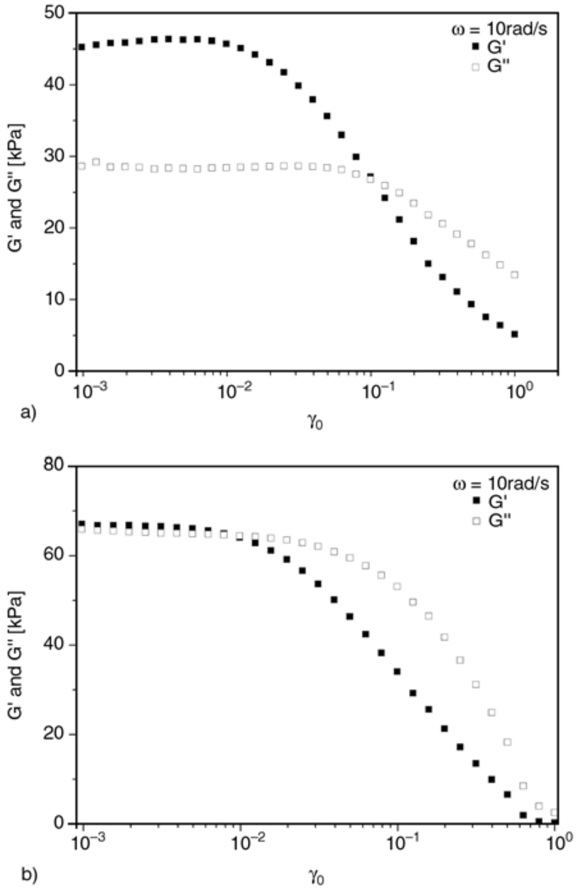

**Figure 10.** Strain amplitude sweeps of the storage $G'$ and loss $G''$ moduli of PC filled with 5 wt% CNTs at two different frequencies: $\omega = 1$ rad/s (a) and $\omega = 10$ rad/s (b). $T = 230°C$.

$\gamma_2 = 0.25$. For control, after attaining the stationary state at $\gamma_2 = 0.25$, the sample is again allowed to rest at the strain amplitude $\gamma_0 = 0.005$. It is meaningfully to characterize each shearing step by its effective shear rate $\dot{\gamma}_{eff}$. In the flocculation experiment with $\omega = 1$ rad/s, $\gamma_0 = 0.005$ corresponds to $\dot{\gamma}_{eff} \approx 0.003\ s^{-1}$, $\gamma_1 = 0.05$ to $\dot{\gamma}_{eff} \approx 0.03\ s^{-1}$ and $\gamma_2 = 0.25$ to $\dot{\gamma}_{eff} \approx 0.16\ s^{-1}$.

Let us first consider the sample behavior in the quasi-quiescent state ($\gamma_0 = 0.005$). Typical curves are presented on Figure 11. It can be seen that both moduli considerably increase with time: $G'$ approximately three times and $G''$ approximately 25% compared to the initial values (Figure 11a). Further, one observes at least two recovery processes. The first process is relatively fast with the relaxation time of about 50 s and can be very likely associated with the agglomeration of CNTs into a sphere-like viscoelastic clusters [30]. Simple Brownian motion cannot be responsible for this agglomeration process as diffusion of non-interacting filler particles is estimated to be too slow to be taken into account in the explanation of this effect. Rather, the strong attractive interactions between the dispersed carbon nanotubes and thermodynamic incompatibility between the particle and the polymer phases facilitate such fast agglomeration of the CNTs within a highly viscous medium [8]. The second recovery process is extremely slow without a sign of saturation even after two hours. It can be presumably associated with the gradual rearrangement of the CNT agglomerates in a network-like structure. Slow reorientation of CNTs back into the isotropic state cannot be responsible for this second recovery process in which the storage modulus increases on about 10 kPa. Such dramatic increase is far above the changes that can be caused in the storage modulus by the change in hydrodynamic reinforcement upon the reorientation of CNTs if one considers reasonable values of the aspect ratio, $r \leq 100$. After application of the oscillatory shearing with $\gamma_1 = 0.05$, the storage modulus drops immediately staying however higher than its initial value measured in the beginning of flocculation experiment (Figure 11a). The loss modulus stays unchanged which is in agreement with the data of strain amplitude sweep (Figure 10a). The fast drop in $G'$ is caused solely by the rapid destruction of the CNT clusters as we can certainly exclude the orientation of tubes at this step with $\dot{\gamma}_{eff} \approx 0.03\ s^{-1}$. As it was shown previously, there is no reorientation of CNTs at shear rates below $1.0\ s^{-1}$.

The next shearing step with $\gamma_2 = 0.25$ is performed after the crossing point in Figure 10a and, therefore, the drop in both moduli leads now to a higher value of $G''$ compared to $G'$ (Figure 11a). Interestingly, both moduli drop below their initial values measured in the beginning of flocculation experiment. The latter can be somewhat higher than the real initial values in the as-received probes, as the ARES software needs 8 s at $\omega = 1$ rad/s to measure the first point. Nevertheless, there is no doubt that the oscillatory shearing with $\gamma_2 = 0.25$ ($\dot{\gamma}_{eff} \approx 0.16\ s^{-1}$) causes a similar qualitative change in the moduli as the injection molding. This is a very interesting finding as we can again prove that the orientation effects play a negligible role at $\dot{\gamma}_{eff} \approx 0.16\ s^{-1}$ and thus the changes in moduli should be mainly assigned to the process of cluster destruction. Figure 11a shows that this destruction is very rapid and takes place at very small shearing rates.

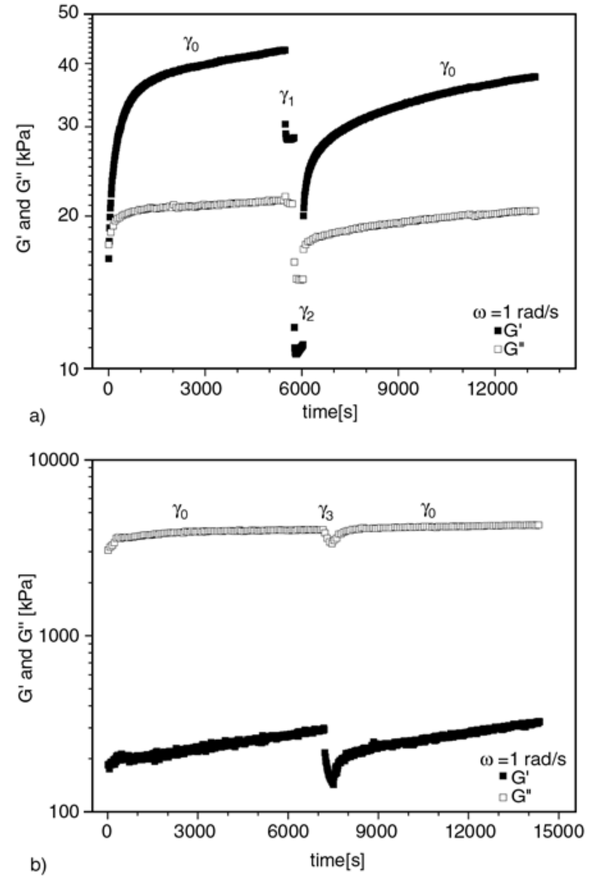

**Figure 11.** Flocculation experiment at different strain amplitudes: $\gamma_0 = 0.005$, $\gamma_1 = 0.05$, $\gamma_2 = 0.25$ and $\gamma_3 = 1.0$, $\omega = 1$ rad/s, $T = 230°C$. (a) PC filled with 5 wt% CNTs, (b) pure polycarbonate.

Obviously, this indicates that the CNT clusters are very fragile and thus can be easily damaged at shear rates $\dot{\gamma}_0 \geq 1\ s^{-1}$. Taking into account extremely high shear rates ($10^3$–$10^4\ s^{-1}$) at the injection molding process, we assume a total breakage of clusters in the as-received samples.

The control step made at the quasi-quiescent conditions ($\gamma_0 = 0.005$) shows a very similar behavior to the behavior at the first stage of the flocculation experiment. First of all, this means that all of the processes taking place in our system are fully reversible. Secondly, we can use this control step, together with two breakage steps preceding it, to test our superposition model as in all three cases we have a well-defined starting point. Before doing that, we have performed an additional control experiment with the unfilled polycarbonate (Figure 11b). At the quasi-quiescent conditions, a slight increase of both moduli has been found for the injection-molded sample. Application of the oscillatory shearing with $\gamma_3 = 1$ ($\dot{\gamma}_{eff} \approx 0.67\ s^{-1}$) leads to a noticeable decrease of both moduli approximately to their initial values in the beginning of control experiment. During the second rest period the sample exhibits the same behavior as during the first rest period. In the following modeling of flocculation experiment, the gradual changes in the storage and loss moduli of the polycarbonate matrix will be neglected as these changes do not exceed 0.1 kPa for $G'_p$ and 1 kPa for $G''_p$ as can be seen in Figure 11b. This is considerably lower than the corresponding changes, about 30 kPa for $G'$ and 10 kPa for $G''$ (Figure 11a), caused by the structural rearrangement of the CNT-network. Therefore, the storage and loss moduli will be described in the first approximation by their average values: $G'_p = 200$ Pa and $G''_p = 3500$ Pa. The gradual changes in the total moduli are defined in the frame of superposition approach by the Equations (22) and (23):

$$G'(t) = XG'_p + G'_f(t) \tag{22}$$

$$G''(t) = XG''_p + G''_f(t) \tag{23}$$

Here, the hydrodynamic reinforcement of the polymer matrix is taken into account via the factor $X \approx 2$ that was extracted earlier from the fitting of stress growth curves.

In the modeling of flocculation experiment, the extremely slow relaxation process seen in Figure 11a will be neglected. Thus, we will concentrate on the phenomenological description of the agglomeration – de-agglomeration process responsible for the fast changes in the viscoelastic moduli. This process will be described by the modified viscoelastic Maxwell model which is characterized by a set of six parameters. Note, that it is necessary to introduce at least two more parameters, i.e. an additional kinetic equation (Equation (9)), if one would like to describe also the second (slow) relaxation process.

Such a large number of parameters is quite common in the modeling of thixotropic behavior [7, 25, 26]. The set of six parameters is the smallest one that is required to describe, even in a simplified manner, the physical phenomena that govern the structural kinetics and the rheology of CNT-polymer composites under study. Two of the model parameters, the relaxation time in the quiescent state $\lambda_0$ and the rupture strength $a$ (see Equation (9)), determine the evolution of the structural parameter $\xi_b$ and thus the rates of structural reorganization under shear and in its absence. The relaxation time $\lambda_0$ can be directly estimated from exponential fitting of the recovery process (not shown here). One can also estimate the relaxation time in the presence of flow $\lambda_\gamma$ from the two breakage steps and thus, using the formula (16), the value of parameter $a \sim 0.1$. Another two parameters, the residual parameter $\alpha$ and the exponent $d > 1$, are necessary to calculate the time-dependent effective viscosity via the mobility function (see Equation (14)). As was discussed above, the values of $\alpha$ and $d$ strongly influence the form of strain and frequency sweeps. Further, we will keep the value of parameter $d = 2$ which means that shearing at high shear rates is able to destroy the filler structure completely. The last two parameters, the effective modulus of the filler structure $G_f$ and the viscosity parameter $\eta_f$, or their ratio $\tau_f = \eta_f/G_f$ that is more convenient in use, define the magnitudes of $G_f'$ and $G_f''$. The value of $G_f$ can be identified with the storage modulus of filler structure in the absence of shear and thus it should be about the stationary value of modulus, ca. 40 kPa, at $\gamma_0 = 0.005$. Thus, we have actually only two parameters, $\tau_f$ and $\alpha$, that should be defined by fitting the experimental data.

Figure 12 presents the best fit of two breakage steps and the second quasi-rest period in the flocculation experiment using the set of parameters presented in Table 2. Relaxation times in the presence of oscillatory shear flow are $\lambda_\gamma = 43$ s for $\gamma_1 = 0.05$ and $\lambda_\gamma = 28$ s for $\gamma_2 = 0.25$. It can be seen that the evolution of storage modulus is reproduced reasonably well, but still a big discrepancy between the experimental data and theoretical prediction for the loss modulus exists. Similar problems were reported by [26], who could not provide a reasonable fit of the strain dependence of the loss modulus, although a number of elaborated viscoelastic models have been tried. Presently, we cannot say what process should be taken into account or how the model should be improved, to reach a better agreement with the experimental data for the loss modulus. Both moduli exhibit a noticeable jump in the moment of strain amplitude change, which is not predicted by the time-dependent solution of Equation (17). The same jump is exhibited by the PE-LDH nanocomposites upon the sudden change of strain amplitude, and thus it is not specific for the CNT-filled systems [8].

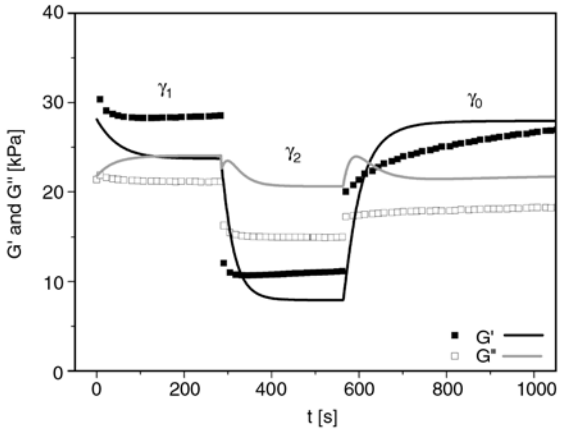

**Figure 12.** Time evolution of the storage $G'$ and loss $G''$ moduli at different strain amplitudes: $\gamma_0 = 0.005$, $\gamma_1 = 0.05$, and $\gamma_2 = 0.25$, $\omega = 1$ rad/s, $T = 230$°C. Filled symbols – experiment, lines – fit using Equations (22) and (23) and the parameter set given in the Table 2.

**Table 2.** Model parameters for PC filled with 5 wt% CNTs

| **Parameter** | **Value** |
|---|---|
| **Matrix** | |
| Viscosity, $\eta_0$ | 8000 Pa·s |
| Reinforcement factor, $X$ | 1.9 |
| **Filler structure** | |
| Relaxation time in the quiescent state, $\lambda_0$ | 50 s |
| Rupture strength, $a$ | 0.1 |
| Effective elastic modulus, $G_f$ | 35 kPa |
| Ratio $\tau_f = \eta_f/G_f$ | 0.8 |
| Residual parameter, $\alpha$ | 0.4 |
| Exponent, $d$ | 2 |

## 6. Conclusions

In this study we performed an extensive morphological and rheological characterization of the MWNT-polycarbonate composites produced by the injection molding technique. The main focus was to carry out such nonlinear viscoelastic experiments which allow to follow the structural rearrangements in the melt state.

In the first experiment, the polycarbonate composites with 5 wt% CNTs were sheared at a constant rate in the ARES rheometer to obtain a set of stress growth curves at different shear rates. The data obtained were then modelled using a superposition approach in which contributions from the polymer matrix, embedded nanotubes and their clusters have been accounted separately. The main effect found is the breakage of CNT clusters upon nonlinear shearing in the ARES rheometer. These clusters were presumably grown during 15 minutes tempering of as-received samples, as in the latter we expect a nearly total breakage of the CNT network structure in the process of injection molding.

In the second experiment, we followed agglomeration and deagglomeration processes by applying oscillatory deformation to the same composites. The strain amplitudes were chosen to be below and above the critical one, i.e. in linear and nonlinear viscoelastic regime. We found that both the storage and loss moduli of the as-received samples considerably increase in the linear regime. There are at least two recovery processes. One is relatively fast, with the relaxation time of about 50 s, which corresponds presumably to the formation of carbon nanotubes agglomerates. The second process is extremely slow, with the relaxation time of several hours (a steady state is not achieved within the experimental time scale). This second recovery process is very likely caused by the gradual rearrangement of a whole network structure, although a definite conclusion can be only made after performing additional morphological studies, for example in-situ Rheo-SAXS measurements. When the strain amplitude is noticeably higher than the critical one, the network structure is effectively destroyed which results in a fast drop of both moduli, whereby the storage modulus becomes lower than the loss modulus. We have tried to reproduce the flocculation experiment in the frame of a modified Maxwell model capable of describing phenomenologically the transition from liquid-like to solid-like behavior in highly filled nanocomposites. The modified Maxwell model predicts reasonably well the time evolution of storage modulus, however there is a noticeable discrepancy between the theoretical description and the measured data for the loss modulus.

In overall, we can say that the main process influencing the viscoelastic properties of the MWNT-polycarbonate composites is the agglommeration-deagglommeration of nanotubes. Presumably, a main reason of suppression of the nanotube reorientation, both under shearing in the ARES rheometer and during the recovery process, is strong attractive interactions between the carbon nanotubes leading to their agglomeration into the viscoelastic clusters. We should admit that the modeling of aggregating filled systems, especially those composed from anisometric particles, is a difficult (maybe unsolved) task. However, we think that the superposition approach proposed here represents an essential step foreword as it can account not only for agglomeration but also for orientation effects which can become very pronounced during the melt processing of polymer nanocomposites. In the frame of superposition approach the orientation effects can be accounted for by using in Equation (2) instead of a constant reinforcement factor $X$ an additional contribution described by the Folgar-Tucker orientation model [7]. The modelling itself is very important in industrial applications of CNT based polymer composites and is planned to be implemented in commercial programs for description of the injection molding process.

## Acknowledgements

This work was carried out with the support of the BMBF Project 'CarboNet' No. 03X0504E. Bayer Technology Services GmbH (Leverkusen, Germany) is greatly acknowledged for providing the samples for rheological measurements. Further, we would like to thank Dr. Klaus Schröter (Martin-Luther-University of Halle-Wittenberg, Germany) for very helpful discussions concerning the experimental rheological work. The authors are very grateful to Mr. Torsten Hofmann (Leibniz-Institut für Polymerforschung Dresden e.V., Germany) for carrying out the X-ray scattering measurements. Dr. Petra Pötschke (Leibniz-Institut für Polymerforschung Dresden e.V., Germany) and Dr. Gilles Ausias and Mr. Ronan Simon (Université de Bretagne-Sud, Lorient, France) are greatly acknowledged for fruitful discussions.

## References

[1] Nalwa H. S.: Polymeric nanostructures and their applications. American Scientific Publishers, Los Angeles (2007).

[2] Heinrich G., Klüppel M.: Recent advances in the theory of filler networking in elastomers. Advances in Polymer Science, **160**, 1–44 (2002).
DOI: 10.1007/3-540-45362-8_1

[3] Fan Z., Advani S. G.: Rheology of multiwall carbon nanotubes suspensions. Journal of Rheology, **51**, 585–604 (2007).
DOI: 10.1122/1.2736424

[4] Pegel S., Pötschke P., Petzold G., Alig I., Dudkin S. M., Lellinger D.: Dispersion, agglomeration, and network formation of multiwalled carbon nanotubes in polycarbonate melts. Polymer, **49**, 974–984 (2008).
DOI: 10.1016/j.polymer.2007.12.024

[5] Ray S. S., Okamoto M.: Polymer/layered silicate nanocomposites: A review from preparation to processing. Progress in Polymer Science, **28**, 1539–1641 (2003).
DOI: 10.1016/j.progpolymsci.2003.08.002

[6] Moniruzzaman M., Winey K. I.: Polymer nanocomposites containing carbon nanotubes. Macromolecules, **39**, 5194–5205 (2006).
DOI: 10.1021/ma060733p

[7] Lertwimolnun W., Vergnes B., Ausias G., Carreau P. J.: Stress overshoots of organoclay nanocomposites in transient shear flow. Journal of Non-Newtonian Fluid Mechanics, **141**, 167–179 (2007).
DOI: 10.1016/j.jnnfm.2006.11.003

[8] Costa F. R., Saphiannikova M., Wagenknecht U., Heinrich G.: Layered double hydroxide based polymer nanocomposites. Advances in Polymer Science, **210**, 101–168 (2008).
DOI: 10.1007/12_2007_123

[9] Huang Y. Y., Ahir S. V., Terentjev E. M.: Dispersion rheology of carbon nanotubes in a polymer matrix. Physical Review B, **73**, 125422/1–125422/9 (2006).
DOI: 10.1103/PhysRevB.73.125422

[10] Pötschke P., Fornes T. D., Paul D. R.: Rheological behaviour of multiwalled carbon nanotube/polycarbonate composites. Polymer, **43**, 3247–3255 (2002).
DOI: 10.1016/S0032-3861(02)00151-9

[11] Ren J., Silva A. S., Krishnamoorti R.: Linear viscoelasticity of disordered polystyrene-polyisoprene block copolymer based layered-silicate nanocomposites. Macromolecules, **33**, 3739–3746 (2000).
DOI: 10.1021/ma992091u

[12] Solomon M. J., Almusallam A. S., Seefeldt K. F., Somwangthanaroj A., Varadan P.: Rheology of polypropylene/clay hybrid materials. Macromolecules, **34**, 1864–1872 (2001).
DOI: 10.1021/ma001122e

[13] Liu A. J., Nagel S. R.: Nonlinear dynamics: Jamming is not just cool any more. Nature, **396**, 21–22 (1998).
DOI: 10.1038/23819

[14] Trappe V., Prasad V., Cipelletti L., Serge P. N., Weitz D. A.: Jamming phase diagram for attractive particles. Nature, **411**, 772–775 (2001).
DOI: 10.1038/35081021

[15] Winter H. H., Mours M.: The cyber infrastructure initiative for rheology. Rheologica Acta, **45**, 331–338 (2005).
DOI: 10.1007/s00397-005-0041-7

[16] Baumgaertel M., Winter H. H.: Determination of discrete relaxation and retardatation time spectra from dynamic mechanical data. Rheologica Acta, **28**, 511–519 (1989).
DOI: 10.1007/BF01332922

[17] Leonov A. I.: On the rheology of filled polymer melts. Journal of Rheology, **34**, 1039–1068 (1990).
DOI: 10.1122/1.550109

[18] Doi M., Edwards S. F.: The theory of polymer dynamics. Oxford University Press, Oxford (1988).

[19] Thomasset J., Carreau P. J., Sanschagrin B., Ausias G.: Rheological properties of long glass fiber filled polypropylene. Journal of Non-Newtonian Fluid Mechanics, **125**, 25–34 (2005).
DOI: 10.1016/j.jnnfm.2004.09.004

[20] Simhambhatla M., Leonov A. I.: On the rheological modeling of filled polymers with particle-matrix interactions. Rheologica Acta, **34**, 329–338 (1995).
DOI: 10.1007/BF00367150

[21] Bird R. B., Armstrong R. C., Hassager O.: Dynamics of polymeric fluids. Wiley, New York (1987).

[22] Bastian H.: Non-linear viscoealsticity of linear and long-chain branched polymer melts in shear and extensional flows. PhD thesis, Stuttgart University (2001).

[23] Wagner M. H., Rubio P., Bastian H.: The molecular stress function model for polydisperse polymer melts with dissipative convective constraint release. Journal of Rheology, **45**, 1387–1412 (2001).
DOI: 10.1122/1.1413503

[24] Lu J. P.: Elastic properties of carbon nanotubes and nanoropes. Physical Review Letters, **79**, 1297–1300 (1997).
DOI: 10.1103/PhysRevLett.79.1297

[25] Dullaert K., Mewis J.: A structural kinetics model for thixotropy. Journal of Non-Newtonian Fluid Mechanics, **139**, 21–30 (2006).
DOI: 10.1016/j.jnnfm.2006.06.002

[26] Yziquel F., Carreau P. J., Moan M., Tanguy P. A.: Rheological modelling of concentrated colloidal suspension. Journal of Non-Newtonian Fluid Mechanics, **86**, 133–155 (1999).
DOI: 10.1016/S0377-0257(98)00206-7

[27] Saphiannikova M., Costa F. R., Wagenknecht U., Heinrich G.: Nonlinear behaviour of the polyethylene/layered double hydroxide nanocomposites under shear flow. Polymer Science Series A, **50**, 573–582 (2008).
DOI: 10.1134/S0965545X0805012X

[28] Sobhanie M., Isayev A. I.: Modeling and experimental investigation of shear flow of a filled polymer. Journal of Non-Newtonian Fluid Mechanics, **85**, 189–212 (1999).
DOI: 10.1016/S0377-0257(99)00002-6

[29] Coussot P., Leonov A. I., Piau J. M.: Rheology of concentrated dispersed system in a low molecular weight matrix. Journal of Non-Newtonian Fluid Mechanics, **46**, 179–217 (1993).
DOI: 10.1016/0377-0257(93)85046-D

[30] Alig I., Skipa T., Lellinger D., Bierdel M., Meyer H.: Dynamic percolation of carbon nanotube agglomerates in a polymer matrix: Comparison of different model approaches. Physica Status Solidi (b), **245**, 2264–2267 (2008).
DOI: 10.1002/pssb.200879622

*eXPRESS Polymer Letters Vol.3, No.12 (2009) 769–777*
*Available online at www.expresspolymlett.com*
*DOI: 10.3144/expresspolymlett.2009.95*

# Temperature dependence of the electrical properties of the carbon nanotube/polymer composites

*Q. Li*[1,2], *Q. Z. Xue*[1*], *X. L. Gao*[1], *Q. B. Zheng*[1]

[1]College of Physics Science and Technology, China University of Petroleum, Dongying, Shandong 257061, People's Republic of China
[2]Department of Materials and Chemical Engineering, Taishan University, Tai'an, Shandong 271021, People's Republic of China

*Received 17 July 2009; accepted in revised form 4 September 2009*

---

**Abstract.** In this paper, pristine and oxidized multi-walled carbon nanotube (MWCNT)/poly(vinylidene fluoride) (PVDF) composites were prepared and the temperature dependence of some electrical properties of these composites were studied. It is found that the transition temperature ($T_t$), from positive temperature coefficient (PTC) to negative temperature coefficient (NTC) effect, of the oxidized MWCNT/PVDF composites shifted to a higher temperature. The shift of the $T_t$ of the oxidized MWCNT/PVDF composites can be attributed to the chemical functionalization of the MWCNTs. The dielectric constants of these composites are enhanced remarkably, which can be understood by the interfacial polarization effect. The largest dielectric constant of 3600 is obtained in the composite with about 8 vol% oxidized MWCNTs at 1 kHz. The dielectric constants of these composites increase firstly and then decrease with increasing temperature. However, when the temperature reaches a higher value, the dielectric constants increase again with increasing temperature. The 'wave' phenomenon of the temperature dependence of the dielectric constants can be understood by the temperature dependence of the interfacial polarization.

***Keywords:*** *polymer composites, carbon nanotube, electrical properties, thermal properties*

---

## 1. Introduction

It is well known that the resistance of the carbon black (CB) or other conductive particle filled semi-crystalline polymer composites exhibits a sharp increase when the temperature reaches the melting temperature ($T_m$) of the polymers. This phenomenon is referred as the positive temperature coefficient (PTC) effect. When the temperature is above $T_m$, the resistance of the composites will decrease. This is the negative temperature coefficient (NTC) effect. The PTC effect and NTC effect of the CB-filled semi-crystalline polymer composites have been investigated for a long time. In recent years, the relative factors of the PTC and NTC effects of CB-filled semi-crystalline polymer composites have been studied in detail [1–4]. The results showed that both the molecular weight of the polymer matrix and the size of CB could influence the percolation threshold and the PTC temperature, at which a sharp increase of the resistance of these composites occurs. Zhang *et al*. [4] studied the electrical properties of the CB-filled ultra-high molecular weight polyethylene (UHMWPE). They found that the percolation threshold of these composites decreases with the increase of the molecular weight of UHMWPE, and with the decrease of the particle size of CB. The PTC temperature of the CB-filled UHMWPE composite with the UHMWPE molecular weight of 145 millions decreases with the increase of CB size. The PTC composites have

---

[*]Corresponding author, e-mail: xueqingzhong@tsinghua.org.cn

many important applications, such as the over-current protectors and sensors. However, CB-filled polymer composites require a high CB concentration. This means that the excellent properties of the polymer matrix will be influenced.

Since the discovery of carbon nanotubes (CNTs) in 1991, they have been widely studied in several fields because of their extraordinary properties [5]. CNT/polymer composite is one of the important applications of the CNTs [6, 7]. The properties of the CNT/polymer composites will be enhanced remarkably with small CNT concentration. The application of the CNT/polymer composites under different temperatures is the problem that we must think about. He *et al.* [8] studied the temperature dependence of electrical properties of the multi-walled carbon nanotube (MWCNT) filled high density polyethylene (HDPE) composites, and found an obvious PTC effect and a less obvious NTC effect in these composites with a low MWCNT concentration. The PTC intensity of the MWCNT/HDPE composite with 5.4 wt% MWCNTs reached $10^4$. After $\gamma$-ray irradiation, the NTC effect of these composites could be further eliminated. Poly(vinylidene fluoride) (PVDF) and its copolymers, as semi-crystalline polymer materials, have attracted more attention for their broad applications in electromechanical systems [9, 10]. The mechanical properties of the PVDF polymer are better than those of the polyethylene (PE), which is the traditional PTC polymer. And the $T_m$ of PVDF is also higher than that of PE, which means that the application range is wider than that of PE polymer.

In this paper, we investigated the temperature dependence of electrical properties of the pristine and oxidized MWCNT/PVDF composites. Because of the high aspect ratio, the percolation threshold is much smaller than that of CB filled polymer composites. The dielectric constant of these composites is enhanced remarkably. The temperature dependence of electrical properties of these composites showed that the transition temperature ($T_t$), from PTC effect to NTC effect, of the oxidized MWCNT/PVDF composites shifted to a higher temperature. The dielectric constants of these composites increase with increasing temperature, and then decrease. However, the dielectric constants increase again when the temperature reaches a higher temperature. The temperature dependence of the dielectric constants indicated a 'wave' phenomenon.

## 2. Experimental section

### 2.1. Materials

The MWCNTs (purity > 95 wt%, diameter 10–20 nm, length about 30 µm, density 2.1 g/cm$^3$) synthesized by Chemical Vapor Deposition were purchased from Chengdu Organic Chemistry Co. Ltd., Chinese Academy of Science. The PVDF powder (particle size about 50 µm, density 1.7 g/cm$^3$) was purchased from 3F Co. Ltd., Shanghai, China. The ethanol (AR), concentrated nitric acid (AR), and concentrated sulfuric acid (AR) were purchased from Tianjin Chemical Co. Ltd., China. Ultrasonicator (HK2200, 100W) was purchased from High Kugod Science Instrument Co. Ltd., Shanghai, China. LCR digital meter (TH2828) was purchased from Tonghui Electronic Co. Ltd., Changzhou, China. Deionized water was supplied by the University of Petroleum, China.

### 2.2. Sample preparation

Briefly, 1 g of the pristine MWCNTs was suspended in 100 ml mixture of concentrated sulfuric acid and concentrated nitric acid (3:1 [v/v]) for 6 h with the ultrasonicator. The MWCNTs were filtrated and washed with deionized water until pH 5–7, and then dried at 55°C in a vacuum for 8 h [11, 12]. The oxidized MWCNTs were obtained.

In order to form a stable suspension, the pristine and oxidized MWCNTs were ultrasonically dispersed in ethanol for 3 h respectively. Then the PVDF powder was poured into this suspension. The PVDF powder was swollen by ethanol and the mixture was ultrasonically dispersed for another 2 h. The mixture was dried for 3 h at 70°C to remove any excess ethanol. The agglomerates of these composites were broken into powder. The composite powder was cold pressed to disk-shape sample with 15 mm in diameter and 2 mm in thickness at 20 MPa. Then the samples were kept at 200°C for 3 h [13, 14].

### 2.3. Measurements

All samples were polished to control their flatness, and silver paste was painted on both sides of the samples to get an ohmic contact with the electrodes. The alternating current (ac) electrical properties of the samples were measured by using two-probe method with LCR digital meter in the

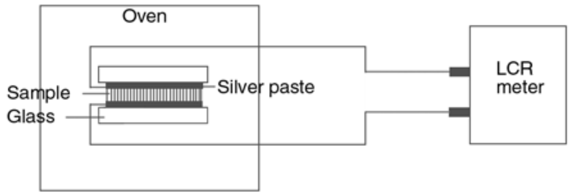

**Figure 1.** The scheme of the measurement of the electrical properties at different temperatures

frequency range of 20–$10^6$ Hz at room temperature. The temperature dependence of the electrical properties was measured by putting the samples in an oven [4]. Figure 1 illustrates the measurement system.

## 3. Results and discussion

### 3.1. Characterization of CNTs and composites

Figure 2 shows the transmission electron microscopy (TEM) images of the pristine and oxidized MWCNTs and the scanning electron microscope (SEM) images of the pristine and oxidized MWCNT/PVDF composites in our experiment. As shown in Figures 2a and 2b, the impurity, for instance the amount of amorphous carbon materials and catalysts, in oxidized MWCNTs is less than that in pristine MWCNTs. The MWCNTs were purified. The length of the MWCNTs became shorter by the chemical functionalization. Figures 2c and 2d show the SEM images of the composite sections, which indicate that the MWCNTs were dispersed in the PVDF matrix homogeneously.

### 3.2. Electrical properties of these composites

Figure 3 shows the electrical conductivity and the dielectric constants of the pristine and oxidized MWCNT/PVDF composites as a function of the volume fraction of the MWCNTs measured at room temperature and 1 kHz. The electrical conductivity of these two kinds of composites increased significantly with low MWCNT concentration. The conductivity can be analyzed with the critical MWCNT concentration, percolation threshold $p_c$, by the following scaling law [14–16] (Equation (1)):

$$\sigma_{eff} \propto \sigma_i (p_c - p_{\mathrm{MWCNT}})^{-s'}, \text{ for } p_c > p_{\mathrm{MWCNT}} \qquad (1)$$

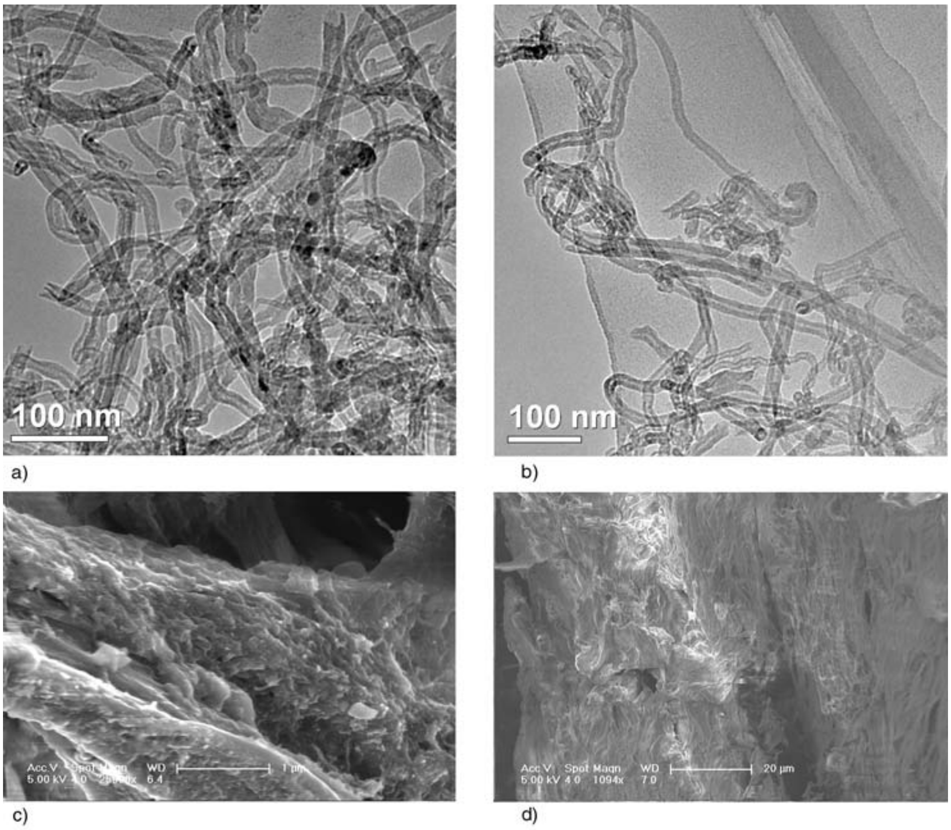

**Figure 2.** TEM images of a) pristine; and b) oxidized MWCNTs; SEM images of c) pristine, and d) oxidized MWCNT/PVDF composite sections

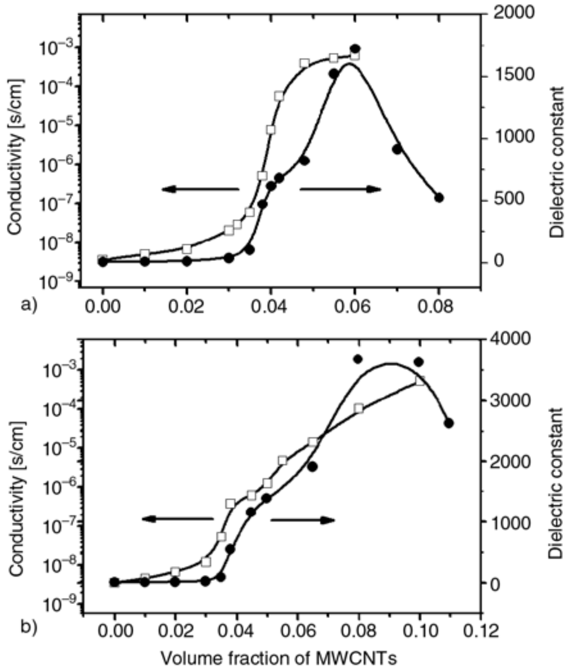

**Figure 3.** Dependence of the electrical conductivity and dielectric constant of a) pristine MWCNT/PVDF composites; and b) oxidized MWCNT/PVDF composites on the MWCNT concentration

The percolation threshold of these composites by calculating is about 3.8 vol%. The conductivity of the pristine MWCNT/PVDF composites increases remarkably near the percolation threshold, and exhibits a typical insulator-conductor transition. However, the conductivity of the chemically functionalized MWCNT/PVDF composites increases slowly with increasing the MWCNT volume fraction. The reason for the electrical properties of these composites can be attributed to the tunneling conduction mechanism and percolation phenomenon. The carboxylic groups on the surface of MWCNTs can decrease the tunneling currents. In other words, it becomes difficult for the tunneling event to occur, if there are carboxylic groups between MWCNTs. Therefore, the tunneling current will decrease relatively, and the conductivity will increase slightly with increasing MWCNT concentration [14–16].

The dielectric constant increases remarkably when the concentration of MWCNTs approaches to about 6 and 8 vol% for the pristine and oxidized MWCNT/PVDF composites, respectively, and then the dielectric constants decrease with increasing MWCNTs concentration. As we noted, the largest dielectric constants of these two kinds of composites are different. The largest dielectric constant of the pristine MWCNT/PVDF composites is 1700, with about 6 vol% MWCNTs at 1 kHz. However, it reaches 3600 for the oxidized MWCNT/PVDF composite with about 8 vol% oxidized MWCNTs.

The dielectric properties of the composites can be understood by the percolation theory and interfacial polarization effect. In these composites, the MWCNTs were distributed in the insulting matrix, which can form a lot of interfaces. For these composites, a thin insulating layer of PVDF was combined with the MWCNTs to form the nanoscale structure in these composites. The large Π-orbital of the MWCNTs could provide large domains for nomadic electrons. These electrons can be orientated under electric field, and interfacial polarization can take place [15]. As the MWCNT concentration increases, the number of the interfaces increases. So dielectric constant increases with increasing MWCNT concentration. When the concentration of MWCNTs is larger than the percolation threshold of the composites, some MWCNTs will connect with each other, and even agglomerated again. The interfaces between the MWCNTs and the PVDF will decrease. The dielectric constant will decrease with further increasing MWCNT concentration.

The different largest dielectric constant of these two kinds of composites can be attributed to the chemical functionalization. Compared with the pristine MWCNTs, the length of the MWCNTs became shorter by the chemical functionalization, so that there will need more MWCNTs to form the conductive nets. So the interfaces formed between the oxidized MWCNTs and PVDF matrix will be larger than that between pristine MWCNTs and PVDF matrix. Moreover the carboxylic groups are the electron-withdrawing groups, and this will strengthen interfacial polarization. Therefore, the different largest dielectric constants of MWCNT/PVDF composites can be attributed to the different MWCNT concentration and the chemical functionalization [16].

Furthermore, the measured dielectric constant values show a divergence at the percolation threshold. The reasons of these changes of dielectric constants in the neighborhood of the percolation threshold may be caused by this factor. As shown in Figure 3, the percolation transition region is wide, the variation of dielectric constants will occur in the percolation transition region, and the percolation threshold calculated by Equation (1) is only the beginning value of the percolation transition scope. This caused the divergence [15, 16].

### 3.3. Temperature dependence of the impedance

Figure 4 shows the temperature dependence of impedance of these two kinds of MWCNT/PVDF composites. As shown in this figure, the PTC and NTC effects of these composites are both small. The impedance of the composites at $T_t$ is only 2–4 times larger than that at room temperature.

It has been accepted that the PTC effect is due to the different thermal expansion coefficients of the polymer matrix and the filler [1–4]. At lower temperature the conductive fillers imbedded in the insulator can connect with each other, which form the conducting paths. When the temperature is lower than $T_t$, the expansion of the polymer matrix will separate the fillers that connected with each other before, and the impedance of the composites increases with increasing temperature. When the temperature is higher than $T_t$, the PVDF crystalline phase begins to melt, transforming from a semi-crystalline phase to the rubbery flow region. Therefore, the fluidity of the polymer matrix and the mobility of the MWCNTs will be enhanced in rubbery flow region. This will make it easier for the fillers to connect with each other than before so that the impedance decreases with a further increasing temperature. On the other hand, the electrons will capture more energy when the temperature increases, and they can overcome the potential barrier easily. So the impedance decreases with increasing temperature. The small temperature coefficients of the MWCNT/PVDF composites can be attributed to the one-dimension structure of CNTs and the conducting network formed by the MWCNTs in composites. At low temperature, the MWCNTs contacted each other in the PVDF matrix. Because of the one-dimension structure of the CNTs, the contact probability of one CNT and anthor CNT is larger than that between two CB particles. Compared with the CB network, CNT network is very difficult to disconnect because of the connection with each other. This reason caused the small PTC effect of these composites.

As shown in Figure 4b, the impedance-temperature curves show that the $T_t$ of the oxidized MWCNT/PVDF composites shifts to a higher temperature. However, as shown in Figure 5, the DSC curves show that the $T_m$ of these two kinds of composite powders is approximately equal. The $T_m$ of the pure PVDF is slightly higher than the composites. MWCNTs can be considered as the nucleation agent and improve the crystallinity of the polymer matrix. The defects of the polymer matrix crystal

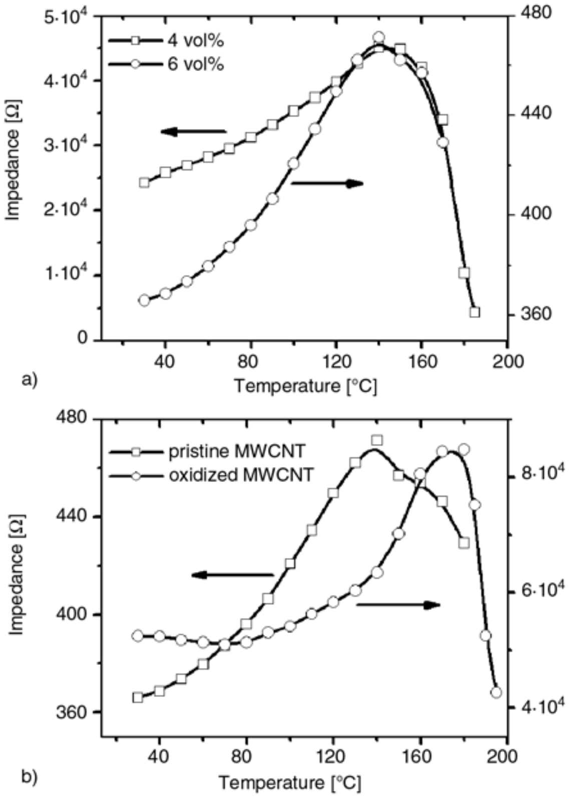

**Figure 4.** Temperature dependence of the impedance for these two kinds of MWCNT/PVDF composites; a) 4 and 6 vol% pristine MWCNT/PVDF composites, b) 6 vol% pristine and oxidized MWCNT/PVDF composites

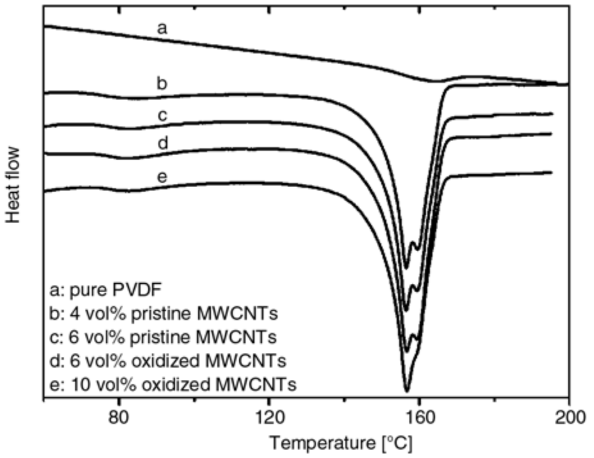

**Figure 5.** DSC curve of the pure PVDF and the MWCNT/PVDF composites with various MWCNT concentration

may be introduced by the MWCNTs, and the lamellae thickness may be slightly reduced. So the $T_m$ of the composites was decreased slightly [17]. According to the polymer theory, the $T_t$ should be approximately equal to $T_m$ of the polymer. We think that there are two reasons for this difference. Firstly, the interface effect between the MWCNTs and the PVDF matrix [18]. The carboxylic acid groups were introduced to the surface of the MWCNTs in the oxidized MWCNT/PVDF composites. The thermal interfacial resistance between MWCNTs and polymer matrix can be reduced. The thermal conductance property of oxidize MWCNT/PVDF composites is better than that of pristine MWCNT/PVDF composites. So this will consume more thermal energy to melt polymer matrix [18–21]. Secondly, the carboxylic groups on the surface of the MWCNTs can be imbedded into the polymer matrix, which cause the oxidized MWCNT/PVDF composites to be more compact. So the $T_t$ of the oxidized MWCNT/PVDF composites shifts to a higher temperature. In a word, the interface effect between the oxidized MWCNTs and the polymer matrix may be the major reason for the change of the $T_t$.

### 3.4. Temperature dependence of dielectric properties

The temperature dependence of the dielectric properties of the pristine and oxidized MWCNT/PVDF composites are shown in Figure 6. The dielectric constants increase firstly, and then decrease with increasing temperature. After that, the dielectric constants increase again with increasing temperature when the temperature reaches a higher temperature. The dielectric loss decrease first, and then increase with increasing temperature. All the specimens have the similar properties. In order to find out the mechanism of the temperature dependence of the dielectric properties, we investigated the temperature dependences of the impedance and dielectric properties of the pure PVDF matrix. Figure 7 shows the temperature dependences of the impedance and dielectric properties of the pure PVDF matrix at 1 kHz. As shown in Figure 7, the temperature dependence of the dielectric constants of the PVDF matrix shows the same 'wave' phenomenon.

Electric modulus formalism is a good method to study the polarization effect. The electric modulus can be calculated by the Equation (2) [22, 23]:

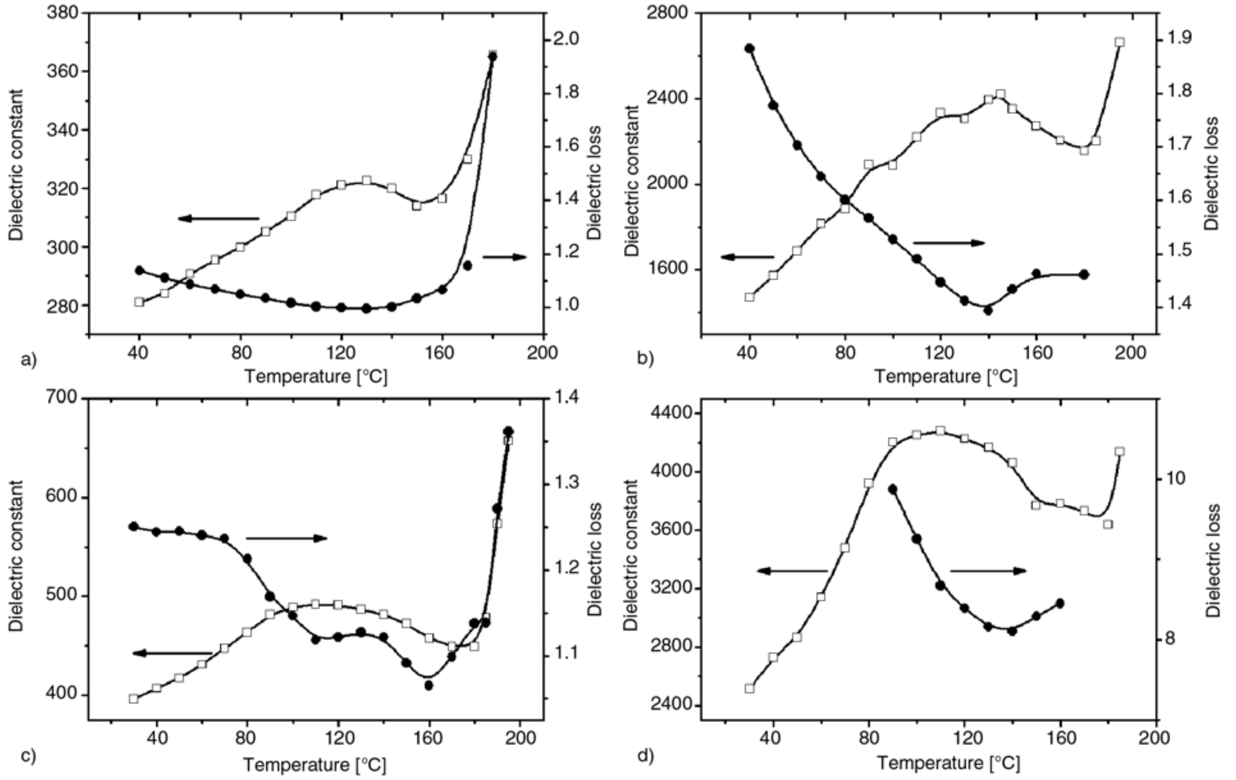

**Figure 6.** Temperature dependence of the dielectric constants and dielectric loss of a) 4 vol%, b) 6 vol% pristine MWCNT/PVDF composites; and c) 6 vol%, d) 10 vol% oxidized MWCNT/PVDF composites at 1 kHz

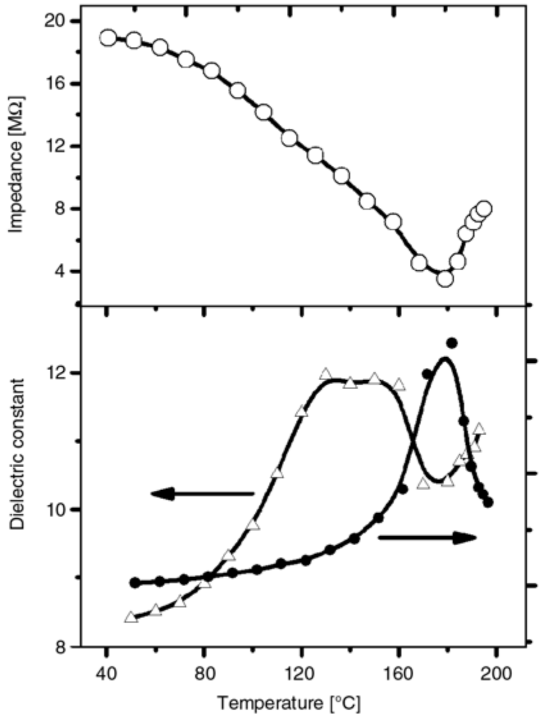

**Figure 7.** Temperature dependence of the electrical properties of the pure PVDF matrix

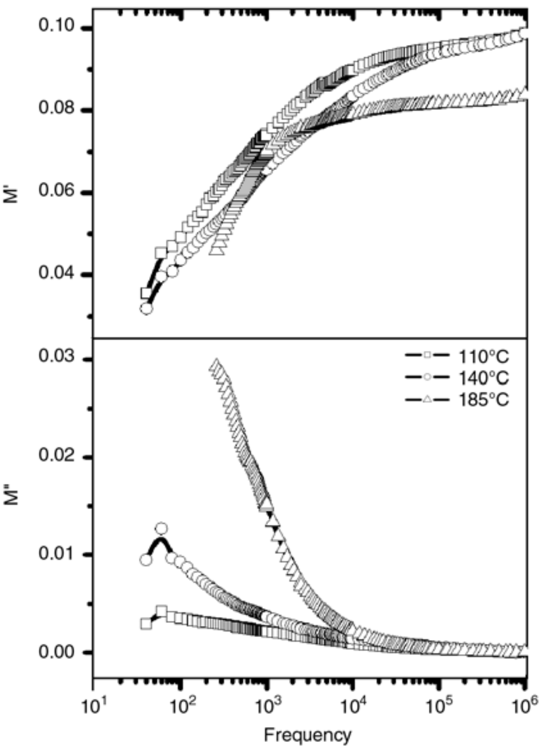

**Figure 8.** Real $M'$ and imaginary $M''$ of the electric modulus formalism of the pure PVDF versus frequency at different temperatures

$$M^* = (\varepsilon^*)^{-1} = M' + iM'' = \frac{\varepsilon'}{\varepsilon'^2 + \varepsilon''^2} + i\frac{\varepsilon''}{\varepsilon'^2 + \varepsilon''^2} \tag{2}$$

Because of the instrument precision, we do not get the values of the electric modulus of the MWCNT/PVDF composites at low frequency. The electric modulus formalism of the pure PVDF is calculated. Figure 8 shows the electric modulus formalism of the pure PVDF. As shown in this figure, the values of real components ($M'$) increase with frequency and reach a constant value as expected. The values of imaginary components ($M''$) show a peak at low frequency at 110 and 140°C. Relaxation peaks are attributed to an interfacial polarization process. According to the electric modulus formalism of the pure PVDF matrix, the temperature frequency of dielectric properties of the MWCNT/PVDF composites can be explained as follows [24, 25]. When the temperature is lower than $T_t$, the expansion of the polymer matrix will separate the fillers that connected with each other before. The interfaces between the MWCNTs and the polymer matrix will increase, and the dielectric constant will increase. When the temperature is higher than $T_t$, the PVDF crystalline phase begins to melt, transforming from a semi-crystalline phase to the rubbery flow region. This will make it easier for the fillers to connect with each other. The interfaces between the MWCNTs and the polymer matrix will decrease. So the dielectric constant will decrease. However, the nomadic electrons will get larger energy and agglomerated on the interfaces at higher temperatures because the fluorine atom is an electron-withdrawing group. The polarization will be enlarged, even exceed the influence of MWCNTs connect again. The dielectric constant increases again. We do not get the values of the electric modulus of the PVDF composites at higher temperatures (for example 185°C) at low frequency for the reason of instrument precision. So the electrode effect should also be considered for the later increase.

## 4. Conclusions

The pristine and oxidized MWCNT/PVDF composites were fabricated by solution blending. The percolation threshold of these composites is smaller than that of CB filled polymer composites. The dielectric constant of the composites was enhanced remarkably, which can be understood by interfacial polarization effect. The temperature dependence of impedance of these MWCNT/PVDF composites indicates that the PTC and NTC effects of these two kinds of composites are small. Because of the functionalization of the MWCNTs, the transition temperature, from positive temperature coefficient to negative temperature coefficient effect, of the oxidized MWCNT/PVDF composites is larger than that of the pristine MWCNT/PVDF composites. The dielectric constants of these composites increase firstly and then decrease with increasing temperature. However, when the temperature reaches a higher temperature, the dielectric constants increase again with increasing temperature. The 'wave' phenomenon of the temperature dependence of these dielectric constants can be attributed to the interfacial polarization under different temperatures.

## Acknowledgements

This work is supported by 973 National Basic Research Program under Contract No. 2008CB617508, and the Cultivation Fund of the Key Scientific and Technical Innovation Project (No. 708061), Ministry of Education of China, and Program for New Century Excellent Talents in University (NCET-08-0844).

## References

[1] Feng J., Chan C-M.: Double positive temperature coefficient effects of carbon black-filled polymer blends containing two semicrystalline polymers. Polymer, **41**, 4559–4565 (2000).
DOI: 10.1016/S0032-3861(99)00690-4

[2] Feng J., Chan C-M.: Positive and negative temperature coefficient effects of an alternating copolymer of tetrafluoroethylene-ethylene containing carbon black filled HDPE particles. Polymer, **41**, 7279–7282 (2000).
DOI: 10.1016/S0032-3861(00)00095-1

[3] Hindermann-Bischoff M., Ehrburger-Dolle F.: Electrical conductivity of carbon black-polyethylene composites experimental evidence of the change of cluster connectivity in the PTC effect. Carbon, **39**, 375–382 (2001).
DOI: 10.1016/S0008-6223(00)00130-5

[4] Zhang C., Ma C. A., Wang P., Sumita M.: Temperature dependence of electrical resistivity for carbon black filled ultra-high molecular weight polyethylene composites prepared by hot compaction. Carbon, **43**, 2544–2553 (2005).
DOI: 10.1016/j.carbon.2005.05.006

[5] Iijima S.: Helical microtubules of graphitic carbon. Nature, **354**, 56–58 (1991).
DOI: 10.1038/354056a0

[6] Sandler J., Shaffer M. S. P., Prasse T., Bauhofer W., Schulte K., Windle A. H.: Development of a dispersion process for carbon nanotube in an epoxy matrix and the resulting electrical properties. Polymer, **40**, 5967–5971 (1999).
DOI: 10.1016/S0032-3861(99)00166-4

[7] Barrau S., Demont P., Peigney A., Laurent C., Lacabanne C.: DC and AC conductivity of carbon nanotube-polyepoxy composites. Macromolecules, **36**, 5187–5194 (2003).
DOI: 10.1021/ma021263b

[8] He X. J., Du J. H., Ying Z., Cheng H. M., He X. J.: Positive temperature coefficient effect in multiwalled carbon nanotube/high-density polyethylene composites. Applied Physics Letters, **86**, 062112/1–062112/3 (2005).
DOI: 10.1063/1.1863452

[9] Zhao X-Z., Bharti V., Zhang Q. M., Romotowski T., Tito F., Ting R.: Electromechanical properties of electrostrictive poly(vinylidene fluoride-trifluoroethylene) copolymer. Applied Physics Letters, **73**, 2054–2056 (1998).
DOI: 10.1063/1.122365

[10] Huang C., Zhang Q. M., Su J.: High-dielectric constant all-polymer percolative composites. Applied Physics Letters, **82**, 3502–3504 (2003).
DOI: 10.1063/1.1575505

[11] Li S., Qin Y., Shi J., Guo Z. X., Li Y., Zhu D.: Electrical properties of soluble carbon nanotube/polymer composite films. Chemistry of Materials, **17**, 130–135 (2005).
DOI: 10.1021/cm0491025

[12] Kim Y. J., Shin T. S., Choi H. D., Kwon J. H., Chung Y-C., Yoon H. G.: Electrical conductivity of chemically modified multiwalled carbon nanotube/epoxy composites. Carbon, **43**, 23–30 (2005).
DOI: 10.1016/j.carbon.2004.08.015

[13] Owens F. J., Jayakody J. R. P., Greenbaum S. G.: Characterization of single walled carbon nanotube: Polyvinylene difluoride composites. Composites Science and Technology, **66**, 1280–1284 (2006).
DOI: 10.1016/j.compscitech.2005.10.027

[14] Wang L., Dang Z-M.: Carbon nanotube composites with high dielectric constant at low percolation threshold. Applied Physics Letters, **87**, 042903/1–042903/3 (2005).
DOI: 10.1063/1.1996842

[15] Dang Z., Wang L., Yin Y., Zhang Q., Lei Q.: Giant dielectric permittivities in functionalized carbon-nanotube/electroactive-polymer nanocomposites. Advanced Materials, **19**, 852–857 (2007).
DOI: 10.1002/adma.200600703

[16] Li Q., Xue Q., Hao L., Gao X., Zheng Q.: Large dielectric constant of the chemically functionalized carbon nanotube/polymer composites. Composites Science and Technology, **68**, 2290–2296 (2008). DOI: 10.1016/j.compscitech.2008.04.019

[17] Zhang S., Zhang N., Huang C., Ren K., Zhang Q.: Microstructure and electromechanical properties of carbon nanotube/poly(vinylidene fluoride trifluoroethylene chlorofluoro ethylene) composites. Advanced Materials, **17**, 1897–1901 (2005). DOI: 10.1002/adma.200500313

[18] Shenogin S., Bodapati A., Xue L., Ozisik R., Keblinski P.: Effect of chemical functionalization on thermal transport of carbon nanotube composites. Applied Physics Letters, **85**, 2229–2231 (2004). DOI: 10.1063/1.1794370

[19] Liu C. H., Fan S. S.: Effects of chemical modifications on the thermal conductivity of carbon nanotube composites. Applied Physics Letters, **86**, 123106/1–123106/3 (2005). DOI: 10.1063/1.1887839

[20] Yu A., Itkis M. E., Bekyarova E., Haddon R. C.: Effect of single-walled carbon nanotube purity on the thermal conductivity of carbon nanotube-based composites. Applied Physics Letters, **89**, 133102/1–133102/3 (2006). DOI: 10.1063/1.2357580

[21] Xu Y., Ray G., Abdel-Magid B.: Thermal behavior of single-walled carbon nanotube polymer-matrix composites. Composites Part A: Applied Science and Manufacturing, **37**, 114–121 (2006). DOI: 10.1016/j.compositesa.2005.04.009

[22] Tsangaris G. M., Psarras G. C., Kouloumbi N.: Electric modulus and interfacial polarization in composite polymeric systems. Journal of Materials Science, **33**, 2027–2037 (1998). DOI: 10.1023/A:1004398514901

[23] Abdul-Jawad S., Alnajjar A., Abdallah M. H.: AC impedance, permittivity and modulus spectroscopy of lead chloride single crystal. Applied Physics A: Materials Science and Processing, **64**, 199–201 (1997). DOI: 10.1007/s003390050464

[24] Yu S., Hing P., Hu X.: Dielectric properties of polystyrene-aluminum-nitride composites. Journal of Applied Physics, **88**, 398–404 (2000). DOI: 10.1063/1.373672

[25] Bobnar V., Levstik A., Huang C., Zhang Q. M.: Enhanced dielectric response in all-organic polyaniline poly(vinylidene fluoride-trifluoroethylene-chlorotrifluoroethylene) composite. Journal of Non-Crystalline Solids, **353**, 205–209 (2007). DOI: 10.1016/j.jnoncrysol.2006.10.003

*eXPRESS Polymer Letters Vol.3, No.12 (2009) 778–787*
*Available online at www.expresspolymlett.com*
*DOI: 10.3144/expresspolymlett.2009.96*

# A new approach to the synthesis of hydrophobically associating polyacrylamide via the inverse miniemulsion polymerization in the presence of template

*L. X. Gong*, X. F. Zhang*

College of Material Science & Engineering, Beijing Institute of Technology, Beijing 100081, China

*Received 31 July 2009; accepted in revised form 4 September 2009*

**Abstract.** Cationic, hydrophobically associating polyacrylamide (PDA) was synthesized via the inverse miniemulsion polymerization in the presence of template. Dimethyloctane(2- acrylamidopropyl)ammoniumbromide (DOAB) was synthesized via quaternization reaction and used as the hydrophobic monomer. Polyacrylic acid (PAA) was used as template for the oppositely charged DOAB. The distribution of DOAB in the inverse miniemulsion and the solution viscosity behaviors of PDA were investigated. The results showed that the complexes of DOAB and PAA were located not only at the interface of the inverse miniemulsion droplets and oil phase but also in the interior of inverse miniemulsion droplets. PDA prepared with template exhibited remarkable enhancement of solution viscosity (thickening ability). And the optimal thickening ability was obtained when the aqueous phase pH was 6.5 and the ratio of DOAB to PAA was 1. The thickening ability of PDA was improved with increasing DOAB content. PDA prepared with template showed stronger association ability than that prepared without template for its longer hydrophobic block structure, which was further supported by the plots of fluorescence spectra.

***Keywords:*** *polymer synthesis, molecular engineering, hydrophobically associating, inverse miniemulsion polymerisation, template*

## 1. Introduction

In recent years, water-soluble, hydrophobically associating polymers have attracted considerable interest for their special properties. Among these polymers, hydrophobically associating polyacrylamide (HAPAM) is especially attractive [1–9]. It is well known that there are intramolecular association and intermolecular association in HAPAM aqueous solution due to the presence of hydrophobic groups. When the concentration of HAPAM is above a certain concentration, intermolecular hydrophobic interaction will lead to the formation of dynamic three-dimensional network structure and supramolecular aggregates, which can dramatically enhance the viscosity (thickening ability) [10, 11]. These polymers have potential applications in many fields including enhanced oil recovery, drilling fluids, coatings, water treatment, etc. [12–18].

Up to now, micellar polymerization has been the most effective method for the synthesis of HAPAM. This method is extremely attractive since it allows the preparation of polymers with hydrophobic microblock structure [19, 20]. As a result, the polymers exhibit higher thickening abilities than those with random distribution structure at the similar molar mass. However, the major disadvantages for this method are obvious: the initial concentration of the reaction mixture is relatively low because of gel effect during the course of poly-

---

*Corresponding author, e-mail: glx802400@bit.edu.cn

merization, and the water solubility of the HAPAM is often poor [10, 21, 22], which makes difficult its practical application.

A variety of techniques have been suggested to overcome the problems mentioned above, such as inverse emulsion polymerization and inverse microemulsion polymerization, which can also be used to obtain HAPAM with higher solid content and better water solubility [23–25]. However, these methods require a large amount of surfactant, which restricts their potential applications. And only a small number of literatures on these techniques have been reported recently.

Inverse miniemulsion polymerization is another promising method that can be applied to obtain water-soluble polymer with low surfactant content. In our laboratory, an attempt has been made to prepare HAPAM via inverse miniemulsion polymerization using cationic hydrophobic monomer. In order to obtain HAPAM with higher thickening ability, we introduce template polymerization method [26–28] to the inverse miniemulsion system. In the presence of template, the oppositely charged monomer can form a longer hydrophobic block along the polymer chains. The products will exhibit higher thickening ability.

In this work, we examined the inverse miniemulsion polymerization of acrylamide with the cationic hydrophobic monomer Dimethyloctane(2-acrylamidopropyl)ammoniumbromide (DOAB) in the presence of template polyacrylic acid (PAA). The distribution of DOAB in the inverse miniemulsion and the solution viscosity behaviors of polymers prepared by varying aqueous phase pH, ratio of hydrophobic monomer to template and hydrophobic monomer content were investigated. Effects of polymer concentration and inorganic salt (NaCl) concentration on hydrophobic associating behavior were examined.

## 2. Experimental section

### 2.1. Materials

N,N'-Dimethyl-1,3-propanediamine (98%) and 1-Bromooctane were purchased from Huaian Heyuan Chemical Factory (Huaian, China) and Shanghai Chemical Reagent (Shanghai, China) respectively. Acrylamide (AM), Acryloyl chloride and Sorbitan monooleate (Span80) were obtained from Sinopharm Chemical Reagent Co., Ltd, (Beijing, China). PAA ($M_n$ = 1200 g/mol) and Amphiphilic polymer of poly(oxyethylene-oxypropylene-oxyethylene-oxypropylene)-vinyl diamine (CM38, $M_w$ = 3800 g/mol) were supplied by Institute of Chemistry, the Chinese Academy of Sciences, (Beijing, China); 2,2′-azobis[2-(2-imidazolin-2-yl)-propane]dihydrochloride (VA-044) was purchased from Fluka (Milwaukee, USA). Deionized water was used throughout the work. All reagents and other solvents were used as received.

### 2.2. Measurements

FTIR spectrum of the hydrophobic monomer was recorded on a Prestige-21 FTIR spectrophotometer (Shimadzu Corporation, Kyoto, Japan) with KBr pellet in the range of 400–4000 cm$^{-1}$.

$^1$H NMR spectrum was measured with a Mercury-plus 400 (Varian Inc., Palo Alto, USA) using Chloroform-D ($CDCl_3$) as the solvent.

Elemental analysis was carried out using an elemental analyses system, Vario EL III (Elementar Analysensysteme GmbH, Hanau, Germany).

The molar mass of polymer was characterized relatively with intrinsic viscosity, and the intrinsic viscosity of polymer was determined using an Ubbelohde viscometer with 1.0 mol/l NaCl as solvent and the concentrations of the polymer were in the range of 0.02–0.05 g/dl. The measurement process was kept at 30.0 ± 0.1°C. The intrinsic viscosity [η] of polymer was obtained with the dilution extrapolation method. The intrinsic viscosity measurement was an approximation method due to the effect of intramolecular hydrophobic interaction on the determination of the viscosity-average molar mass for polymer [29]. The molar mass of polymer was determined by the Mark-Houwink-Sakurada Equation (1):

$$[\eta] = KM_{\eta}^{\alpha} \tag{1}$$

where $K = 4.75 \cdot 10^{-3}$ ml/g and $\alpha = 0.80$.

Droplet size of the inverse miniemulsion was determined at 25°C by a Malvern Zetasizer 3000HS (Malvern Instruments Ltd, Worcestershire, U.K.).

Apparent viscosity measurement was conducted by a Brookfield LVDV II+ rotational viscometer (Brookfield Asset Management Inc., Middleboro, USA) with a spindle 1 and a shear rate of 6 rpm at 80°C.

The fluorescence emission spectrum of the probe pyrene was recorded on a HITACHI F-4500 (Hitachi, Ltd., Tokyo, Japan) fluorescence spectrophotometer at 30°C with an excitation wavelength of 335 nm and a slit width of 2.5 nm in a scanning range of 350–450 nm. The ratio of the first band intensity to the third band intensity of pyrene emission, $I_1/I_3$, was used as an estimate of micro polarity of pyrene microenvironment. A required volume of stock solution of pyrene in methanol ($1\cdot10^{-3}$ mol/l) was pipetted out into a standard flask and a thin film of pyrene was deposited on the side of the flask after the evaporation of solvent by bubbling nitrogen. The concentration of pyrene was maintained at $1\cdot10^{-6}$ mol/l in all the solutions and the concentrations of polymers were in the range of 0.1–0.55 g/dl.

All the polymer solutions were prepared by dissolution of the samples in deionized water at room temperature. Afterward, the solution was diluted and polymer aqueous solutions with different concentrations were prepared and kept for 24 h before measurement.

## 2.3. Synthesis of cationic hydrophobic monomer DOAB

### 2.3.1. Synthesis of N,N′-dimethylpropylacrylamide

N,N′-dimethylpropylacrylamide was synthesized according to the literature [22]. Dichloromethane solution (20 ml) with predissolved N,N′-dimethyl-1,3-propanediamine (4.17 g, 0.04 mol) and sodium hydroxide solution (7 ml, 6 mol/l) were added to a round bottom flask, cooled by ice-water bath and purged with nitrogen for 30 min at the same time. Then dichloromethane solution (20 ml) with predissolved acryloyl chloride (3.71 g, 0.041 mol) was titrated slowly. The temperature was kept below 5°C. After titration, the system was kept still for 5 h at the room temperature. Then the organic phase was washed twice with saturated sodium carbonate aqueous solution and aqueous phase was extracted with dichloromethane after adding excessive sodium chloride. The organic phase and the extract liquid of dichloromethane were dried for 24 h with magnesium sulfate, solvents were removed by vacuum distillation, and liquid product was obtained (yield 74%).

### 2.3.2. Synthesis of DOAB

DOAB was prepared via quaternization reaction [22, 30] of N,N′-dimethylpropylacrylamide and 1-Bromooctane according to the following method: In a round-bottom flask with a magnetic bar, acetone (60 ml) with predissolved N,N′-dimethylpropylacrylamide (4.5 g, 0.029 mol) and 1-Bromooctane (6.4 g, 0.033 mol) was added under the purge of nitrogen. The reaction proceeded at 55°C for 24 h before being quenched. The initial product was precipitated and purified by the mixture solvent of absolute ether and acetone. Solvents were removed by vacuum distillation and the rude product was dried to a constant weight in a vacuum oven at room temperature, then power DOAB was obtained (yield 81%). FTIR (KBr, $cm^{-1}$): $v = 3434$ (N–H stretching), 3041 (C=CH stretching), 1670 (C=O stretching), 1626 (C=C stretching), 1410 (C–N stretching), 726 ($(CH_2)_n$, n>>2, rocking). $^1H$ NMR ($CDCl_3$, ppm): δH = 8.3 (1H, s), 6.5 (1H, s), 6.3 (1H, m), 5.6 (1H, s), 3.9 (2H, d), 3.5 (2H, s), 3.3 (2H, s), 3.2 (6H, s), 2.1 (2H, s) ,1.8 (2H, s), 1.3 (10H, m) , 0.9 (3H, s). Elemental analysis: Calculated for $C_{16}H_{33}N_2O$ (269.45 g/mol): 71.32 (C%), 12.34 (H%), 10.40 (N%). Found: 71.30 (C%), 12.76 (H%), 10.32 (N%).

## 2.4. Synthesis of cationic hydrophobically associating polyacrylamide (PDA)

PDA was synthesized as described below. Aqueous phase consisting of a certain amount of template PAA, monomers DOAB, AM solution (15 g, 50 g/dl), initiator VA-044 (6 mg) was prepared and adjusted to pH 6.5 with sodium hydroxide solution (Unless otherwise defined, pH used herein was about 6.5). Then aqueous phase was mixed with oil phase prepared by predissolving surfactant Span80 (1.5 g) and stabilizer CM38 (0.15 g) in kerosene (35 g). The mixture was pre-emulsified by magnetic stirring and purged with nitrogen for 1 h. Then the mixture was homogenized by ultrasonication for 180 s with a Branson sonifier W450 Digital (Branson Ultrasonics Corporation, Danbury, USA) at 70% amplitude in an ice-water bath to prevent polymerization. The inverse miniemulsion thus prepared was subsequently transferred into a round bottom flask, and purged with nitrogen for 15 min. Then the reaction proceeded at 50°C for 4 h. The

**Table 1.** Correlative data of the polymers prepared via inverse miniemulsion polymerization

| Sample | DOAB [mol%][a] | DOAB/PAA [mol/mol] | $M_\eta \cdot 10^{-6}$ [g/mol] |
|---|---|---|---|
| PAM | – | – | 5.06 |
| PDA-1 | 0.5 | – | 5.13 |
| PDA-2 | 0.1 | 1.0 | 4.93 |
| PDA-3 | 0.3 | 1.0 | 4.75 |
| PDA-4 | 0.5 | 1.0 | 4.38 |
| PDA-5 | 0.5 | 0.5 | 4.11 |
| PDA-6 | 0.5 | 2.0 | 4.67 |

[a]The molar ratio of DOAB to AM

initial product was dropped into the mixture solvent of ethanol and acetone and then washed with absolute ethanol for three times. After filtration, the rude product was dried to a constant weight in a vacuum oven at room temperature, and then power polymer was obtained. The correlative data about the polymer samples were presented in Table 1.

## 3. Results and discussion

### 3.1. Molecular design for PDA

The synthetic route for PDA is shown in Figure 1. We firstly synthesized cationic monomer DOAB. PDA with hydrophobic block was then obtained by the inverse miniemulsion polymerization with PAA as template.

In the inverse miniemulsion system with template PAA, cationic hydrophobic monomer DOAB was soluble in aqueous phase, namely the inverse miniemulsion droplets. DOAB strongly interacted with template PAA due to electrostatic interaction and formed a tight complex. This complex could be completely dissolved in aqueous solution, even when pH varied from 5 to 8. It could be assumed that the polymerization of DOAB adsorbed on template followed a zip mechanism rather than a pick-up mechanism for the strong ionic interaction. Under the same conditions, the neutral monomer AM had no interaction with PAA. When DOAB adsorbed on template PAA was initiated by a growing macroradical headgroup in the aqueous phase, polymerization would proceed along the PAA chain to form a hydrophobic block and then initiated AM in the aqueous phase to form a hydrophilic block. These steps were repeated many times, so the structure of the product was multiblock [31]. The length and density of the hydrophobic block in the HAPAM chain depended on the pH of the aqueous phase and the ratio of hydrophobic monomer to template. Under proper conditions, products with high hydrophobically associating ability could be obtained through the template process. The polymerization process was illustrated in Figure 2.

Unfortunately, it was impossible to separate PDA from template PAA completely [32], and the exact sequence distribution of hydrophobic groups along the polymer chain could not be detected by $^1$H NMR and FTIR since the length of the hydrophobic blocks was too large [23] and the amount of hydrophobic groups was too small [31]. So we compared the PAA-PDA complexes obtained by inverse miniemulsion polymerization with the complexes obtained by mixing of equimolar solutions of the two polymers at the following experi-

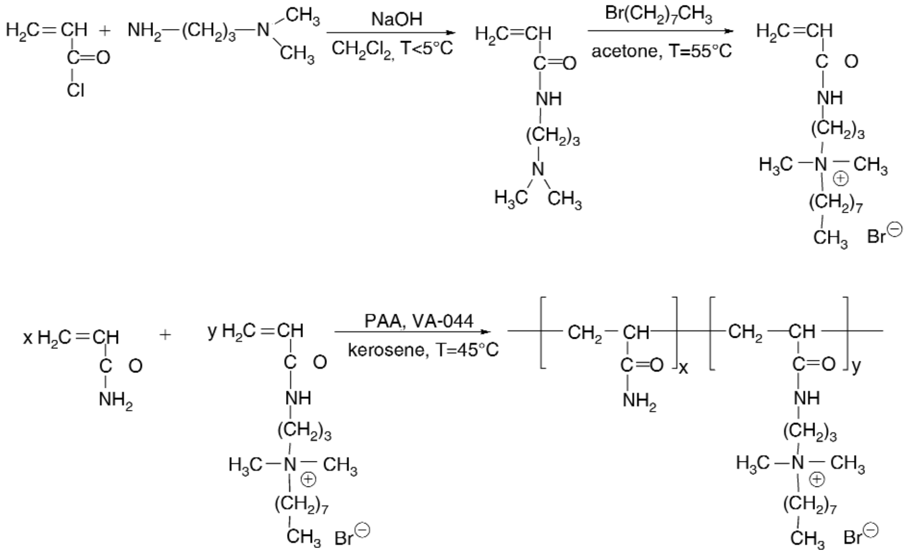

**Figure 1.** Synthetic route for PDA

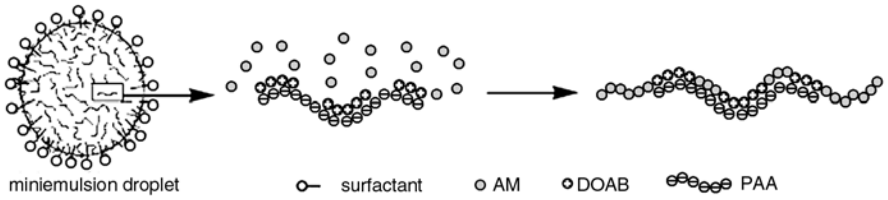

**Figure 2.** Representation of inverse miniemulsion polymerization in the presence of template

ments and studied the sequence distribution indirectly by the hydrophobic associating behavior of the polymers.

### 3.2. Distribution of DOAB in the inverse miniemulsion

The distribution of DOAB in the inverse miniemulsion can be reflected by the variation of inverse miniemulsion droplet size. Figure 3 shows the droplet sizes of the inverse miniemulsions prepared with (DOAB/PAA ratio was 1) and without template PAA. It can be noted that the initial droplet size of the inverse miniemulsion prepared without template decreased with the increase of DOAB content. And in the presence of template, the initial droplet size decreased firstly and then kept nearly constant. These results indicated that DOAB was located at the interface of the inverse miniemulsion droplet and oil phase for its surface activity, while the complexes of DOAB and PAA were located not only at the droplets interface but also in the interior of inverse miniemulsion droplet. Indeed, if the complexes were located at the interface, the interfacial tension and therefore the droplets size would be modified [23].

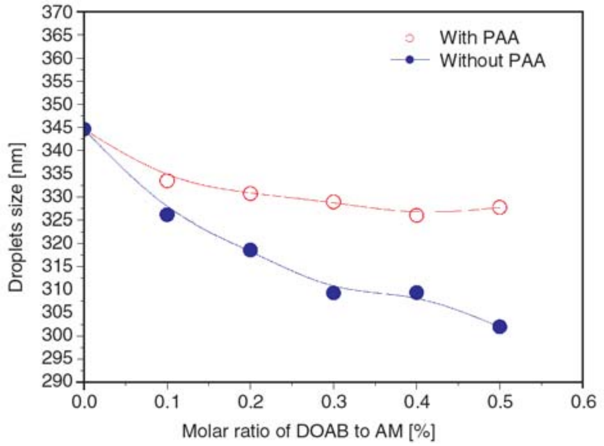

**Figure 3.** Effect of PAA on the droplets size of the inverse miniemulsion

### 3.3. Influencing factors of the inverse miniemulsion polymerization in the presence of template

#### 3.3.1. Aqueous phase pH

Figure 4 shows the effect of aqueous phase pH on the molar mass and apparent viscosity of PDA solution (0.5 g/dl). The content of DOAB was 0.5 mol% (relative to AM) and the DOAB/PAA ratio was 1. The molar mass and apparent viscosity of PDA solution firstly increased and then decreased with increasing aqueous phase pH. The largest molar mass was obtained at pH 7.0, but the optimal thickening ability was obtained at pH 6.5. At the same hydrophobic group content, PDA prepared at pH 6.5 must have a longer hydrophobic block structure than that of prepared at pH 7.0. In the inverse miniemulsion system, aqueous phase pH determined the ionization degrees of DOAB and PAA, which significantly influenced their interaction. Under strong acid or strong basic conditions, the interaction between DOAB and PAA was weakened due to the fact that one of their ionization degrees was decreased. This led to a decreasing quantity of DOAB preadsorbed on PAA and the number of hydrophobic groups randomly distributed in the PDA chain increased, and therefore the thickening ability of PDA decreased.

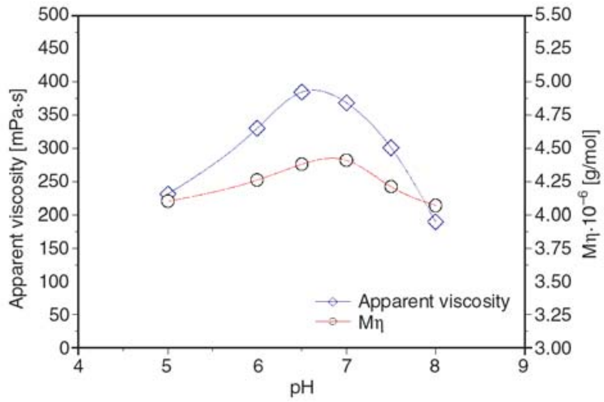

**Figure 4.** Effect of aqueous phase pH on the molar mass and apparent viscosity of PDA solution

### 3.3.2. Ratio of hydrophobic monomer to template

Figure 5 shows the effect of the molar ratio of DOAB to PAA on PDA solution viscosity as a function of polymer concentration. When the molar ratio of DOAB to PAA was equal to 1, the thickening ability was the best. In this case, most DOAB molecules were preadsorbed on PAA chains. When the ratio was higher than 1, part of DOAB molecules were dissolved in the aqueous phase for the absence of template, which led to a decrease of the number of hydrophobic blocks along the macromolecular chains and the thickening ability. When the ratio was lower than 1, most DOAB molecules were preadsorbed on the PAA chains, but the length and density of the hydrophobic blocks decreased, so the thickening ability decreased.

It was apparent that the viscosities enhanced sharply when PDA solution concentrations attained approximately 0.30 g/dl. This suggested that 0.30 g/dl (or a value around 0.30 g/dl) was a critical concentration for the three polymers, at which intramolecular association transformed into intermolecular association, i.e., the critical association concentration ($C^*$). When the polymer concentrations increased further, intermolecular association was strengthened because of the shortening of the distance between macromolecules, and the viscosity enhanced rapidly.

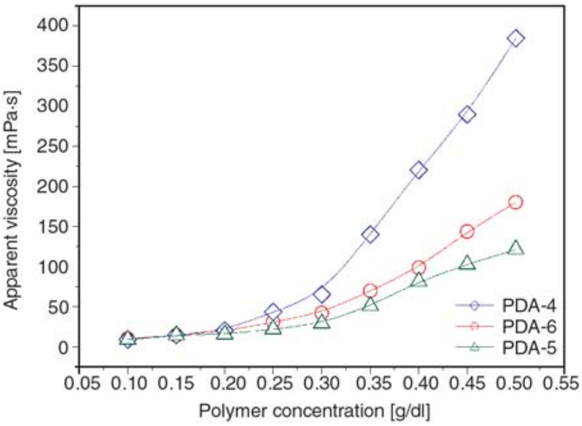

**Figure 5.** Effect of DOAB to PAA ratio on the apparent viscosity of PDA solution

### 3.3.3. Hydrophobic monomer content

Figure 6 shows the effect of hydrophobic monomer content on the viscosity of PDA solution. It was found that the apparent viscosity increased and the $C^*$ decreased with the increase of hydrophobic monomer content. The $C^*$ were about 0.30 and 0.34 g/dl for PDA-4 and PDA-2 respectively. The solution viscosity of PDA prepared with higher content of DOAB increased rapidly at the concentration above $C^*$. This could be explained by the higher hydrophobic block density along the PDA chain, which led to a larger quantity and probability of hydrophobic groups that participated in association.

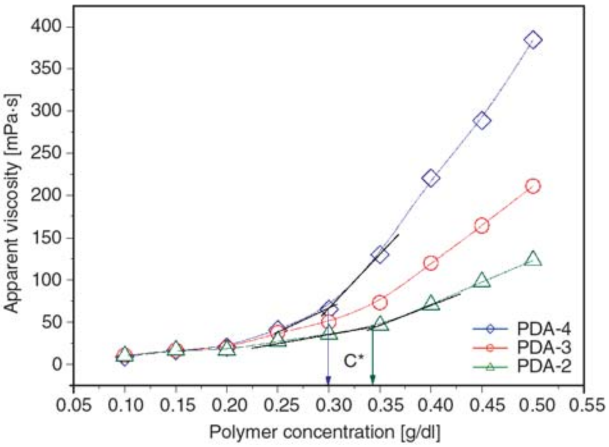

**Figure 6.** Effect of hydrophobic monomer content on the apparent viscosity of PDA solution

One can also noted that the molar mass of PDA prepared with template decreased with increasing hydrophobic monomer content (Table 1). This could be mainly attributed to the presence of PAA, which was known to act as a chain-transfer agent. This assumption was supported by the comparison with PDA-1. The fact of PDA with lower molar mass and higher thickening ability due to the template effect was described in the next section.

### 3.4. Apparent viscosity of different polymer solutions

The relationships between apparent viscosity and polymer concentration for different polymers can be seen in Figure 7. A strong template effect was evidenced by the different trends of the curves. The solution viscosity of PDA prepared with template showed a significant dependence of the viscosity on concentration. The viscosity of PDA-4 solution was higher than that of PDA-1 solution at the concentration above $C^*$ (0.30 g/dl), opposite tend was showed at the concentration below $C^*$. This result indicated that PDA prepared with template exhibited a longer hydrophobic block characteristic,

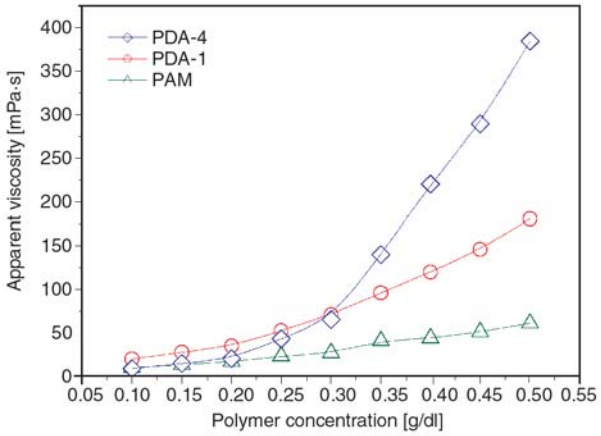

**Figure 7.** Relationships between apparent viscosity and polymer concentration for different polymers

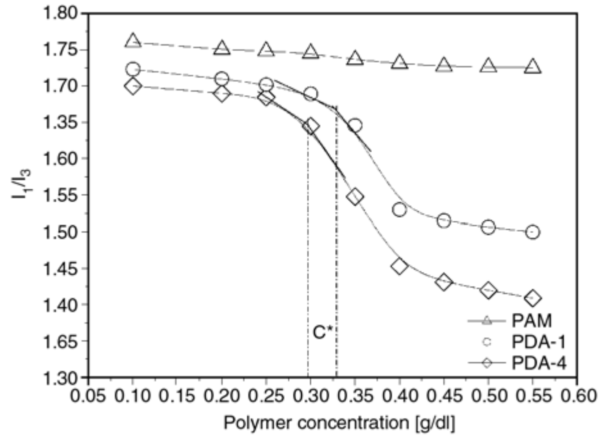

**Figure 8.** Variation of the $I_1/I_3$ value with polymer concentration

which made it more easily to form intermolecular association at the concentration above C* and intramolecular association at the concentration below C* [8, 33, 34].

It was interesting to note that the viscosity of PDA was higher than that of PAM without hydrophobically modified at the concentration below C*. The unusual phenomenon disagreed with the behavior generally described for HAPAM. Viscosity of HAPAM was often found to be either equal to or lower than that of PAM [16] at the concentration below C* due to the formation of intramolecular hydrophobic association. The explanation of this discrepancy could be related to the presence of template PAA. In the polymer solution, PAA was absorbed on the hydrophobic chain of PDA through electrostatic interaction and formed the PAA-PDA complexes, which enhanced the viscosity of the polymer solution.

The apparent viscosity reflects the hydrophobic association ability from a macroscopic property, whereas the fluorescence probe experiments can investigate their hydrophobic association ability from the molecular level. It is known that the value of $I_1/I_3$ is extremely sensitive to the polarity of the probe microenvironment. The weaker the polarity of the microenvironment around the pyrene molecule, the lower the value of $I_1/I_3$.

Figure 8 shows the value of $I_1/I_3$ as a function of polymer concentration in aqueous solution. For PAM, the value of $I_1/I_3$ had no remarkable changes in whole concentration region, but for PDA, the value of $I_1/I_3$ decreased with increasing polymer concentration. Especially in the range of higher concentrations, the $I_1/I_3$ value of PDA was much lower than that of PAM. This indicated that the hydrophobic microdomains have formed in polymer solution due to the intramolecular associating at lower concentrations and intermolecular associating at higher concentrations. It could be found that the $I_1/I_3$ values of PDA-4 and PDA-1 decreased abruptly at a concentration of about 0.30 and 0.33 g/dl (C*) respectively. At the same concentration, the $I_1/I_3$ value of PDA-4 was lower than that of PDA-1, especially at the concentration above C*. This difference should be attributed to the different microstructures of polymers. As mentioned above, polymer with longer hydrophobic block structure had stronger hydrophobic association ability. Therefore the polarity of the hydrophobic microdomains for PDA-4 was weaker, resulting in the lower value of $I_1/I_3$.

### 3.5. Effect of inorganic salt concentration on apparent viscosity of polymers solution

Figure 9 shows the effect of inorganic salt (NaCl) concentration on the apparent viscosity of polymer solution (0.5 g/dl). It was found that NaCl has a significant effect on the values of apparent viscosity. The expected viscosity decrease was observed for PAM solution, which generally attributed to the thinning of hydration film around the macromolecular chain and the size shrinkage of the macromolecular by the increasing polarity of solvent. At the concentration above 1.0 g/l, the viscosity of PAM solution became insensitive to the increasing NaCl concentration due to the slightly change of the shrunken macromolecular chain size.

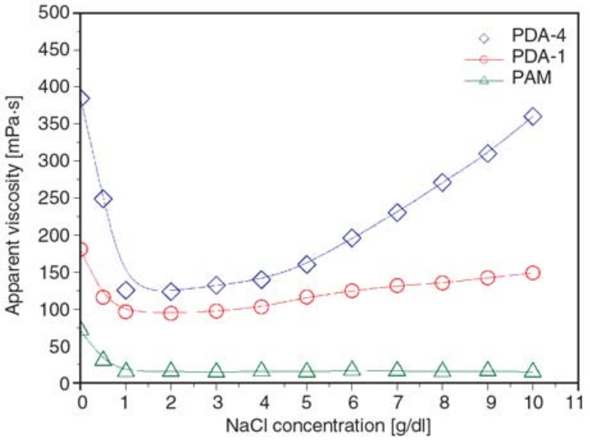

**Figure 9.** Effect of salt concentration on the apparent viscosity of polymer solution

As far as PDA was concerned, the viscosity decreased sharply with the addition of NaCl. It was believed that the added ionic charges acted as electrostatic shields had destroyed the PAA-PDA complexes, leading to a reduction in the macromolecular chain size and the decrease of solution viscosity, which was accelerated by the thinning of hydration film. With the increase of NaCl concentration, the viscosity of PDA solution increased. The addition of salt increased the polarity of solvent, which made the nopolar hydrophobic groups more easily to contract, resulting in the enhancement of intermolecular association and the solution viscosity. PDA prepared with template had a more significant salt thickening effect for its longer hydrophobic block structure.

## 4. Conclusions

A new approach was carried out to synthesize HAPAM via inverse miniemulsion polymerization in the presence of template. DOAB was synthesized via quaternization reaction and used as the hydrophobic monomer. PAA was used as template for the oppositely charged DOAB. In the inverse miniemulsion system, DOAB strongly interacted with template PAA and formed tight complexes. The complexes were located not only at the interface of the inverse miniemulsion droplets and oil phase but also in the interior of inverse miniemulsion droplets. The results from viscosimetry indicated that PDA prepared with template exhibited remarkable thickening ability in aqueous solution and aqueous salt solution. The thickening ability strongly depended on the chain structure, which was dominated by aqueous phase pH, ratio of hydrophobic monomer to template and hydrophobic monomer content. Furthermore, fluorescence spectra of pyrene probe revealed that PDA prepared with template showed stronger association ability for its longer hydrophobic block structure.

## References

[1] Lee K. E., Poh B. T., Morad N., Teng T. T.: Synthesis and characterization of hydrophobically modified cationic polyacrylamide with low concentration of cationic monomer. Journal of Macromolecular Science Part A: Pure and Applied Chemistry, **46**, 240–249 (2009).
DOI: 10.1080/10601320802637284

[2] Yang Q. B., Song C. L., Chen Q., Zhang P. P., Wang P. X.: Synthesis and aqueous solution properties of hydrophobically modified anionic acrylamide copolymers. Journal of Polymer Science Part B: Polymer Physics, **46**, 2465–2474 (2008).
DOI: 10.1002/polb.21577

[3] Lu H. S., Feng Y. J., Huang Z. Y.: Association and effective hydrodynamic thickness of hydrophobically associating polyacrylamide through porous media. Journal of Applied Polymer Science, **110**, 1837–1843 (2008).
DOI: 10.1002/app.28596

[4] Gouveia L. M., Paillet S., Khoukh A., Grassl B., Müller A. J.: The effect of the ionic strength on the rheological behavior of hydrophobically modified polyacrylamide aqueous solutions mixed with sodium dodecyl sulfate (SDS) or cetyltrimethylammonium *p*-toluenesulfonate (CTAT). Colloids and Surfaces A: Physicochemical and Engineering Aspects, **322**, 211–218 (2008).
DOI: 10.1016/j.colsurfa.2008.03.008

[5] Lee K. E., Poh B. T., Morad N., Teng T. T.: Synthesis and characterization of hydrophobically modified cationic acrylamide copolymer. International Journal of Polymer Analysis and Characterization, **13**, 95–107 (2008).
DOI: 10.1080/10236660801905684

[6] Gao B. J., Guo H. P., Wang J., Zhang Y.: Preparation of hydrophobic association polyacrylamide in a new micellar copolymerization system and its hydrophobically associative property. Macromolecules, **41**, 2890–2897 (2008).
DOI: 10.1021/ma701967b

[7] Castelletto V., Hamley I. W., Xue W., Sommer C., Pedersen J. S., Olmsted P. D.: Rheological and structural characterization of hydrophobically modified polyacrylamide solutions in the semidilute regime. Macromolecules, **37**, 1492–1501 (2004).
DOI: 10.1021/ma035039d

[8] Xue W., Hamley I. W., Castelletto V., Olmsted P. D.: Synthesis and characterization of hydrophobically modified polyacrylamides and some observations on rheological properties. European Polymer Journal, **40**, 47–56 (2004).
DOI: 10.1016/j.eurpolymj.2003.09.014

[9] Ren H. J., Chen W. N., Zheng Y. F., Luan Z. K.: Effect of hydrophobic group on flocculation properties and dewatering efficiency of cationic acrylamide copolymers. Reactive and Functional Polymers, **67**, 601–608 (2007).
DOI: 10.1016/j.reactfunctpolym.2007.03.008

[10] Feng Y. J., Billon L., Grassl B., Khoukh A., François J.: Hydrophobically associating polyacrylamides and their partially hydrolyzed derivatives prepared by post-modification. 1. Synthesis and characterization. Polymer, **43**, 2055–2064 (2002).
DOI: 10.1016/S0032-3861(01)00774-1

[11] Volpert E., Selb J., Candau F.: Associating behaviour of polyacrylamides hydrophobically modified with dihexylacrylamide. Polymer, **39**, 1025–1033 (1998).
DOI: 10.1016/S0032-3861(97)00393-5

[12] Zhong C. R., Luo P. Y., Ye Z. B., Chen H.: Characterization and solution properties of a novel water-soluble terpolymer for enhanced oil recovery. Polymer Bulletin, **62**, 79–89 (2009).
DOI: 10.1007/s00289-008-1007-6

[13] Chagas B. S., Machado D. L. P. Jr., Haag R. B., De Souza C. R., Lucas E. F.: Evaluation of hydrophobically associated polyacrylamide-containing aqueous fluids and their potential use in petroleum recovery. Journal of Applied Polymer Science, **91**, 3686–3692 (2004).
DOI: 10.1002/app.13628

[14] Ma Z., Lundberg D. J., Roberts S., Glass E. J.: Phase behaviors and film properties of dispersions and coatings containing associative and conventional thickeners. Journal of Applied Polymer Science, **49**, 1509–1527 (2003).
DOI: 10.1002/app.1993.070490902

[15] Yekta A., Duhamel J., Brochard P., Adiwidjaja H., Winnik M.: A fluorescent probe study of micelle-like cluster formation in aqueous solutions of hydrophobically modified poly(ethylene oxide). Macromolecules, **26**, 1829–1836 (1993).
DOI: 10.1021/ma00060a006

[16] Hill A., Candau F., Selb J.: Properties of hydrophobically associating polyacrylamides: Influence of the method of synthesis. Macromolecules, **26**, 4521–4532 (1993).
DOI: 10.1021/ma00069a017

[17] Pamies R., Cifre J. G. H., de la Torre J. G.: Brownian dynamics simulation of polyelectrolyte dilute solutions under shear flow. Journal of Polymer Science Part B: Polymer Physics, **45**, 1–9 (2007).
DOI: 10.1002/polb.20994

[18] Shashkina Y. A., Zaroslov Y. D., Smirnov V. A., Philippova O. E., Khokhlov A. R., Pryakhina T. A., Churochkina N. A.: Hydrophobic aggregation in aqueous solutions of hydrophobically modified polyacrylamide in the vicinity of overlap concentration. Polymer, **44**, 2289–2293 (2003).
DOI: 10.1016/S0032-3861(03)00043-0

[19] Candau F., Selb J.: Hydrophobically-modified polyacrylamides prepared by micellar polymerization. Advances in Colloid and Interface Science, **79**, 149–172 (1999).
DOI: 10.1016/S0001-8686(98)00077-3

[20] McCormick C. L., Nonaka T., Johnson C. B.: Water-soluble polymers: 27. Synthesis and aqueous solution behaviour of associative acrylamide/*N*-acrilamide polymers. Polymer, **29**, 731–739 (1988).
DOI: 10.1016/0032-3861(88)90092-4

[21] Huang Z. Y., Lu H. S., He Y.: Amphoteric hydrophobic associative polymer: I synthesis, solution properties and effect on solution properties of surfactant. Colloid and Polymer Science, **285**, 365–370 (2006).
DOI: 10.1007/s00396-006-1570-z

[22] Chang Y. H., McCormick C. L.: Water-soluble copolymers. 49. Effect of the distribution of the hydrophobic cationic monomer dimethyldodecyl(2-acrylamidoethyl) ammonium bromide on the solution behavior of associating acrylamide copolymers. Macromolecules, **26**, 6121–6126 (1993).
DOI: 10.1021/ma00074a038

[23] Pabon M., Corpart J. M., Selb J., Candau F.: Synthesis in inverse emulsion and associating behavior of hydrophobically modified polyacrylamides. Journal of Applied Polymer Science, **91**, 916–924 (2004).
DOI: 10.1002/app.13227

[24] Lu H. S., Huang Z. Y.: Solution and adsorption properties of hydrophobically associating polyacrylamide prepared in inverse microemulsion polymerization. Journal of Macromolecular Science Part A: Pure and Applied Chemistry, **46**, 412–418 (2009).
DOI: 10.1080/10601320902728736

[25] Lu H. S., Feng Y. J.: Study on associative polymerizable inverse microemulsion. Journal of Macromolecular Science Part A: Pure and Applied Chemistry, **45**, 372–380 (2008).
DOI: 10.1080/10601320801946298

[26] Polowiński S., Janowska G.: Thermal copolymerization of acrylonitrile with methacrylate units arranged in matrix. European Polymer Journal, **11**, 183–185 (1975).
DOI: 10.1016/0014-3057(75)90144-5

[27] Rainaldi I., Cristallini C., Ciardelli G., Giusti P.: Copolymerization of acrylic acid and 2-hydroxyethyl methacrylate onto poly(*N*-vinylpyrrolidone): Template influence on comonomer reactivity. Macromolecular Chemistry and Physics, **201**, 2424–2431 (2000).
DOI: 10.1002/1521-3935(20001101)201:17<2424::AID-MACP2424>3.0.CO;2-8

[28] Charalambopoulou A., Bokias G., Staikos G.: Template polymerisation of *N*-isopropylacrylamide with a cationic monomer: Influence of the template on the solution properties of the product. Polymer, **43**, 2637–2643 (2002).
DOI: 10.1016/S0032-3861(02)00065-4

[29] Gao B. J., Jiang L. D., Liu K. K.: Microstructure and association property of hydrophobically modified polyacrylamide of a new family. European Polymer Journal, **43**, 4530–4540 (2007).
DOI: 10.1016/j.eurpolymj.2007.03.049

[30] Peiffer D. G.: Hydrophobically associating polymers and their interactions with rod-like micelles. Polymer, **31**, 2353–2360 (1990).
DOI: 10.1016/0032-3861(90)90324-R

[31] Zhang Y. X., Wu F. P., Li M. Z., Wang E. J.: Novel approach to synthesizing hydrophobically associating polymer using template polymerization: The synthesis and behaviors of acrylamide and 4-(ω-propenoyloxyethoxy) benzoic acid polymer. The Journal of Physical Chemistry B, **109**, 22250–22255 (2005).
DOI: 10.1021/jp054315i

[32] Al-Alawi S., Saeed N. A.: Preparation and separation of complexes prepared by template polymerization. Macromolecules, **23**, 4474–4476 (1990).
DOI: 10.1021/ma00222a023

[33] Candau F., Selb J.: Hydrophobically-modified polyacrylamides prepared by micellar polymerization. Advances in Colloid and Interface Science, **79**, 149–172 (1999).
DOI: 10.1016/S0001-8686(98)00077-3

[34] Regalado E. J., Selb J., Candau F.: Viscoelastic behavior of semidilute solutions of multisticker polymer chains. Macromolecules, **32**, 8580–8588 (1999).
DOI: 10.1021/ma990999e

*eXPRESS Polymer Letters Vol.3, No.12 (2009) 788–796*
*Available online at www.expresspolymlett.com*
*DOI: 10.3144/expresspolymlett.2009.97*

# Novel halogen-free flame retardant thermoset from a hybrid hexakis (methoxymethyl) melamine/phosphorus-containing epoxy resin cured with phenol formaldehyde novolac

*Z. Z. Huang*[1], *X. H. Zhang*[2*], *G. R. Qi*[2]

[1]The Department of Chemistry, Zhejiang University, Hangzhou 310027, China
[2]Key Laboratory of Macromolecular Synthesis and Functionalization (Ministry of Education), Department of Polymer Science and Engineering, Zhejiang University, Hangzhou 310027, China

*Received 19 July 2009; accepted in revised form 12 September 2009*

**Abstract.** This paper describes the curing behaviours, thermal properties and flame-resistance of a novel halogen-free epoxy hybrid thermoset, prepared by the curing reaction of hexakis (methoxymethyl) melamine (HMMM), a phosphorous-containing epoxy resin (EPN-D) with 9, 10-dihydro-9-oxa-10-phosphaphenanthrene 10-oxide (DOPO) group and phenol formaldehyde novolac (n-PF). The resultant thermosets showed high glass-transition temperatures ($T_g$, 123–147°C) as determined by thermal mechanical analysis (TMA), excellent thermal stability with high 5 wt% decomposition temperatures ($T_{d,5\%} \geq 308$°C) and high char yields ($Y_c \geq 39.4$ wt%) from the thermogravimetric analysis (TGA). All the cured EPN-D/HMMM/n-PF hybrid resins achieved the UL 94 V-0 grade with high limited oxygen indices (LOI > 45.7). It is found that phosphorous and nitrogen elements in the cured EPN-D/HMMM/n-PF hybrid resins had a positive synergistic effect on the improvement of the flame retardancy.

***Keywords:*** *thermosetting resins, thermal properties, flame retardancy, epoxy*

## 1. Introduction

Epoxy resins are widely used as functional materials due to their superior thermo-mechanical properties and excellent processability. However, the flammability limits the usage of epoxy resins in the field of electrical/electronic substrates. Halogen is usually applied to improve the flame retardancy of the epoxy resins. Nevertheless, halogen-containing epoxy resins have a series of potential environmental issues during decomposition or incineration [1, 2]. Halogen-free flame-retardant epoxy resins [3–30] are being developed and are expected to reduce the release of toxic substances during fire. By covalent incorporation of nitrogen [11, 12, 15–24] and phosphorous [3, 4, 7–9, 13, 14, 22, 23, 26, 30] into the backbone of the epoxy resins, better flame retardancy can be achieved. Thereinto, it is a very effective way to improve the flame retardancy by introducing P and N elements together into the epoxy matrix. For example, the incorporation of a thermal-stable cyclic phosphinate, i.e.: 9, 10-dihydro-9-oxa-10-phosphaphenanthrene 10-oxide (DOPO) [3] in combination with an isocyanurate structure [15–18], or a triazine structure [11, 14, and 20] into an epoxy matrix led to excellent flame retardancy without losing heat resistance. In these P and N containing flame retardant systems, P is favourable to the formation of char structure while N is generally released as a non-flammable gas which can dilute air and absorb heat energy in combustion. However, complex synthesis of most

---

[*]Corresponding author, e-mail: xhzhang@zju.edu.cn

reported nitrogen-containing epoxy resins or hardeners [19, 21] is unfavourable to their application.

Hexakis (alkoxymethyl) melamine (HMMM) is widely used as flame retardant for polymeric materials because it has high nitrogen content and low cost. It has also been applied to blend with epoxy resin for preparing halogen-free flame-retardant epoxy thermoset [11, 12, 23]. However, it is better to avoid serious phase separation between the HMMM network and epoxy network for the epoxy/HMMM/hardener system during cure. It was reported that silane coupling agents could be used to increase the miscibility of the epoxy network and the HMMM network for the epoxy/HMMM/diamine system [11]. Very recently, an epoxy/phenol formaldehyde novolac resin (n-PF) curing system was developed for preparing nitrogen-containing epoxy hybrid thermoset without using silane coupling agents, on the basis of reaction of HMMM and n-PF. However, there is still one problem for this hybrid system when it was used as electrical/electronic substrates. That is, HMMM alone is not enough to improve the flame resistance. In the present work, a phosphorous-containing epoxy resin (EPN-D), which was synthesized via the addition reaction of DOPO and epoxy phenol formaldehyde novolac resin (EPN) [22], was blended with HMMM and used for preparing a halogen-free flame-retardant epoxy resin. The curing behaviours, thermal properties and flame retardancy of the resultant thermosets were investigated in detail.

## 2. Materials and methods

Hexakis (methoxymethyl) melamine (HMMM, density: 1.2 g/ml, viscosity: 3000–6000 mPa·s (25°C), heat loss < 2 wt% at 105°C for 1.5 h, free formaldehyde: ≤ 0.5 wt%, degree of polymerization: 1.75) was obtained from Xinhua Chemical Co. (Hangzhou, China). Phenol formaldehyde novolac resin (n-PF, softening point: 85–95°C, free phenol ≤ 0.1 wt%,) was granted kindly from King-Board Chemical Co., Ltd. (Kunshan, China). Epoxy phenol formaldehyde novolac resin (EPN, functionality = 4–6) with EEW 182 g/eq was purchased from Shanghai Resin Company (Shanghai, China). 9, 10-dihydro-9-oxa-10-phosphaphenanthrene 10-oxide (DOPO) was supplied kindly by Hang Zhou JLS Flame Retardant Co., Ltd. (Hangzhou, China) and used as received. 4,4′-diaminodiphenylmethane (DDM) and 4,4′-diaminodiphenyl sulphone (DDS) were purchased from Sinopharm Chemical Reagent (Shanghai, China) and used without purification. Phosphorus-containing epoxy resin (EPN-D) was synthesized from the addition reaction of DOPO and EPN according to the reported method [22]. The structures of n-PF, HMMM and EPN-D are shown in Figure 1. *P*-toluenesulfonic acid (*p*-TSA) was purchased from Sinopharm Chemical Reagent Co., Ltd. (Shanghai, China) and used as a catalyst.

Differential scanning calorimeter (DSC) measurements were performed on a Perkins-Elmer DSC 7 thermal analyzer at a heating rate of 10°C/min under $N_2$. Gel Time Tester GT-2 was used to determinate the gel time of resins according to IPC-TM-650 method, which is an industrial method for evaluating the gel time of a resin. $T_g$ data of the thermosets were obtained from the measurement of DSC at a heating rate of 20°C/min under $N_2$ atmosphere. Thermogravimetric analyses (TGA) were carried out on a Perkins-Elmer Pyris 1 under an $N_2$

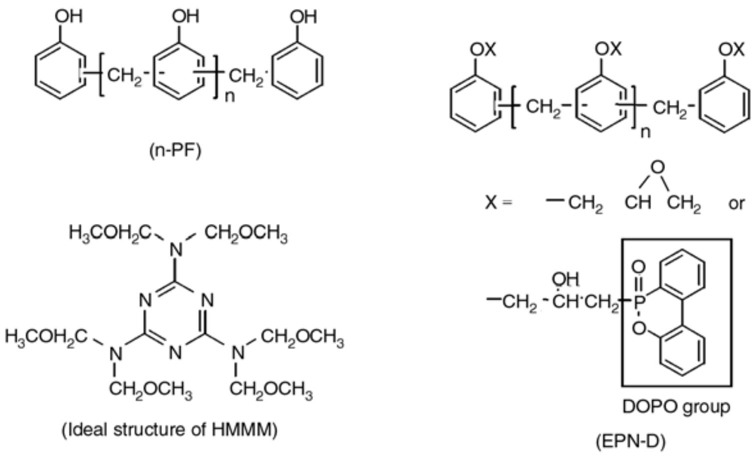

(n-PF)

(Ideal structure of HMMM)

(EPN-D)

**Figure 1.** Chemical structures of n-PF, EPN-D and HMMM

atmosphere at a heating rate of 10°C/min from 50 to 850°C. Limited oxygen indices (LOI) were measured on a HC-2 LOI tester according to ASTM D-2863-77. The percentage in the $O_2$-$N_2$ mixture deemed sufficient to sustain the flame was taken as the LOI. The UL-94 vertical test was performed according to the testing method proposed by Underwriter Laboratories Inc. with the test specimen bars of 130 mm in length, 13 mm in width and 1.6 mm in thickness. During the test, five sample bars suspended vertically over surgical cotton were ignited by a Bunsen burner. A flame was applied twice to the lower end of the bar for 10 s. The ratings of V-0, V-1 were achieved if burning stops within 10, 30 s after two applications of 10 s each of a flame to a test bar, and no flaming drips were allowed. The Z-axis coefficient of thermal expansion (Z-CTE) was measured with a DuPont 943 thermal mechanical analyzer (TMA) in accordance with ASTM E83-186. A specimen of 4 mm long, 4 mm in wide and 1.6 mm in thick was measured at a heating rate of 5°C/min. Normally the thermal expansion increases with increasing of the temperature and the CTEs are calculated from the slope. An abrupt change in slope of the expansion curve indicates a transition of the material from one state to another. $\alpha_1$ and $\alpha_2$ are the CTE values below and above $T_g$ respectively.

## 3. Preparation of the epoxy thermosets

The preparation of EPN-D/HMMM (10)/n-PF resin (i.e. with 10 wt% HMMM in the EPN-D/n-PF resin) is described next as an example. HMMM (12 g) and deionized water (1.2 g) were dissolved in butanone (50 ml), and the solution was stirred at room temperature. After the addition of *p*-TSA (0.12 g), the solution was stirred at 60°C for 1 h to yield homogeneous solution A. EPN-D (80 g) and of n-PF (28 g) were dissolved in 100 ml of butanone, and the solution was stirred at room temperature for 1 h to obtain homogeneous solution B. Solutions A and B were then poured together in a beaker and stirred at 60°C for another 1 h. A viscous, homogeneous solution was obtained, which was then poured onto a stainless plate and treated at 60°C *in vacuo* for complete removal of all volatiles. The obtained thermoset was transparent. All the epoxy thermosets were prepared with the curing procedure of 120°C (1 h), 160°C (2 h) and 190°C (2 h). For comparison, the sample preparation method was applied for EPN-D/HMMM/DDS (and DDM) curing system, DDS and DDM were mixed with EPN-D at an equivalent molar ratio of 1:1 respectively.

## 4. Results and discussion

### 4.1. Preparation and curing process of EPN-D/HMMM resin with various hardeners

It is known that novolac phenol formaldehyde resin (n-PF) is a hardener for preparing high-performance epoxy materials. It has strong reactivity towards HMMM and hydrated HMMM [23, 31]. It was reported that the usage of n-PF could avoid the phase separation between the HMMM network and epoxy network of the resultant materials [23]. Herein, aimed to prepare a new halogen-free epoxy material with excellent flame retardancy, n-PF was chosen and cured with HMMM and a phosphorous-containing epoxy resin (EPN-D, Figure 1) [22].

In the process for making such EPN-D/HMMM/n-PF hybrid resin (depicted in Figure 2), HMMM should be partly hydrated by quantitative water using *p*-TSA (~0.1 wt%) as a catalyst at first to generate a (hydroxymethyl) melamine [23]. This is a very important step for that (hydroxymethyl) melamine is more reactive than HMMM in the blend, and hydroxyl groups are favourable to condensation of HMMM [11]. The hydrated HMMM was then dissolved into solution B (here, DDS and DDM were used as hardeners for control experiments). After complete removal of all volatiles from the mixture, a transparent resin was obtained. It was disclosed that an epoxy/HMMM/hardener hybrid resin contained at least two reactions when heating them [11, 23]. One was the HMMM condensation with an endothermic process, and the other was the epoxy/hardener addition polymerization with an exothermal process. So the curing behaviours of EPN-D/HMMM/hardeners (n-PF, DDS and DDM) resins could be easily monitored by DSC method.

Figure 3 shows the DSC thermograms of the EPN-D/n-PF (DDS, DDM) resins and EPN-D/n-PF (DDS, DDM) resins with 20 wt% HMMM. One can see that the onset reaction temperature of the EPN-D/n-PF resin is ~150°C (line 3, Figure 3) and lower than that of the HMMM condensation in the

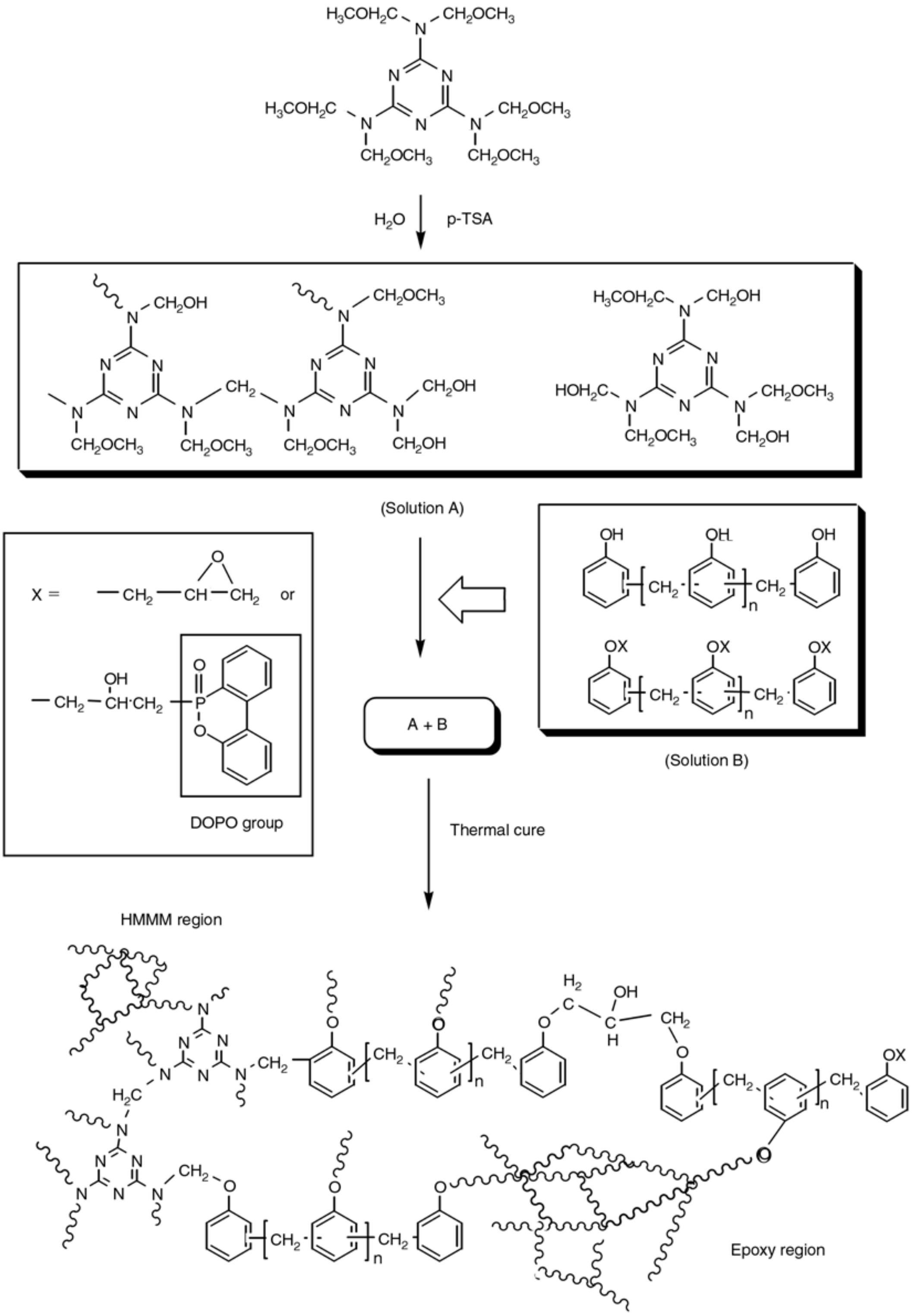

**Figure 2.** Scheme of the preparation and the curing process of the EPN-D/HMMM/n-PF hybrid resin

presence of *p*-TSA (~100°C [23]). That is, the HMMM condensation occurred before the curing reaction of EPN-D/n-PF. Moreover, the exothermal temperature at which the maximum conversion rate occurs in the DSC curve ($T_p$) of the EPN-D/HMMM/n-PF resin is 211.5°C and slightly higher than that of EPN-D/n-PF resin (201.4°C). This indicates that the curing reaction of EPN-D and n-PF was not seriously retarded by the HMMM network. Because n-PF could react with HMMM in the blend, a macromolecular hardener containing triazine and hydroxyl groups could be produced. The generated HMMM network linked n-PF could also act as a hardener for EPN-D. Thus, the direct

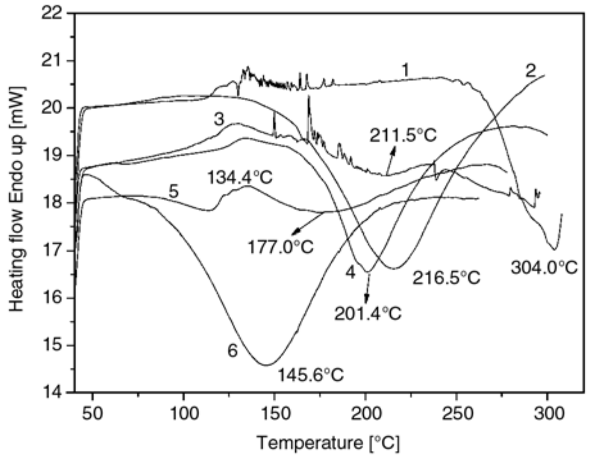

**Figure 3.** DSC thermograms of various epoxy samples at a heating rate of 10°C/min under $N_2$: 1. EPN-D/HMMM (20)/DDS, 2. EPN-D/DDS, 3. EPN-D/HMMM (20)/n-PF, 4. EPN-D/n-PF, 5. EPN-D/HMMM (20)/DDM, and 6. EPN-D/DDM

linkages between HMMM (and n-PF) region and EPN-D/n-PF region could be built with increasing the temperature (illustrated in Figure 2). This may strengthen the thermal properties of the resultant thermosets in comparison with the cured EPN-D/n-PF resin.

From curve 1 in Figure 3, it is seen that $T_p$ of the EPN-D/HMMM (20)/DDS resin is 304.0°C and dramatically higher than that of the EPN-D/DDS resin (216.5°C). This indicates that the curing reaction of EPN-D and DDS in the resin was really retarded seriously by the HMMM network formed before (irregular endothermic peaks in the range of 110–200°C in curve 1) due to relative low reactivity of DDS to EPN-D resin. This would result in incomplete cure of EPN-D/DDS. In practice, it was observed that the resultant thermosets showed serious phase separation even if silane coupling agents used in the EPN-D/HMMM/DDS curing system. For the EPN-D/HMMM/DDM resin (curve 5 in Figure 3), it is found that $T_p$ is 177.0°C and higher than that of EPN-D/DDM resin (145.6°C), and the endothermic peak is ~134.4°C and in the range of the exothermal peak of the EPN-D/DDM resin. Presumably, the epoxy network was firstly formed before the formation of HMMM network (curve 5 in Figure 3), and so some HMMM remained in the thermoset. This would result in the deterioration of the thermal properties of the resultant thermoset. Moreover, this hybrid resin had a very fast curing rate (the gel time was less 20 s at 160°C, determined according to IPC-TM-650 method) which is out of control in processing and is against practical application. However, the gel time of the EPN-D/HMMM (20)/n-PF resin was ~300 s at 160°C which is accepted in practice.

## 4.2. The glass transition temperatures ($T_g$s)

The glass transition temperatures ($T_g$s) for all the cured resins were obtained from DSC thermogram (see Figure 4) and TMA method. It is found that $T_g$ of the EPN-D/DDS thermoset (156°C, curve 2) is higher than that of the EPN-D/HMMM (20)/DDS thermoset (126°C, curve 1). It was also found that the second DSC heating curve of this thermoset showed a small exothermal peak beyond 200°C. So it is clear that the epoxy network in this hybrid resin is limited by the HMMM network formed in advance, which resulted in the dramatic decrease of $T_g$ of the resultant thermoset.

The $T_g$ of the EPN-D/HMMM (20)/n-PF thermoset is 122°C (curve 3 in Figure 4) and higher than that of the EPN-D/n-PF thermoset (111°C, curve 4). Due to the strong reactivity of n-PF to HMMM and EPN-D in the curing process, the epoxy network and HMMM network were gradually 'buttoned' together tightly. Part of the rigid triazine moieties, which are hindered in free rotation and vibration, were copolymerized with EPN-D and n-PF. This would lead to the inhibition of the chain motion of the EPN-D/n-PF network by the formation of HMMM network (and HMMM/n-PF network) and cause the increase of $T_g$. For this hybrid resin, more amounts of HMMM may increase the chances of

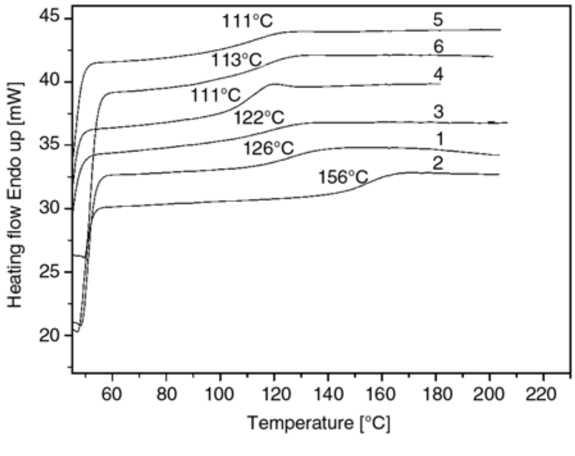

**Figure 4.** DSC curves of the cured samples: 1. EPN-D/HMMM (20)/DDS, 2. EPN-D/DDS, 3. EPN-D/HMMM (20)/n-PF, 4. EPN-D/n-PF, 5. EPN-D/HMMM (20)/DDM, and 6. EPN-D/DDM

condensation and thus decrease the residue of unreacted HMMM in the resultant thermoset. It is proved by the fact that $T_g$s of the EPN-D/HMMM/n-PF thermosets with 0, 10, 20 and 30 wt% HMMM was 120,123,136 and 147°C respectively, which were determined by TMA (Table 1). Although it is considered that the methoxymethyl group of HMMM can react with the amino group [32] of DDM, $T_g$ of the EPN-D/HMMM (20)/DDM thermoset is 111°C (curve 5, Figure 4) and is almost the same as that of the cured EPN-D/DDM resin (113°C, curve 6, Figure 4). It is clear that the incorporation of HMMM into EPN-D/DDM resin couldn't increase the $T_g$ of the resultant thermoset.

## 4.3. TGA evaluation

The thermal stability and thermal degradation patterns of the cured EPN-D/HMMM/n-PF resins with various HMMM content were evaluated by TGA. Figure 5 shows the TGA curves of these thermosets. The thermal parameters including 5 wt% decomposition temperature ($T_{d,5\%}$) and char yield ($Y_c$) of these thermosets are collected in Table 1. It is found that $T_{d,5\%}$ of the EPN-D/HMMM/n-PF thermoset increased from 308 to 351°C with increasing the content of HMMM from 10 to 30 wt%. Such $T_{d,5\%}$ values are satisfactory for using as electric materials, however, they are clearly lower than that of the EPN-D/n-PF thermoset (388°C). This may be attributed to the decomposition of the weak crosslink points between the triazine ring and some unreacted groups (e.g.: $–NCH_2OCH_3$, $–NCH_2OH$ and $–NCH_2OCH_2N–$ etc.) in the HMMM network. For this hybrid resin, the probability of producing the weak linkages and unreacted groups may be decreased with increasing the HMMM content because the chance of the condensation of HMMM and n-PF/HMMM would be increased with increasing HMMM content when relatively more HMMM is applied. The char residue of the thermosets changes from 39.4 to 44.7 wt% when the HMMM content increases from 10 to 30 wt%. It is considered that high crosslink density may be favourable to improving the char residue of the resultant thermosets, which was proved by TMA data in Table 1. The high char yields of these thermosets are favourable to form intumescent charred layers during fire and can block the spread of the fire, and thus ensure poor flammability. This will be proved by the following UL 94 vertical test results.

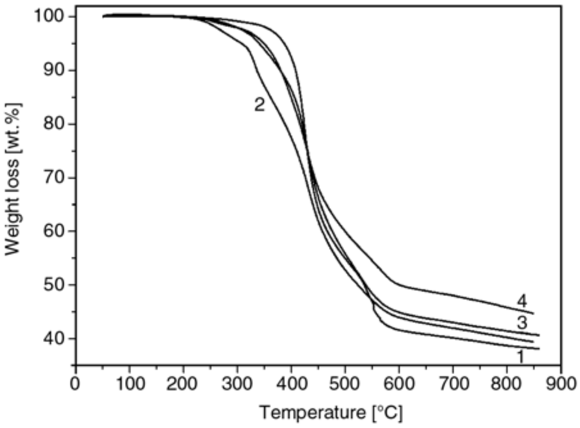

**Figure 5.** TGA curves of the EPN-D/HMMM/n-PF thermosets with: Line-1, 0 wt%; Line-2, 10 wt%; Line-3, 20 wt% and Line-4, 30 wt% HMMM (10°C/min, $N_2$)

## 4.4. Flame retardancy of the cured EPN-D/HMMM/n-PF resin

Limited oxygen index (LOI) presents the minimum oxygen concentration (in a flowing mixture of oxygen-nitrogen gas) required to support candle-like downward flame combustion [3]. A material with LOI of 26 or higher is rated as a flame-retardant material [33]. It is strongly dependent on the char residue for halogen-free polymers and is suitable as a semi-qualitative indicator of the effectiveness of

**Table 1.** Thermal properties, flame retardancy and CTEs of the EPN-D/HMMM/n-PF thermosets[a]

| HMMM content [wt%] | N [wt%] | P [wt%] | $T_g$ [°C] (TMA) | CTE ($\alpha_1/\alpha_2$) | $T_{d,5wt\%}$ [°C] | $Y_{c,wt\%}$ (850°C) | LOI | Burning time[b] | Classification |
|---|---|---|---|---|---|---|---|---|---|
| 0 | 0.00 | 2.50 | 120 | 51/280 | 388 | 38.2 | 40.8 | 11 | V-1 |
| 10 | 2.15 | 1.67 | 123 | 27/165 | 308 | 39.4 | 45.7 | 7 | V-0 |
| 20 | 4.30 | 1.48 | 136 | 34/163 | 340 | 40.7 | 48.9 | 6 | V-0 |
| 30 | 6.45 | 1.30 | 147 | 24/114 | 351 | 44.7 | 55.5 | 5 | V-0 |

[a] the curing procedure: 170°C/2 h in a heat press with a pressure of 10 MPa (without postcure procedure);
[b] the maximum burning time after 10 s ignition for each test bar, no drippings

the flame retardants in laboratory. While UL-94 vertical test is another testing method for flame-retardancy evaluation of materials in industrial application with strong heat input, and thus the results depend on the integrated effects of all flame-retardant elements the material contained.

The flammability of the thermosets was evaluated with their LOIs and by UL 94 test. Because of much higher concentration of phenol formaldehyde structures and high phosphorus content (2.5 wt%), which facilitated the formation of intumescent charred layers observed after ignition, LOI value of the EPN-D/n-PF thermoset is 40.8 and higher than that of the common epoxy thermoset (e.g.: LOI of the cured DGEBA/ethylenediamine resin is 19 [27]). The maximum burning time after 10 s ignition for the EPN-D/n-PF thermoset was 11 s and only achieved UL-94 V-1 grade. The main reason may be that the EPN-D/n-PF thermoset lacks non-flammable gas source in combustion to retard flame since it does not contain nitrogen element. The LOIs of the EPN-D/HMMM/n-PF thermosets containing 10, 20 and 30 wt% HMMM are 45.7, 48.9 and 55.5 respectively. The improvement of weight percentage of phosphorous and nitrogen elements in the thermoset with respect to the non-flammability of the epoxy thermoset is remarkable in comparison with the EPN-D/n-PF thermoset.

The UL-94 test results show that all EPN-D/HMMM/n-PF thermosets can achieve UL-94 V-0 grade without any drippings. The maximum burning time after 10 s ignition for the thermosets containing 10, 20 and 30 wt% HMMM content are 7, 6 and 5 s respectively (see Table 1). For these halogen-free resins, the function of phosphorous in the materials is favourable to the formation of char residue (a solid phase flame-retardancy mechanism), whereas nitrogen can mainly be released as a non-flammable gas which can dilute air and absorb heat energy in combustion (a vapour phase flame-retardancy mechanism). Herein, incorporating about 1.67 wt% of phosphorus and 2.15 wt% nitrogen element into the thermoset can make the thermoset flame-retardant in industrial applications, similarly to the XT/EPN-D/DICY system [22] reported by us earlier.

### 4.5. Z-axis Coefficient of thermal expansion (CTE)

The Z-axis coefficient of thermal expansion (CTE, $\alpha_1/\alpha_2$) of a polymer is a very important parameters for evaluating the long term stability and reliability of an electrical/electronic substrate. The lower the $\alpha_1/\alpha_2$ is, the better the dimensional stability of the thermoset is. It can be determined by TMA. The CTE values of the aforementioned EPN-D/HMMM/n-PF thermosets are shown in Table 1. The $\alpha_1/\alpha_2$ of the EPN-D/n-PF thermoset was 51/280 and bigger than that of all the EPN-D/HMMM/n-PF thermosets in which the $\alpha_1/\alpha_2$ values decreased with increasing the HMMM content of the thermoset. This may be the result of the increasing crosslinking density, which is proved by the fact that $T_g$s of the thermosets increased from 120 to 147°C with increasing HMMM content from 0 to 30 wt%. These rigid triazine moieties may decrease the free volume of the thermoset, and thus increase CTE values.

## 5. Conclusions

In this work, novel halogen-free flame-retardant epoxy resins composed of EPN-D with DOPO moiety, HMMM, and n-PF were successfully prepared via an *in situ* polymerization process. Because of the incorporation of HMMM, the obtained thermosets exhibited high $T_g$s, excellent thermal stability, and enhanced the flame retardancy with a high LOI value beyond 45.7. Furthermore, all EPN-D/HMMM/n-PF thermosets could achieve UL-94 V-0 grade without any drippings, which can be attributed to the positive phosphorous-nitrogen synergistic effect on flame retardancy. With these outstanding properties and the absence of a halogen element, such halogen-free epoxy thermosets can be potentially used as the advanced electrical/electronic materials.

## Acknowledgements

The authors are grateful for the support of China Postdoctoral Science Foundation (Grant number: 20060400339).

## References

[1] Derouet D., Morvan F., Bross J. C.: Chemical modification of epoxy resins by dialkyl(or aryl) phosphates: evaluation of fire behavior and thermal stability. Journal of Applied Polymer Science, **62**, 1855–1868 (1996).
DOI: 10.1002/(SICI)1097-4628(19961212)62:11<1855::AID-APP10>3.0.CO;2-Y

[2] Camino G., Costa L., Martinasso G.: Intumescent fire-retardant systems. Polymer Degradation and Stability, **23**, 359–376 (1989).
DOI: 10.1016/0141-3910(89)90058-X

[3] Lu S-Y., Hamerton I.: Recent developments in the chemistry of halogen-free flame retardant polymers. Progress in Polymer Science, **27**, 1661–1712 (2002).
DOI: 10.1016/S0079-6700(02)00018-7

[4] Liu Y. L.: Epoxy resins from novel monomers with a bis-(9,10-dihydro-9-oxa-10-oxide-10-phosphaphenanthrene-10-yl-) substituent. Journal of Polymer Science Part A: Polymer Chemistry, **40**, 359–368 (2002).
DOI: 10.1002/pola.10125

[5] Liu Y-L., Wu C-S., Chiu Y-S., Ho W-H.: Preparation, thermal properties, and flame retardance of epoxy-silica hybrid resins. Journal of Polymer Science Part A: Polymer Chemistry, **41**, 2354–2367 (2003).
DOI: 10.1002/pola.10778

[6] Chiu Y-S., Liu Y-L., Wei W-L., Chen W-Y.: Using diethylphosphites as thermally latent curing agents for epoxy compounds. Journal of Polymer Science Part A: Polymer Chemistry, **41**, 432–440 (2003).
DOI: 10.1002/pola.10578

[7] Liu Y-L., Tsai S-H.: Synthesis and properties of new organosoluble aromatic polyamides with cyclic bulky groups containing phosphorus. Polymer, **43**, 5757–5762 (2002).
DOI: 10.1016/S0032-3861(02)00473-1

[8] Liu Y. L., Wu C. S., Hsu K. Y., Chang T. C.: Flame-retardant epoxy resins from *o*-cresol novolac epoxy cured with a phosphorus-containing aralkyl novolac. Journal of Polymer Science Part A: Polymer Chemistry, **40**, 2329–2339 (2002).
DOI: 10.1002/pola.10320

[9] Liu Y. L., Chang G. P., Wu C. S.: Halogen-free flame retardant epoxy resins from hybrids of phosphorus- or silicon-containing epoxies with an amine resin. Journal of Applied Polymer Science, **102**, 1071–1077 (2006).
DOI: 10.1002/app.24247

[10] Liu Y-L., Chen Y-J.: Novel thermosetting resins based on 4-(N-maleimidophenyl) glycidylether: II. Bismaleimides and polybismaleimides. Polymer, **45**, 1797–1804 (2004).
DOI: 10.1016/j.polymer.2004.01.001

[11] Wu C-S., Liu Y-L.: Preparation and properties of epoxy/amine hybrid resins from in situ polymerization. Journal of Polymer Science Part A: Polymer Chemistry, **42**, 1868–1875 (2004).
DOI: 10.1002/pola.20031

[12] Chiang C-L., Ma C-C. M.: Synthesis, characterization and thermal properties of novel epoxy containing silicon and phosphorus nanocomposites by sol-gel method. European Polymer Journal, **38**, 2219–2224 (2002).
DOI: 10.1016/S0014-3057(02)00123-4

[13] Wu C. S., Liu Y. L., Chiu Y-S.: Synthesis and characterization of new organosoluble polyaspartimides containing phosphorus. Polymer, **43**, 1773–1779 (2002).
DOI: 10.1016/S0032-3861(01)00751-0

[14] Shieh J-Y., Wang C-S.: Synthesis of novel flame retardant epoxy hardeners and properties of cured products. Polymer, **42**, 7617–7625 (2001).
DOI: 10.1016/S0032-3861(01)00257-9

[15] Tarek A., Hajime T., Tsutomu T.: Novel organic-inorganic hybrids prepared from polybenzoxazine and titania using sol-gel process. Polymer, **45**, 7903–7910 (2004).
DOI: 10.1016/j.polymer.2004.09.022

[16] Zhang X. H., Wan H. M., Min Y. Q., Fang Z., Qi G. R.: Synthesis and thermal properties of a novel nitrogen-containing epoxy resin. Chinese Chemical Letters, **16**, 547–550 (2005).

[17] Zhang X. H., Wan H. M., Min Y. Q., Qi G. R.: Novel nitrogen-containing epoxy resin. I. Synthetic kinetics. Journal of Applied Polymer Science, **96**, 723–731 (2005).
DOI: 10.1002/app.21519

[18] Zhang X. H., Min Y. Q., Wan H. M., Qi G. R.: Novel nitrogen-containing epoxy resin. II. Cure kinetics by differential scanning calorimetry. Journal of Applied Polymer Science, **100**, 3483–3489 (2006).
DOI: 10.1002/app.23146

[19] Zhang X. H., Chen S., Min Y. Q., Qi G. R.: Synthesis of novel bisphenol containing phthalazinone and azomethine moieties and thermal properties of cured diamine/bisphenol/DGEBA polymers. Polymer, **47**, 1785–1795 (2006).
DOI: 10.1016/j.polymer.2006.01.075

[20] Min Y. Q., Zhang X. H., Zhao H., Qia G. R.: Synthesis of 2,4,6-tri (hydroxylphenylmethylamino)-s-triazine and its curing behavior and mechanism with DGEBA. Acta Polymerica Sinica, **7**, 855–859 (2006).

[21] Zhang X. H., Chen S., Chen T., Sun X. K., Liu F., Qi G. R.: Synthesis of a soluble azomethine-containing bisphenol and the properties of its modified epoxy thermosets. Journal of Applied Polymer Science, **106**, 1632–1639 (2007).
DOI: 10.1002/app.26712

[22] Zhang X-H., Liu F., Chen S., Qi G-R.: Novel flame retardant thermosets from nitrogen-containing and phosphorus-containing epoxy resins cured with dicyandiamide. Journal of Applied Polymer Science, **106**, 2391–2397 (2007).
DOI: 10.1002/app.26698

[23] Zhang X., Zhou B., Sun X., Qi G.: Preparation and properties of epoxy/phenol formaldehyde novolac/hexakis (methoxymethyl) melamine hybrid resins from *in situ* polymerization. Journal of Applied Polymer Science, **110**, 4084–4092 (2008).
DOI: 10.1002/app.29016

[24] Zhang X. H., Huang L. H., Chen S., Qi G. R.: Improvement of thermal properties and flame retardancy of epoxy-amine thermosets by introducing bisphenol containing azomethine moiety. Express Polymer Letters, **1**, 326–332 (2007).
DOI: 10.3144/expresspolymlett.2007.46

[25] Shau M-D., Wang T-S.: Syntheses, structure, reactivity, and thermal properties of new cyclic phosphine oxide epoxy resins cured by diamines. Journal of Polymer Science Part A: Polymer Chemistry, **34**, 387–396 (1996).
DOI: 10.1002/(SICI)1099-0518(199602)34:3<387::AID-POLA7>3.0.CO;2-R

[26] Espinosa M. A., Galià M., Càdiz V.: Novel flame-retardant thermosets: Phosphine oxide-containing diglycidylether as curing agent of phenolic novolac resins. Journal of Polymer Science Part A: Polymer Chemistry, **42**, 3516–3526 (2004).
DOI: 10.1002/pola.20220

[27] Jeng R-J., Shau S-M., Lin J-J., Su W-C., Chiu Y-S.: Flame retardant epoxy polymers based on all phosphorus-containing components. European Polymer Journal, **38**, 683–693 (2002).
DOI: 10.1016/S0014-3057(01)00246-4

[28] Levchik S. V., Weil E. D.: Thermal decomposition, combustion and flame-retardancy of epoxy resins- A review of the recent literature. Polymer International, **53**, 1901–1929 (2004).
DOI: 10.1002/pi.1473

[29] Iji M., Kiuchi Y.: Self-extinguishing epoxy molding compound with no flame-retarding additives for electronic components. Journal of Materials Science: Materials in Electronics, **12**, 715–723 (2001).

[30] Shieh J-Y., Wang C-S.: Effect of the organophosphate structure on the physical and flame-retardant properties of an epoxy resin. Journal of Polymer Science Part A: Polymer Chemistry, **40**, 369–378 (2002).
DOI: 10.1002/pola.10121

[31] Hong X., Xiao S., Chen Q., Liu H., Chen J., Li W., Chen M., Chen L.: Studies on hybrid polymesization of hexamethoxymethyl melamine-polyol-acrylate. Acta Polymerica Sinica, **3**, 265–270 (2002).

[32] Hsiue G-H., Lee R-H., Jeng R-J.: Organic sol-gel materials for second-order nonlinear optics based on melamines. Journal of Polymer Science Part A: Polymer Chemistry, **37**, 2503–2510 (1999).
DOI: 10.1002/(SICI)1099-0518(19990715)37:14<2503::AID-POLA24>3.0.CO;2-#

[33] van Krevelen D. W.: Some basic aspects of flame resistance of polymeric materials. Polymer, **16**, 615–620 (1975).
DOI: 10.1016/0032-3861(75)90157-3

*eXPRESS Polymer Letters Vol.3, No.12 (2009) 797–803*
*Available online at www.expresspolymlett.com*
*DOI: 10.3144/expresspolymlett.2009.98*

# Thermo-oxidative degradation of graphite/epoxy composite laminates: Modeling and long-term predictions

*O. Ozcelik, L. Aktas, M. C. Altan*[*]

School of Aerospace and Mechanical Engineering, The University of Oklahoma, Norman, OK 73019 USA

*Received 19 July 2009; accepted in revised form 23 September 2009*

**Abstract.** Thermo-oxidative degradation of graphite/epoxy composite laminates due to exposure to elevated temperatures was characterized using weight loss and short beam strength (SBS) reduction data. Test specimens obtained from 24-ply, unidirectional AS4/3501-6 graphite/epoxy laminates were subjected to 100, 150, 175, and 200°C for 5000 hours (208 days) in air. Predictive differential models for the weight loss and short beam strength reduction were developed using the isothermal degradation data only up to 2000 hours. Then, the predictive capabilities of both models were demonstrated using the longer term, 5000 hours degradation data. The proposed models were first order differential expressions that can be used to predict degradation in an arbitrary, time-dependent temperature environment. Both models were able to estimate the actual degradation levels accurately. In particular, excellent agreement was obtained when the degradation temperature was lower than 200°C.

***Keywords:*** *polymer composites, graphite/epoxy laminates, thermo-oxidative degradation, short beam strength*

## 1. Introduction

Despite their low density and excellent mechanical properties, fiber reinforced polymeric composites (FRPCs) are known to be sensitive to environmental factors. In particular, elevated temperatures coupled with oxygen-induced aging can lead to significant reduction in properties as well as a considerable mass loss. These nonreversible changes are frequently referred to as 'thermo-oxidative aging' and are initiated by the diffusion of oxygen into the composite. Elevated temperatures accelerate the oxygen diffusion rate and often lead to oxidation reactions that result in weight loss, microcracks in the resin and resin-fiber debonding [1–3].

Starting with the studies of Greer [4], Nelson [5], and Bowles and Meyers [6], various effects of thermo-oxidative aging on FRPCs have been investigated during the last two to three decades. Obviously, a major goal of such studies is the prediction of long-term degradation behavior and service life of the FRPCs when they are exposed to an arbitrary, time dependent temperature cycle. It is highly impractical to expect full characterization of long-term aging solely by experiments as the time required to carry out such studies is often prohibitive [7]. The modeling efforts have been mostly accomplished by following the changes in one or more degradation parameters such as weight loss, microcrack density or a relevant mechanical property under isothermal conditions. It was also proposed that using the so-called *equivalent property time* and *equivalent cycle time* concepts [8–10], time required to achieve a certain degradation state at one temperature can be used to estimate the time required to induce the same degradation at another temperature. Another method to extend the utility of shorter term experiments is to perform these

---

[*]Corresponding author, e-mail: altan@ou.edu

experiments at high pressures, thus accelerating the rate of oxygen diffusion without altering the temperature sensitive oxidation reaction kinetics [2, 11]. More recently, researchers have tried to establish the link between the degradation kinetics and reduction in mechanical properties in an effort to improve the applicability and predictive capability of aging models [12, 13]. However, to the best of authors' knowledge, the elusive goal of linking diffusive-oxidative phenomenon to changes in mechanical properties of polymeric composites has not been achieved yet.

In this study, the applicability of first order, differential weight loss and strength reduction models beyond the time frame of the data used to develop these models was investigated. This approach would save significant time provided that an acceptable accuracy can be achieved by only using the shorter term data.

## 2. Material and experimental procedure

Twenty-four-ply, unidirectional, graphite/epoxy (i.e., Hercules AS4/3501-6, Hexcel, Connecticut, USA) laminates were used in this study. The Polyacrylonitrile-based (PAN-based) continuous AS4 fibers have a carbon content of 94% [14]. The 3501-6 is a Bisphenol A Diglycidyl Ether (DGEBA) type epoxy resin that has been frequently used in aerospace industry [15]. The detailed composition of 3501-6 has been analyzed by Hou and Bai [16]. The composite material system is expected to be used at temperatures up to the recommended cure temperature of 177°C (350°F) [14]. The laminates in this study were cured in an autoclave using a heat rate of 5°C/min followed by a 3 hours hold at 177°C (350°F) at 206.8 kPa (30 psi) pressure. After the fabrication, short beam strength (SBS) test specimens were prepared as suggested by ASTM D 2344-00. All specimens were subsequently dried in a vacuum oven at 60°C for 8~10 days and kept in a vacuum desiccator until the aging experiments. During aging experiments, the specimens were exposed to four different temperatures: 100, 150, 175, and 200°C for up to 5000 hours (208 days) in air. Effect of thermo-oxidative aging was tracked by monitoring the changes in short beam strength and weight of the specimens. Short beam strength values were calculated in three-point bending test mode. As recommended by ASTM, test span to sample thickness ratio has to be preferably around 4 to obtain accurate short beam strength values. Since the average thickness of the 24-ply samples was around 3.5 mm, a span of 14 mm is used to ensure failure due to interlaminar shear stresses. During the course of aging, groups of specimens were removed from the heating chambers at pre-determined times for strength and weight measurements. The three-point bending tests were carried out at ambient temperature between 20 to 22°C. The sample deflection during testing was recorded by a linear variable differential transformer (LVDT) system, yielding repeatable results within 0.1% of the full deflection scale. In each bending tests, 8 samples were used to minimize the experimental uncertainty.

More than 400 composite samples were tested to develop the models. It should be noted that strength reduction models need to accurately capture the initial rate of degradation where the composites experience the highest rate of strength loss. To achieve this, samples need to be tested more frequently in the early stages of the experiments. In fact, modeling short beam strength degradation is critical for estimating service life of composites as it is more sensitive to thermo-oxidative aging due to its strong dependence on matrix properties. Other mechanical properties such as modulus, tensile or flexural strength are influenced more by the fiber properties, and thus experience moderate degradation compared to short beam strength.

## 3. Thermo-oxidative degradation results

### 3.1. Short term degradation

Percentage weight loss experienced by the composite samples during the first 2000 hours of aging at 100, 150, 175, and 200°C is shown in Figure 1. The temporal evolution of weight loss for each temperature is obtained by weighing the same group of eight samples. Error bars shown in Figure 1 are determined by using 95% confidence interval. The samples are weighed as frequent as necessary to identify a well established trend such that a differential model, which depends on the time rate of change of weight loss, can be developed. Thus, the weight loss of samples subjected to 200°C are measured seven times within the first 250 hours, whereas those exposed to 100°C are only measured three times. Figure 1 indicates that at 100°C, the

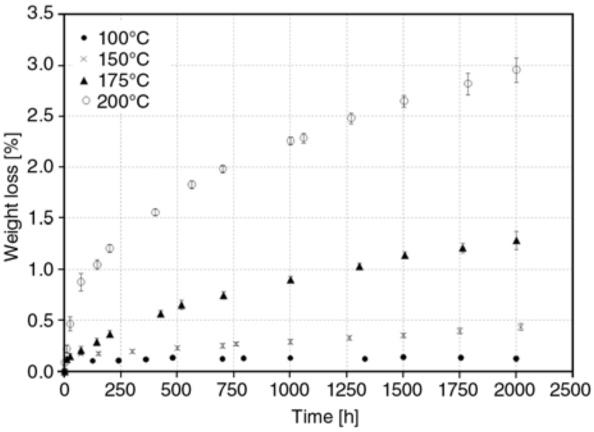

**Figure 1.** Percentage weight loss of the composite specimens subjected to isothermal thermo-oxidative aging at four different temperatures

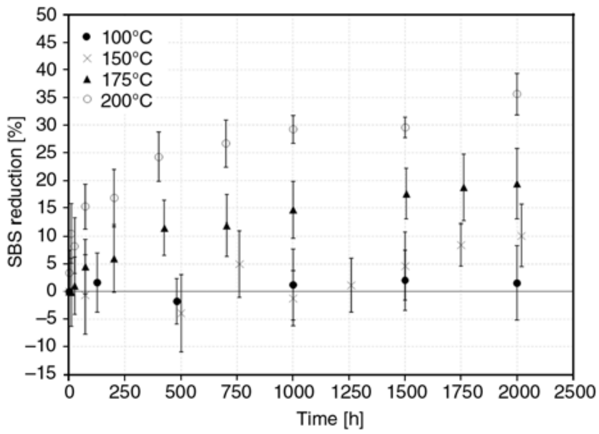

**Figure 2.** Percentage short beam strength reduction of the composite specimens subjected to isothermal thermo-oxidative aging at four different temperatures

samples experienced less than 0.2% weight loss which remained constant after the first 100 hours of aging. This finite and very small weight loss is possibly due to desorption of moisture that was already in the samples. The fact that the weight loss have not increased with time corroborates this assessment. Samples exposed to 175 and 200°C show higher rates of weight loss within the first 500 hours. Rates of weight loss reduced considerably after 1000 hours of aging. Since the same group of eight composite samples was used for each temperature, the variation of percent weight loss at a particular time is very small within a sample group. Hence, the error bars shown in Figure 1 are very small, indicating minimal experimental uncertainty. It is important to point out that the glass transition temperature, $T_g$, of this composite laminate is less than 200°C, most likely between 190 to 195°C when it is fully cured [14, 17]. Thus thermo-oxidative aging at 200°C is slightly above glass transition such that the degradation is taking place in the rubbery phase. Clearly, these composite laminates will not be designed to function above glass transition; however, they might experience unexpected overheating or other thermal events that may raise the temperature temporarily above their glass transition. It is very desirable to assess the structural health and the damage sustained by the composite part after such an event. Investigating the effect of an aging temperature above the glass transition is especially meaningful as the possibility of having a single predictive model – as opposed to having separate models for below and above glass transition – for a wider temperature range is very appealing.

Figure 2 illustrates the percent reduction of short beam strength at 100, 150, 175, and 200°C up to 2000 hours of aging. To obtain the percent short beam strength reduction at different times, the measured strength values of eight aged samples were compared with those of the 27 unaged specimens that were tested earlier. The testing of 27 unaged specimens gave an initial SBS value of 87.06±2.8 MPa at 95% confidence interval. At the start of the experiments, testing a much higher number of unaged samples was important to establish a reliable baseline value for SBS. It is obvious from Figure 2 that the variation of short beam strength within a sample set is much larger than the weight loss as indicated by the larger uncertainty bars. Considering that a new sample set is tested for each data point and the inherent uncertainty in characterizing strength of composites, the variation observed in Figure 2 is rather modest. Similar to the weight loss measurements, strength data is obtained at much shorter intervals during the initial phase of aging. By testing considerable number of samples within the first 250 hours, initial degradation rates are expected to be characterized sufficiently accurate for model development.

Samples aged at 100°C did not show a discernable strength reduction within the first 2000 hours. Unchanged strength values validate the earlier assessment that the initial weight loss observed in these samples were in fact due to the loss of moisture within the samples. Hence, data obtained at 100°C are not used in degradation models developed later.

Samples aged at higher temperatures depict a well-defined strength reduction trend that steadily increases with time and temperature. After 2000 hours of aging, samples exposed to 150, 175 and 200°C suffered approximately 10, 20 and 35% reduction in short beam strength, respectively. It is also observed that composite laminates at 200°C experienced a much rapid degradation, suffering more than 10% strength loss within the first 24 hours. The same level of strength reduction is reached only after 400 and 2000 hours for samples exposed to 175 and 150°C, respectively.

### 3.2. Predictive modeling

To develop predictive thermo-oxidative degradation models, the time rate of reduction of any composite property including its weight is chosen to be written in Equation (1):

$$\frac{d\phi}{dt} = g(T,\phi) \tag{1}$$

where $\phi$ is the degradation parameter and $T$ represents the temperature. In this study $\phi$ is defined to be either weight loss or SBS reduction; however it can be applied to capture the change of any other property. It is emphasized that in Equation (1), the functional form of $g(T,\phi)$ and thus, the specific formulation of temperature effect in $g(T,\phi)$ is not known a priori. Rather, it is left to be determined by the trend observed in experimental data. Once $g(T,\phi)$ is properly identified, the reduction in the property $\phi$ can be determined by solving a first order differential equation.

The premise in Equation (1) is that the thermo-oxidative degradation of composites can be expressed by a first order, phenomenological model. That is, temporal evolution of weight loss or SBS reduction during aging essentially exhibits a mathematical structure that can be predicted from a first order differential equation. Similar first order models have been used to describe oxidation reactions, where the function $g(T,\phi)$ can be separated as the product of two functions (i.e., $K(T)g(\phi)$). In addition to thermal aging, Equation (1), in this generic form, has been used to develop phenomenological models for various other applications, including cure modeling of thermoset resins and composite prepregs, and also for describing microstructural changes [18–22]. The first step in developing such a model involves construction of $d\phi/dt$ from the experimental data. The construction of this rate information requires data to be collected at sufficiently frequent intervals to form an accurate picture of the time rate of change of the degradation parameter, $\phi$. The subsequent construction of $d\phi/dt$ versus $\phi$ curves for the isothermal aging temperatures helps identify the suitable functional forms for $g(T,\phi)$.

In this study, the selection of the functional form of $g(T,\phi)$ and the other temperature dependent model parameters was dictated by the ability of the model to recover the isothermal aging data accurately. This was achieved by maximizing the correlation coefficient of the curve fit during the selection of model parameters and their dependence on temperature. By following this procedure, the best fit for the model parameters was obtained regardless of the scatter in the data.

Considering the data in Figure 1, a three-parameter model accurately represents the evolution of the percentage weight loss, $W_l$ (Equation (2)):

$$\frac{dW_l}{dt} = a\exp[bW_l^c] \tag{2}$$

where $a$, $b$, and $c$ are the temperature dependent model parameters. These model parameters are expressed as a linear function of temperature (Equation (3)):

$$a = 5.64{\cdot}10^{-4}T - 0.0908 \tag{3a}$$

$$b = 0.0400T - 9.762 \tag{3b}$$

$$c = 0.0148T - 2.260 \tag{3c}$$

where $T$ represents aging temperature. For aging at 150°C, a linear model seemed to work better as the weight loss increased slowly at a constant rate. Thus, instead of Equations (2)–(3), the linearized model, $W_l = At + B$ where $A = 1.314{\cdot}10^{-4}$ and $B = 0.1648$ is more suitable. It can be easily seen that the initial rate of weight loss at $t = 0$ is estimated by these models as $W_l = 1.314{\cdot}10^{-4}$, 0.0079, 0.022% per hour for 150, 175 and 200°C, respectively.

In developing the short beam strength reduction model, a similar procedure is implemented to the data shown in Figure 2. The short beam strength of the specimens exposed to 100°C did not show a remarkable drop-off throughout the 2000 hours aging. Therefore, as in the weight loss model, 100°C-data were excluded from the strength reduction model. In this case, a simpler two-parameter model for strength reduction worked better for all three temperatures. The time rate of reduction of strength is expressed by an exponential function given as Equation (4):

$$\frac{\mathrm{d}\sigma}{\mathrm{d}t} = \kappa\exp(\lambda\sigma) \tag{4}$$

where σ is the percentage reduction in short beam strength, and κ and λ are temperature dependent model parameters. Within the range of 150 to 200°C, the parameters κ and λ were expressed in Equation (5):

$$\kappa = (1.256\cdot10^{-3})T^2 - (0.405)T + 32.569 \tag{5a}$$

$$\lambda = (1.895\cdot10^{-5})T^2 - (8.327\cdot10^{-3})T + 0.712 \tag{5b}$$

Although the model given in Equations (4)–(5) only contains two parameters, κ and λ, the temperature dependency of these parameters did not yield a linear relationship. The model estimates the initial rates of short beam strength loss at $t = 0$ as 0.079, 0.159, and 1.809% per hour for 150, 175 and 200°C, respectively. These initial rates are approximate values obtained for $t \to 0$. As time increases, the strength reduction rates rapidly change, especially for higher temperatures. Nevertheless, the estimates of strength reduction as $t \to 0$ provide valuable guideline regarding the severeness of the initial degradation.

### 3.3. Long-term predictions and model validation

The applicability of the weight loss and short beam strength reduction models to longer time frames was analyzed. Although these models have been developed by using only 2000 hours of aging data, applying them to longer periods is desirable. Such an approach would save significant time in experimental characterization of composite degradation, provided that the desired accuracy is still maintained. In the present study, extending the time frame of the models by 2.5 times from 2000 to 5000 hours will demonstrate the utility and robustness of the models. To validate this approach, predictions of both models for 5000 hours aging are compared with the actual experimental data.

The weight loss model given by Equations (2)–(3) is numerically solved up to 5000 hours. The solution is rather straight forward since the standard fourth-order Runge-Kutta method yields the desired numerical accuracy. Figure 3 shows the experimental and predicted percentage weight loss up to 5000 hours. The solid lines illustrate the model predictions up to 2000 hours, the time frame used in model development. Dashed lines depict extension of model predictions up to 5000 hours. As explained earlier, the samples aged at 100°C did not suffer any weight loss beyond the initial phase of moisture desorption. The model performed very well for samples aged at 150 and 175°C, with weight loss estimates falling almost within the measured experimental uncertainty. It seems that at 150 and 175°C, the model would continue to predict weight loss accurately, even after 5000 hours. For aging at 200°C, the model, however, loses accuracy, such that the experimental data starts diverging from the established trend shortly after 2500 hours. At 5000 hours, the model predicts a weight loss of 4%, whereas experimental data indicates an almost 6% weight loss. It is worth noting that experimental uncertainty increases considerably after 2500 hours, as observed by the continual increase in the size of the error bars up until 5000 hours. This deviation from the initial trend points to an acceleration in degradation mechanism.

Although, the reasons for this acceleration in degradation have not been identified, it could possibly be

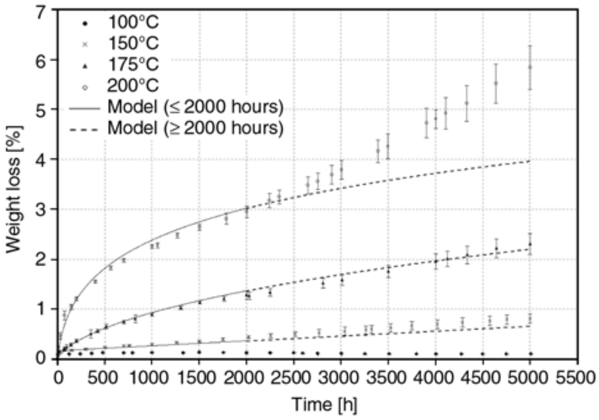

**Figure 3.** Experimental and predicted percentage weight loss of the composite specimens subjected to thermo-oxidative aging up to 5000 hours. Solid lines represent the predictions within the first 2000 hours for which the models were developed. Dashed line represents the extension of model predictions up to 5000 hours.

due to further weakening of the overall fiber-matrix interface, severe delamination or acceleration of microcrack growth along the fibers at the interphase region. A detailed microscopic examination of the samples was not performed to establish the leading cause of degradation at higher temperatures; however, the surface morphology of the samples displayed visible changes such as charring and discoloration after being exposed to 200°C for 5000 hours. From a modeling perspective, higher order effects that were not captured by the first order models may be becoming dominant at later stages of degradation. Such effects could be included in the models at the expense of adding mathematical complexity. For example, both reaction and diffusion controlled degradation effects could be captured by a combination of both first and second order temporal differentials.

Figure 4 shows the experimental and predicted percent reduction in short beam strength up to 5000 hours. Samples aged at 100°C did not suffer any identifiable strength loss as expected. Model predictions and experimental results for 150, 175 and 200°C are observed to agree very well, with the vast majority of model estimates falling within the range of experimental uncertainty. Model performance for aging at 150°C has been excellent, where the composite samples suffer a 10.8% strength reduction after 5000 hours. Model predictions also show excellent agreement up to 4000 hours for aging at 175°C where the samples record 24.9% strength reduction. These results indicate that although the material system AS4/3501-6 has been developed for use up to 177°C, exposure to temperatures as low as 150°C for longer periods could lead to delamination failure due to interlaminar shear stresses. Therefore, it is essential to account for the thermo-oxidative degradation in estimating service life if the composite product is to be exposed to elevated temperatures.

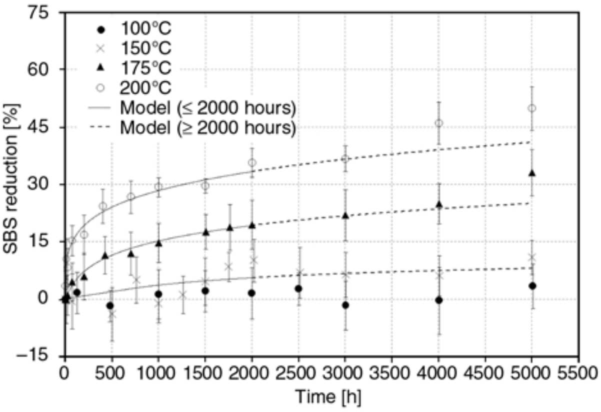

**Figure 4.** Experimental and predicted percentage short beam strength reduction of the composite specimens subjected to thermo-oxidative aging up to 5000 hours. Solid lines represent the predictions within the first 2000 hours for which the models were developed. Dashed line represents the extension of model predictions up to 5000 hours.

For 200°C, the model predictions are excellent up to 3000 hours, where the samples record 36.7% strength reduction. The accelerated pace of weight loss observed at 200°C did not lead to a similar rapid increase in the strength loss. There is some deviation observed in model predictions for 200°C at 4000 and 5000 hours. However, at these levels, the samples have already lost more than 45% of their initial strength. In most practical applications, these samples would be viewed as failed – if not already failed in service – and therefore would be replaced before reaching such excessive levels of degradation. Overall, the strength loss model performed very well for all the temperatures and well beyond the time frame for which it was developed.

## 4. Conclusions

Thermo-oxidative aging of 24-ply, aerospace-grade AS4/3501-6 graphite/epoxy composite laminates is investigated by characterizing the weight loss and reduction in short beam strength at 100, 150, 175 and 200°C. First order differential models are developed for the percentage weight loss and short beam strength reduction using the isothermal aging data up to 2000 hours. These models can be used to predict thermo-oxidative aging when the composite is exposed to an arbitrary time-dependent temperature profile. The utility of these models were demonstrated by successfully predicting the actual weight loss and strength reduction up to 5000 hours, well beyond 2000 hours for which the models were developed. Thus, it is possible to develop robust models using shorter term, isothermal aging data which would yield sufficiently accurate results over a much longer time frame.

The material was shown to be highly stable at 100°C such that no significant weight loss or strength reduction was observed during 5000 hours of aging. After 5000 hours, the laminates suffered 0.81, 2.31, and 5.84% weight loss coupled with

10.87, 33.07, and 49.86% short beam strength reduction at 150, 175, and 200°C, respectively. Compared to aging at 150 and 175°C, aging at 200°C led to rapid strength reduction of more than 20% within the first 400 hours. Overall, the weight loss and strength reduction models predicted data accurately, particularly when the weight loss is less than 3% and the strength reduction is less than 35%.

## References

[1] Colin X., Verdu J.: Thermal ageing and lifetime prediction for organic matrix composites. Plastics, Rubber and Composites, **32**, 349–356 (2003).
DOI: 10.1179/146580103225004117

[2] Tsotsis T. K., Keller S., Bardis J., Bish J.: Preliminary evaluation of the use of elevated pressure to accelerate thermo-oxidative aging in composites. Polymer Degradation and Stability, **64**, 207–212 (1999).
DOI: 10.1016/S0141-3910(98)00190-6

[3] Burcham L. J., Eduljee R. F., Gillespie Jr. J. W.: Investigation of the microcracking behavior of bismaleimide composites during thermal aging. Polymer Composites, **16**, 507–517 (1995).
DOI: 10.1002/pc.750160609

[4] Greer R. H.: Thermal aging of contemporary graphite/epoxy materials. in 'Proceedings of 24th International SAMPE Symposium and Exhibition. San Francisco, USA' 1039–1052 (1979).

[5] Nelson J. B.: Thermal aging of graphite/polyimide composites. in: 'Long-term behavior of composites' (ed.: O'Brien T. K.) ASTM STP 813, Philadelphia, 206–221 (1983).

[6] Bowles K. J., Meyers A.: Specimen geometry effects on graphite/PMR-15 composites during thermo-oxidative aging. in 'Proceedings of 31st International SAMPE Symposium and Exhibition. Las Vegas, USA' 1285–1299 (1986).

[7] McManus H. L., Foch B. J., Cunningham R. A.: Mechanism-based modeling of long-term degradation. Journal of Composites Technology and Research, **22**, 146–152 (2000).

[8] Salin I. M., Seferis J. C., Loechelt C. L., Rothschilds R.: Time-temperature equivalence in thermogravimetry for BMI composites. SAMPE Quarterly, 24, 54–62 (1992).

[9] Seferis J. C.: Aging analyses of polymer composites through time-temperature equivalence. Journal of Composites Technology and Research, **21**, 173–179 (1999).

[10] Chung K., Seferis J. C., Nam J-D.: Investigation of thermal degradation behavior of polymeric composites: Prediction of thermal cycling effect from isothermal data. Composites Part A: Applied Science and Manufacturing, **31**, 945–957 (2000).
DOI: 10.1016/S1359-835X(00)00043-9

[11] Tsotsis T. K., Keller S., Lee K., Bardis J., Bish J.: Aging of polymeric composite specimens for 5000 hours at elevated pressure and temperature. Composites Science and Technology, **61**, 75–86 (2001).
DOI: 10.1016/S0266-3538(00)00196-2

[12] Rasoldier N., Colin X., Verdu J., Bocquet M., Olivier L., Chocinski-Arnault L., Lafarie-Frenot M. C.: Model systems for thermo-oxidised epoxy composite matrices. Composites Part A: Applied Science and Manufacturing, **39**, 1522–1529 (2008).
DOI: 10.1016/j.compositesa.2008.05.016

[13] Dao B., Hodgkin J., Krstina J., Mardel J., Tian W.: Accelerated aging versus realistic aging in aerospace composite materials. II. Chemistry of thermal aging in a structural composite. Journal of Applied Polymer Science, **102**, 3221–3232 (2006).
DOI: 10.1002/app.24573

[14] Kim J., Moon T. J., Howell J. R.: Cure kinetic model, heat of reaction, and glass transition temperature of AS4/3501-6 graphite-epoxy prepregs. Journal of Composite Materials, **36**, 2479–2498 (2002).
DOI: 10.1177/0021998302036021712

[15] Kim Y. K., White S. R.: Stress relaxation behavior of 3501-6 epoxy resin during cure. Polymer Engineering and Science, **36**, 2852–2862 (1996).
DOI: 10.1002/pen.10686

[16] Hou T. H., Bai J. M.: A semi-empirical approach for the chemoviscosity modeling of reactive resin system. SAMPE Journal, **24**, 43–51 (1988).

[17] Howsmon S. C.: Viscoelastic and mechanical properties of Hercules 3501-6 epoxy resin and its prepreg. Master's thesis, The University of Oklahoma (2005).

[18] Loos A. C., Springer G. S.: Curing of epoxy matrix composites. Journal of Composite Materials, **17**, 135–169 (1983).
DOI: 10.1177/002199838301700204

[19] Hargis M., Grady B. P., Aktas L., Bomireddy K. R., Howsmon S., Altan M. C., Rose T., Rose H.: Calorimetric and rheological measurements of three commercial thermosetting prepreg epoxies. Journal of Composite Materials, **40**, 873–897 (2006).
DOI: 10.1177/0021998305056380

[20] Wetzel E. D., Don R. C., Gillespie Jr. J. W.: Modeling thermal degradation during thermoplastic fusion bonding of thermoset composites. in 'Proceedings of Society of Plastics Engineers 52nd Annual Technical Conference (ANTEC '94). San Francisco, USA' 1263–1268 (1994).

[21] Nam J-D., Seferis J. C.: Generalized composite degradation kinetics for polymeric systems under isothermal and nonisothermal conditions. Journal of Polymer Science Part B: Polymer Physics, **30**, 455–463 (1992).
DOI: 10.1002/polb.1992.090300505

[22] Hancox N. L.: Thermal effects on polymer matrix composites: Part 2. Thermal degradation. Materials and Design, **19**, 93–97 (1998).
DOI: 10.1016/S0261-3069(98)00019-3

*eXPRESS Polymer Letters Vol.3, No.12 (2009) 804–813*
*Available online at www.expresspolymlett.com*
*DOI: 10.3144/expresspolymlett.2009.99*

# Wavelet-based acoustic emission characterization of damage mechanism in composite materials under mode I delamination at different interfaces

*A. R. Oskouei, M. Ahmadi*, M. Hajikhani*

Non-destructive Testing Lab., Department of Mechanical Engineering, Amirkabir University of Technology, 424 Hafez Ave., 15914, Tehran, Iran

*Received 13 July 2009; accepted in revised form 29 September 2009*

---

**Abstract.** In this paper, acoustic emission (AE) monitoring with a wavelet-based signal processing technique is developed to detect the damage types during mode I delamination on glass/polyester composite materials. Two types of specimen at different midplane layups, woven/woven (T3) and unidirectional/unidirectional (T5), leading to different levels of damage evolution, were studied. Double cantilever beam (DCB) is applied to simulate delamination process for all specimens. Firstly, the obtained AE signals are decomposed into various wavelet levels. Each level includes detail and approximation that are called components and related to a specific frequency range. Secondly, the energy distribution criterion is applied to find the more significant components each one of which is in relation to a distinct type of damage. The results show that the energy of AE signals has been concentrated in three significant components for both of the specimens. There is a difference in energy distribution of similar components of two specimens. It indicates that there is a dissimilar dominant damage mechanism for two different interfaces during the delamination process. Additionally, the microscopic observation (SEM) is used to determine how the different fracture mechanisms are related to the dominant corresponding wavelet components.

***Keywords:*** *damage mechanism, polymer composites, delamination, acoustic emission, wavelet packet*

---

## 1. Introduction

The main fracture mode that has an effect on the residual strength of composite materials is delamination. Mode I inter-laminar fracture has received the greatest attention, and various standards have been developed for the double cantilever beam (DCB) test [1].

In order to identify the type of damage in composites, which involves fiber failure, the transverse failure and delamination, the acoustic emission (AE) technique is also promising for the detection of the damage type [2]. This technique is based on the detection of elastic surface stress waves caused by the dissipation of elastic energy due to the opening of a crack or plastic deformation. Several studies were already conducted on the mode I fracture to determine the surface energies of composite materials by creating a crack propagation effect [3, 4].

To find correlation between AE parameters and damage mechanism several studies have been carried out [5–9]. Most studies so far have used AE descriptors such as counts, amplitude, energy and also multiparameter method to characterize the development of failure mechanisms. In this way, Siron *et al.* [10] used AE waveform parameters to investigate damage indicators which are related to the physical damage of the composite. Ramirez-Jimenez *et al.* [11] have applied the frequency method to identify the failure modes in glass/

---

*Corresponding author, e-mail: ahmadin@aut.ac.ir

polypropylene composites. The results showed that 100 kHz primary event frequency is due to the fiber/matrix debonding, those between 200 and 300 kHz are due to the fiber slippage and fiber pull out and the two higher frequencies appearing in all tests are related to the fiber breaking. Similar results are obtained by Haselbach and Lauke [12] for evaluating the debonding between fiber and matrix. It was found that debonding is accompanied by signals showing the amplitudes smaller than 45 dB and conspicuous frequencies above 250 kHz at one or more hits of an event.

Many of the useful information get averaged/lost, while transforming a signal from one domain to another. These problems have been successfully eliminated by the introduction of time-frequency distributions. Among them, wavelet transform is one of the most promising methods followed in engineering. Ni and Iwamoto [13] concluded that using the time-frequency method of the wavelet transform, the microfailure modes at a fiber breakage and the microfracture mechanism, such as the sequence of each failure mode and their interaction, were clearer. Qi and coworkers [14, 15] applied the wavelet transform to analyze AE signals by decomposing the signal into different wavelet levels. Each level represents the components of the decomposed AE signal within a certain frequency range. The energy criteria at each level were used to identify the dominant fracture mechanism in an order. A similar work was presented on damage evolution in center-hole glass/polyester composites by Loutas *et al.* [16].

From the above literature review, it appears that there are several different approaches to the event recognition analysis. In this paper, wavelet packet transform method was applied to provide the relevant information from AE signal to discriminate the damage types. The AE signals used for this analysis have been measured during quasi-static loading. The energy criterion has been used for analyzing each level of AE signals which were decomposed by the wavelet method. The energy criterion is used to find the dominant levels that were related to different failure modes. Additionally, wavelet-based method was combined with microscopic observations by SEM to verify the results of the wavelet analysis. This provides the optimal understanding of the occurrence and the evolution of the basic damage mechanisms.

## 2. Experimental procedure

### 2.1. Materials and specimen manufacturing

Standard double cantilever beam (DCB) specimens were prepared according to the ASTM Standard D5528 [1]. The composite used in this study is the polyester resin (unsaturated resin, S. S. P. Co., Iran) reinforced by the E-glass woven and unidirectional fiber (S. S. P. Co., Iran) with the densities and weights of 1.12 g/cm$^3$, 292 g/m$^2$ and 500 g/m$^2$, respectively. The laminates were prepared by hand lay-up with compression molding. The starter crack was formed by inserting a Teflon film at mid-thickness during the molding. Two different specimens which have the same lay-up of [Woven/Unidirectional]$_{5S}$ and different in the midplane interfaces are used. In particular the following specimen midplane interface types have been considered: woven/woven (T3), and unidirectional/unidirectional (T5). The fiber volume fraction was 60% for all specimens. The loading blocks were bonded at one end of starter crack in two sides to apply the opening force for delamination. The specimens were prepared with a length of 250 mm, width of 20 mm, thickness of 5 mm, and a starter crack has a length of 70 mm and the width of 20 mm.

### 2.2. Test

The tests were carried out in a universal test machine (Hiwa Co., Tehran, Iran) with the load cell capacity of 1000 N at the cross head speed of 0.2 mm/min. Five samples for each laminate lay-up were used for DCB testing. Each specimen was equipped with an acoustic emission sensor at one end of DCB specimen (Figure 1). The acoustic emission software AEWin and a data acquisition system (PAC) PCI-2 with a maximum sampling rate of 40 MHz were used for recording AE events. A broadband, resonant-type, single-crystal piezoelectric transducer from Physical Acoustics Corpo-

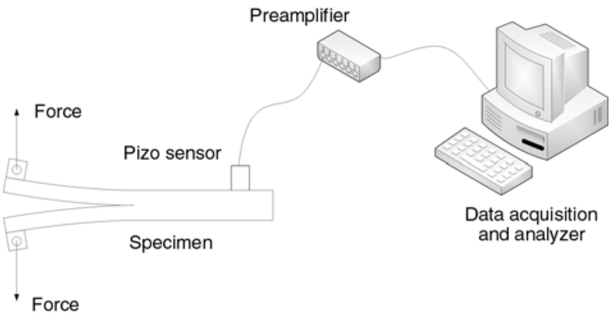

**Figure 1.** DCB test setup

ration (PAC), called PICO, was used as the AE sensor. The sensor had a resonance frequency of 513.28 kHz, and an optimum operating range of 100–750 kHz. AE activities were detected by sensor and amplified by the preamplifier with 40 dB gain. To improve the signals transmission between specimens and sensor, vacuum silicon grease is used. For avoiding background noise during the sampling, the threshold level was set in 35 dB.

## 3. Wavelet transform

Wavelet transform (WT) has been used as a new method in signal and image processing in last two decades. Some researcher applied the wavelet transform method to analyze acoustic emission (AE) signals [13–17]. Wavelet is a waveform with an effectively limited duration and zero average value. Mathematically, consider a function $\psi$ with the following properties [18–20]:

1. The function integrates with zero (Equation (1)):

$$\int_{-\infty}^{-\infty} \psi(t)\mathrm{d}t = 0 \tag{1}$$

2. It is square integrable or, equivalently, has finite energy (Equation (2)):

$$\int_{-\infty}^{+\infty} \left|\psi(t)\right|^2 \mathrm{d}t < \infty \tag{2}$$

The function $\psi(t)$ is called a mother wavelet or wavelet if it satisfies these two properties as obtained from Equations (1), (2).

Let $f(t)$ be any square integrable function. The CWT or continuous-time wavelet transform of $f(t)$ with respect to a wavelet $\psi$ is defined by Equation (3):

$$CWT(a,b) = \frac{1}{\sqrt{a}} \int_{-\infty}^{+\infty} f(t)\psi^*\left(\frac{t-b}{a}\right)\mathrm{d}t \tag{3}$$

where the variable $b$ represents time shift or translation, $a$ refers to the scale or dilation variable and * denotes the complex conjugation of wavelet. The inverse continuous wavelet transform can be expressed as [18] (Equations (4), (5)):

$$f(t) = \frac{1}{C} \int_{a=-\infty}^{+\infty} \int_{b=-\infty}^{+\infty} \frac{1}{\left|a\right|^2} CWT(a,b)\,\psi(t)\,\mathrm{d}a\mathrm{d}b \tag{4}$$

$$C = \int_{-\infty}^{-\infty} \frac{\left|\psi(\omega)^2\right|}{\omega}\mathrm{d}\omega \tag{5}$$

Observe that in contrast to Equation (4), which involves $a$ continuum of the dilations and $b$ translations, Equation (6) uses discrete values for these parameters. It means that the dilation takes values of the form $a = 2^j$ where $j$ is an integer. At any dilation $2^j$, the translation parameter takes the values of the form $2^j \cdot k$ where $k$ is again an integer [18].

Mathematically, this procedure is described by Equation (6):

$$f(t) = c\sum_j \sum_k DWT(j,k)2^{-j/2}\psi(2^{-j}t-k) \tag{6}$$

The inverse discrete wavelet transform can be expressed by Equation (7):

$$DWT(j,k) = \int_{-\infty}^{+\infty} f(t)2^{j/2}\psi^*(2^j t-k)\mathrm{d}t \tag{7}$$

where $DWT(j,k)$ are the wavelet transform coefficients given by a two-dimensional matrix, $j$ is called the level that is related to the frequency domain of the signal and $k$ is in relation to the time domain. $f(t)$ is the signal that is analyzed and $\psi$ the wavelet used for the analysis.

In the wavelet analysis, a signal is broken apart to an approximation and a detail. The approximations are the low-frequency components of the signal and the details are the high-frequency ones. The approximation is then itself broken apart to a second-level approximation and detail, and the process is repeated to obtain the optimal results [19]. As a result, the signal can be decomposed into a tree structure with wavelet details and wavelet approximations at various levels as shown by Equation (8) [21]:

$$f(t) = \sum_{i=1}^{i=j} D_i(t) + A_j(t) \tag{8}$$

where $D_i(t)$ denotes the wavelet detail and $A_j(t)$ stands for the wavelet approximation at the $j$th level, respectively. A graphical representation of DWT of a signal is shown in Figure 2.

The decomposition process of only the approximation component at each level may cause problems while applying DWT in certain applications, where the important information is located in higher frequency components. So, the wavelet packet trans-

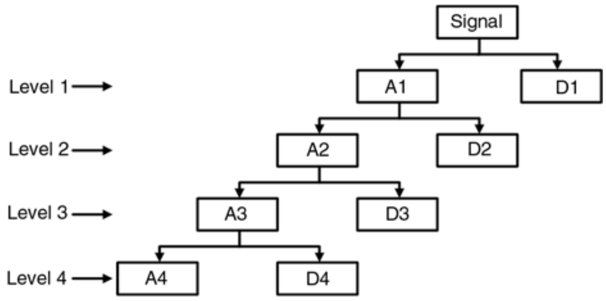

**Figure 2.** Discrete wavelet transform decomposition tree

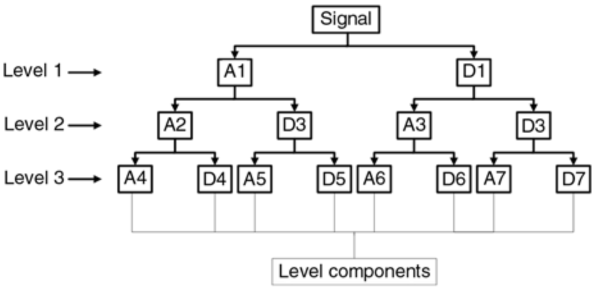

**Figure 3.** Wavelet packet transform tree

form can resolve this difficulty if a wavelet detail component is also further decomposed in order to obtain its own approximation and detail components (Figure 3). We should note here that in this paper all parts of each level is called component (including details and approximations) and the number of components of level $j$ is equal to $2^j$.

A wavelet packet is represented as a function, $\psi^i_{j,k}$ where $i$ is the modulation parameter, $j$ is the dilation parameter and $k$ is the translation parameter (Equation (9)):

$$\psi^i_{j,k}(t) = 2^{-j/2}\psi^i(2^{-j}t-k) \tag{9}$$

Here, $i = 1, 2,\ldots, j^n$ and $n$ is the level of decomposition in wavelet packet tree. The wavelet $\psi^i$ is obtained through the following recursive relationships (Equations (10) and (11)):

$$\psi^{2i}(t) = \frac{1}{\sqrt{2}}\sum_{k=-\infty}^{+\infty} h(k)\psi^i\left(\frac{t}{2}-k\right) \tag{10}$$

$$\psi^{2i+1}(t) = \frac{1}{\sqrt{2}}\sum_{k=-\infty}^{+\infty} g(k)\psi^i\left(\frac{t}{2}-k\right) \tag{11}$$

Here, $\psi^i$ is called a mother wavelet and the discrete filters $h(k)$ and $g(k)$ are quadrature mirror filters associated with the scaling function and the mother wavelet function [18].

The wavelet packet coefficients $c^i_{j,k}$ corresponding to the signal $f(t)$ can be obtained by Equation (12):

$$c^i_{j,k} = \int_{-\infty}^{+\infty} f(t)\psi^i_{j,k}(t)\mathrm{d}t \tag{12}$$

The wavelet packet component of the signal at a particular node can be obtained by Equation (13):

$$f^i_j(t) = \sum_{k=-\infty}^{+\infty} c^i_{j,k}\psi^i_{j,k}(t)\Delta t \tag{13}$$

After performing the wavelet packet decomposition up to $j$th level, the original signal can be represented as a summation of all wavelet packet components at $j$th level as shown in Equation (14):

$$f(t) = \sum_{i=1}^{2^j} f^i_j(t) \tag{14}$$

Based on the relation of frequency structure of wavelet decomposition, the frequency bandwidth of the approximation and detail of level $j$ are defined in Equations (15) and (16):

The frequency bandwidth of approximation:

$$\left[0, \frac{1}{2}f_s 2^{-j}\right] \tag{15}$$

The frequency bandwidth of detail:

$$\left[\frac{1}{2}f_s 2^{-j}, \frac{1}{2}f_s 2^{-(j-1)}\right] \tag{16}$$

where $f_s$ is the sampling rate.

## 4. Wavelet-based methodology for acoustic emission signals analysis

The base theory of wavelet was introduced in the previous section. It was understood that any signal can be decomposed into a set of wavelet component, each having its specific frequency range. In this work, for analyzing the AE signals, we focus on the energy criteria because of the different distribution of energy in each component that can be related to the specific failure mode. So, this idea can be the theoretical basis of the work discussed below.

If $f(t)$ is an AE signal based on Equation (12), it is possible to decompose the signal to wavelet components where $f^1_j \ldots f^i_j$ are the components of $j$th level of the decomposed signal. According to the level of decomposed signal, $E^1_j \ldots E^i_j$ can be defined as the component energy at level $j$. This is mathematically expressed by Equation (17):

$$E_j^i(t) = \sum_{\tau=t_0}^{t} \left(f_j^i(\tau)\right)^2 \tag{17}$$

And the total energy of signal is defined by Equation (18):

$$E_{Total}(t) = \sum_j E_j^i(t) \tag{18}$$

In this work, the ratio of energies at different levels to the total energy is considered in order to find energy distribution displayed at different components. Let it be defined by Equation (19):

$$P_j^i(t) = \frac{E_j^i(t)}{E_{Total}(t)}, \quad i = 1\ldots 2^j \tag{19}$$

In this manner, $P_j^i(t)$ gives a relative energy distribution at each level.

## 5. Results and discussion

During a typical quasi-static loading of the composite material under mode I delamination, a large number of AE waveforms (Events) are recorded. Figure 4 shows the typical raw waveform of AE events in the time domain during the loading of composite material. These events have important roles in the analysis. In Figure 5, a load-time plot and its relationship with AE event energy for specimen T3 is shown. Completely different AE behavior was noticed where AE energies were first detected at the early stage of loading with alternating appearances during delamination. There is no event at the fist stage of loading and all the energy of loading is absorbed by the bending of the DCB specimen beams. But near the maximum load some AE events are detected and crack is being propagated.

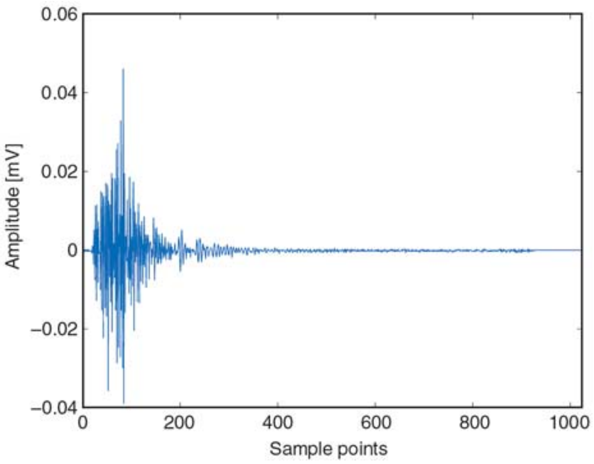

**Figure 4.** Typical AE waveform

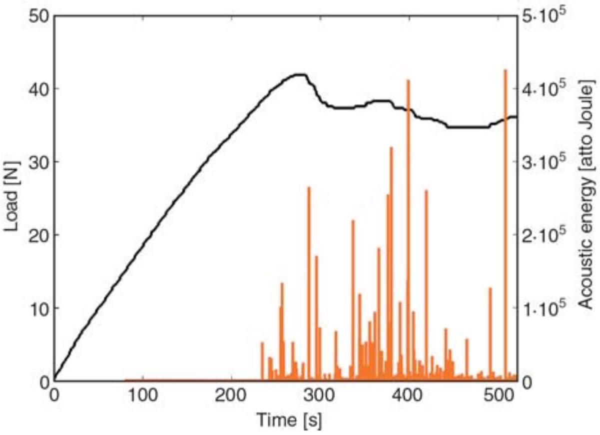

**Figure 5.** Delamination load and AE signal energy vs. time

For the analysis of waveforms, MATLAB software has been chosen since it has wavelet toolbox with numerous options and it is possible to create codes according to the application field. The code developed by the author was utilized to perform the wavelet based AE analysis. At first, we used the discrete wavelet transform as a rule of thumb to find an approximate range of energy concentration of signals. But, for the detailed information, we applied wavelet packet transform. In this way, wavelet detail components are also further decomposed to obtain its own approximation and detail. Because of splitting the wavelet detail component to its own approximation and detail, the frequency range is also split to two equal frequency ranges. By this technique, we can improve the relationship between the failure modes and corresponding frequency range. The existence of narrow band range of frequency in this method is the importance of this method rather than other wavelet transform methods which obtained the frequency range in wider range for the typical failure mode.

The wavelet packet transform (WPT) is applied to every signal. The application of wavelet packet analysis to the acquired AE signal results in its decomposition into three different levels of processed data. The mathematical criteria called entropy criteria [16, 22] are used to determine if certain decomposition is sufficient or more levels are needed. There are a lot of wavelet families that were used in the analysis, one of which was called Daubechies' wavelet [18, 19], and was applied in the current work. The detail results are obtained in

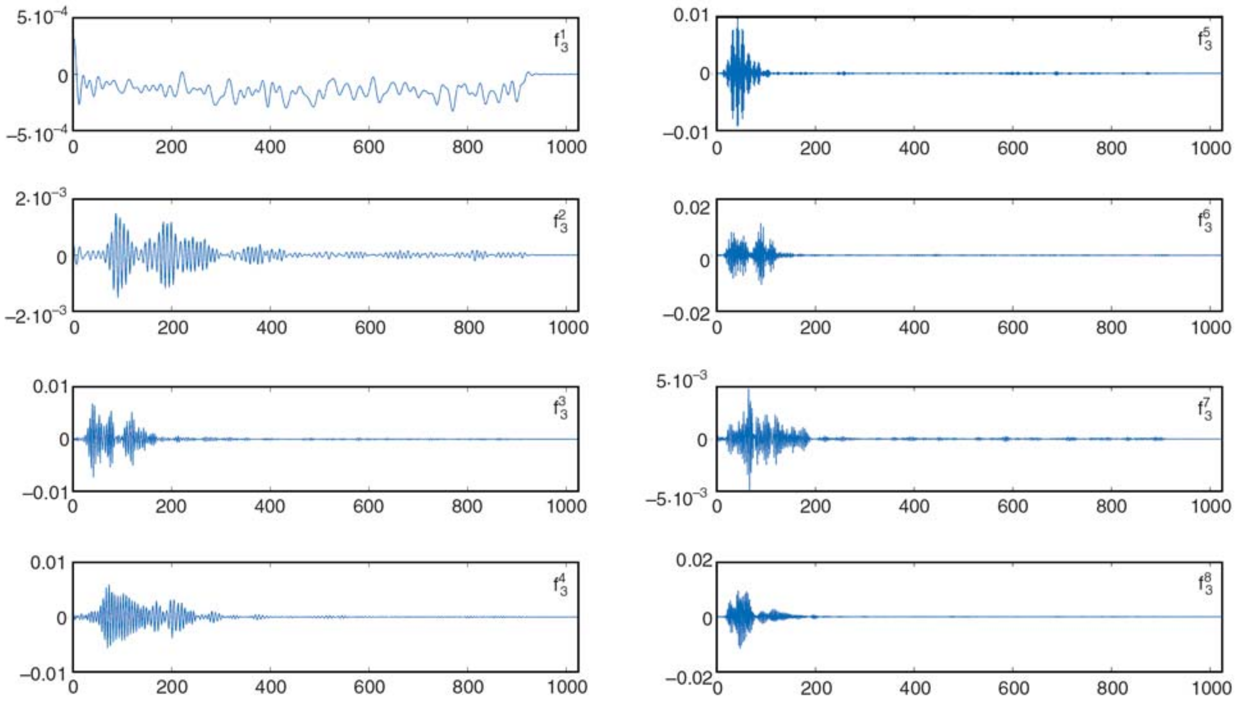

**Figure 6.** Three level wavelet packet decomposition of an AE signal for T3 (amplitude in [mV] vs. sample points)

the next plots. The full decomposition of each signal by the wavelet packet transform is carried out and all the components of the third level were only used to find the dominant energy levels. Figure 6 shows the three level wavelet packet decomposition of AE signals for specimen T3. Each component at level 3 represents a specific frequency range, and the frequency range increases with increasing the wavelet levels. There are eight components at third level whose frequency range is obtained from Equations (15) and (16). The FFT method is used to obtain the frequency content of the decomposed signals. Figure 7 is the frequency content of each component of decomposed signals that have been shown in Figure 6. From the graphs it is obvious that the frequency range of the decom-

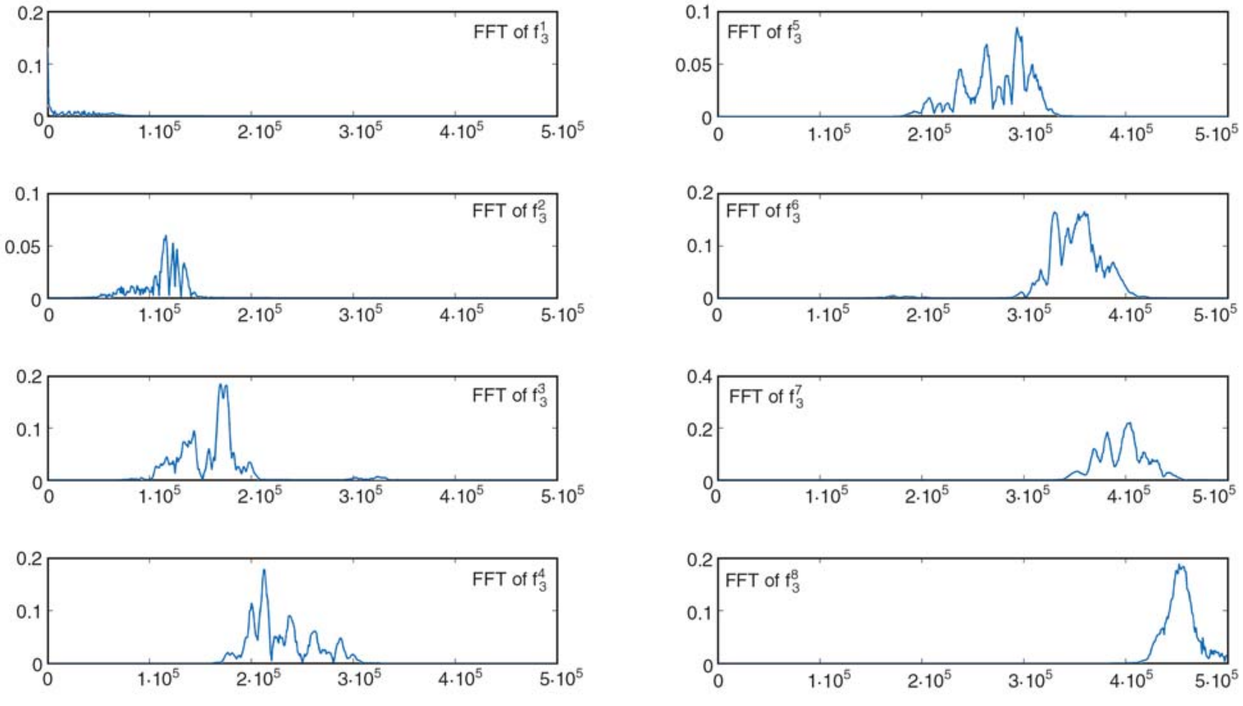

**Figure 7.** FFT of the decomposed components of level 3 (FFT amplitude [mV$^2$/Hz] vs. frequency [Hz])

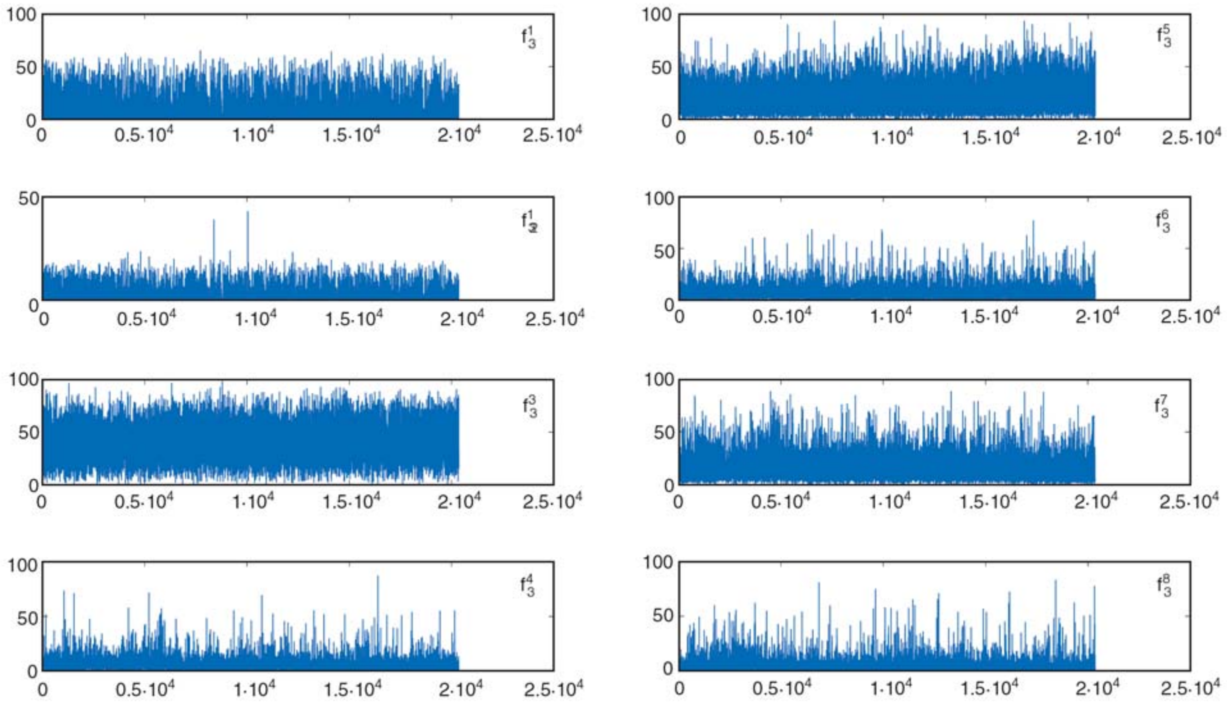

**Figure 8.** Energy percentage of each component of level 3 for T3 (energy [%] vs. waveform number)

posed components, increased from one component to another.

According to the Nyquist sampling theorem, the signal must be sampled at twice the highest frequency contained in the signal. Therefore, in this case, the sampling frequency set to 1 MHz and the transformed signals frequency must be up to 500 kHz. The frequency interval between the two adjacent components is 62.5 kHz, according to Equations (15) and (16).

From the methodology described in the previous section, after the decomposition of all AE signals, the energy percentage of the signal in each component is compared with the total energy of the AE

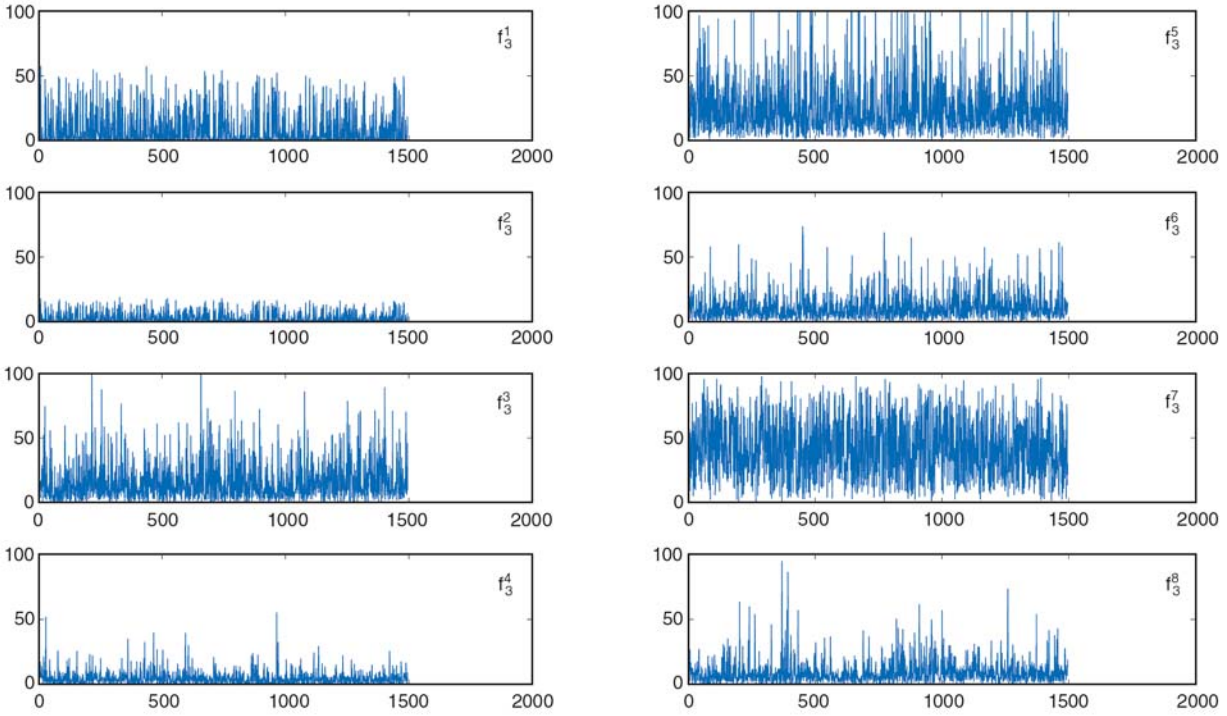

**Figure 9.** Energy percentage of each component of level 3 for T5 (energy [%] vs. waveform number)

signal that can be calculated based on Equations (17), (18) and (19). In Figures 8 and 9, the results of the calculation to find the energy distribution in each component, are obtained for specimens T3 and T5, respectively. In these figures, the vertical coordinate is the energy and the horizontal coordinate is the waveform number.

The variation of distribution is different from one component to another one. The greatest percentage of the energy is distributed in 3 components that called $f_3^3, f_3^5, f_3^7$. For interface T3 the highest energy is concentrated at component $f_3^3$ while for interface T5 the highest energy is related to component $f_3^7$. Obviously, at the same component for different interfaces, the energy distribution pattern is different. This difference could be directly related to different damage mechanisms during mode I delamination. It was concluded that there are two separate dominant damage mechanisms in interfaces T3 and T5. From Figure 7 the frequency range of three dominant components is obtainable: for component $f_3^3$ the frequency range is at 125–200 kHz, component $f_3^5$ at 250–310 kHz and component $f_3^7$ at 375–440 kHz, approximately. For interface T3 components $f_3^3, f_3^5$ are dominant between the three components while for interface T5 $f_3^7$ is dominant. Also, based on the energy distribution at each component, in this work we additionally calculated the average energy of each component. The results show that for interface T3, $f_3^3$ possesses about 40% of total energy, $f_3^5$ about 20% and $f_3^7$ 15% in average. These values for interface T5 are $f_3^3 = 15\%$, $f_3^5 = 25\%$ and $f_3^7 = 40\%$. Summary of wavelet packet results for dominant components are shown in Table 1.

To understand the relationship between dominant component frequency and failure mode, microscopic observation is considered, too. Damage mechanisms such as fiber/matrix debonding and matrix cracking have been observed by SEM microscope (Figure 10a). The break of fiber bridges is observed, especially in unidirectional composites with the weak fiber-matrix adhesion [23, 24]. Its AE energy contribution is negligible in mode I delamination propagation where the woven/woven mid plane is used. On the other hand for interface T3 only matrix cracking and debonding between fiber/ matrix are considered and a little fiber breakages have been observed. As observed from SEM results, matrix cracking and debonding are significant failure mechanisms during mode I delamination in the woven composites, while for interface T5 fiber breakage and debonding were significant too (Figure 10b). But what is the relation between three dominant components frequency range and SEM observation?

**Table 1.** Summary of wavelet packet analysis for dominant components

| Specimen | Energy percentage of dominant components [%] | Frequency range of dominant components [kHz] |
|---|---|---|
| T3 | $f_3^3 = 40$ | 125–250 |
| | $f_3^5 = 20$ | 250–310 |
| | $f_3^7 = 15$ | 375–440 |
| T5 | $f_3^3 = 15$ | 125–250 |
| | $f_3^5 = 25$ | 250–310 |
| | $f_3^7 = 40$ | 375–440 |

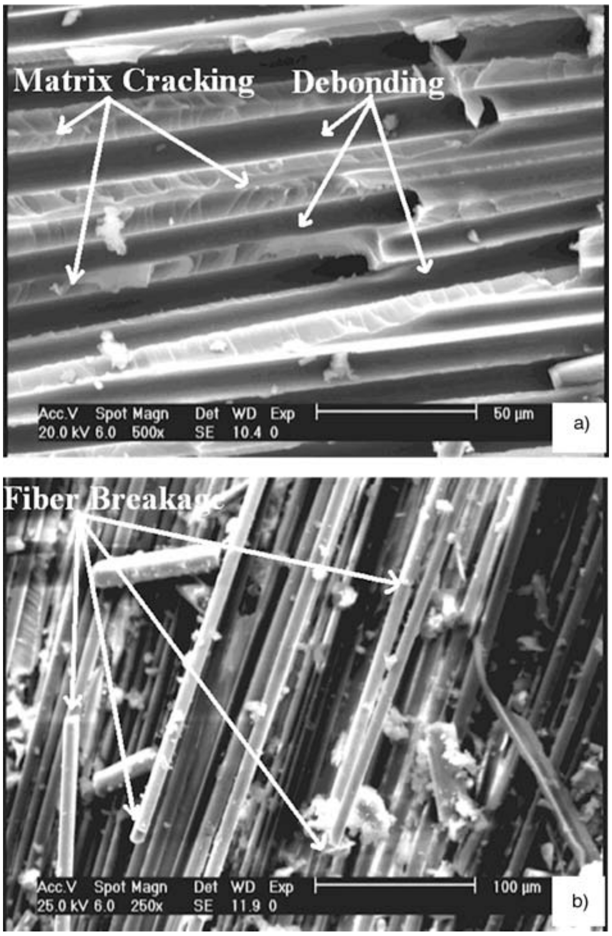

**Figure 10.** SEM observation of dominant failure mechanisms during mode I delamination: a) matrix cracking and debonding for T3 specimen, b) fiber breakage for T5 specimen

The possibility to distinguish between the matrix cracking and interface debonding relies on different visco-elastic relaxation processes near to the source itself [25]. Intrinsic frequencies $f_i$ and elastic acoustic velocities $c_i$ of the relaxation processes differ in the fiber, matrix and matrix/fiber interface because of the correlation with the relaxation times $\tau_i$, elastic module $E_i$ and densities $\rho_i$ according to Equation (20) [25]:

$$f_i \sim \frac{1}{\tau_i} \sim c_i \sim \sqrt{\frac{E_i}{\rho_i}} \tag{20}$$

Thus, the polyester-matrix cracking creates lower wide-band frequencies than the glass-fiber/matrix interface debonding.

From the above discussion it is concluded that component $f_3^3$ at low frequency (125–200 kHz) is associated with matrix cracking. Another dominant wavelet component at level 3, $f_3^5$ can be directly corresponded to the other damage mechanisms e.g. debonding between matrix and fiber where the frequency range is 250–310 kHz [13]. The above argument is consistent with the existing research results based on the AE frequency contents of signals [11–13]. Finally, the last one, that exists other source in the signal with high frequency (375–440 kHz) dominated by component, $f_3^7$, representing fiber breakage failure mode [13, 25]. Also the SEM observation is in agreement with these results as obtained from wavelet analysis.

In interface T5 fiber breakage was more significant and 40% of energy was distributed in fiber breakage range due to the existence of Fiber Bridge in unidirectional interface. But in woven interface, fiber length is not long enough to be bridged, so instead of fiber breakage, fiber debonding is dominant. However, debonding is detected for both of interfaces but the portion of energy for fiber breakage was higher for interface T5.

Consequently, the other components in wavelet analysis can be considered as a noise, fiber pull-out and sliding of fiber.

## 6. Conclusions

The objective of this study is to investigate the mode I delamination by AE technique and determine the relationship between AE results and damage mechanisms in mode I delamination. A wavelet packet transform methodology was established for the post-processing of the AE waveforms recorded during the testing of a composite material. Also, SEM observation of DCB specimens shows that the failure modes, such as matrix cracking, debonding and fiber breakage, were the sources of AE signals but which frequency range is in relation with these failure modes that is the objective that clarified by wavelet based method.

The component energy of a decomposed AE signal provides a comprehensive means of identifying AE sources. The energy concept shows different potential failure modes of a specimen by discriminating the energy quantity and frequency range.

As a result, from the energy concentration criterion, it was found that three dominant components at the frequency ranges of 125–200, 250–310 and 375–440 kHz are concerned with the matrix cracking, debonding and fiber breakage, respectively.

The energy pattern was different from one specimen to another one due to different damage mechanisms. This is the ability of wavelet analysis that can be used as an effective tool for monitoring and characterizing the failure modes especially in the composite materials.

## Acknowledgements

A part of this research is financially supported by the Pars Gas and Oil Company of Iran. The authors wish to thank the Department of Mechanical Engineering at Amirkabir University of Technology for providing the facilities to carrying out the tests.

## References

[1] ASTM D5528: Standard test method for mode I interlaminar fracture toughness of unidirectional fiber-reinforced polymer matrix composites (1994).

[2] Pappas Y. Z., Markopoulos Y. P., Kostopoulos V.: Failure mechanisms analysis of 2D carbon/carbon using acoustic emission monitoring. NDT&E International, **31**, 157–163 (1998).
DOI: 10.1016/S0963-8695(98)00002-4

[3] Velmurugan R., Solaimurugan S.: Improvements in mode I interlaminar fracture toughness and in-plane mechanical properties of stitched glass/polyester composites. Composites Science and Technology, **67**, 61–69 (2007).
DOI: 10.1016/j.compscitech.2006.03.032

[4] Benevolenski O. I., Karger-Kocsis J., Czigány T., Romhány G.: Mode I fracture resistance of glass fiber mat-reinforced polypropylene composites at various degree of consolidation. Composites Part A: Applied Science and Manufacturing, **34**, 267–273 (2003).
DOI: 10.1016/S1359-835X(02)00045-3

[5] Romhány G., Szebényi G.: Interlaminar crack propagation in MWCNT/fiber reinforced hybrid composites. Express Polymer Letters, **3**, 145–151 (2009). DOI: 10.3144/expresspolymlett.2009.19

[6] Benmedakhene S., Kenane M., Benzeggagh M. L.: Initiation and growth of delamination in glass/epoxy composites subjected to static and dynamic loading by acoustic emission monitoring. Composites Science and Technology, **59**, 201–208 (1999). DOI: 10.1016/S0266-3538(98)00063-3

[7] Godin N., Huguet S., Gaertner R.: Integration of the Kohonen's self-organising map and k-means algorithm for the segmentation of the AE data collected during tensile tests on cross-ply composites. NDT&E International, **38**, 299–309 (2005). DOI: 10.1016/j.ndteint.2004.09.006

[8] Philippidis T. P., Nikolaidis V. N., Anastassopoulos A. A.: Damage characterization of carbon/carbon laminates using neural network techniques on AE signals. NDT&E International, **31**, 329–340 (1998). DOI: 10.1016/S0963-8695(98)00015-2

[9] de Oliveira R., Marques A. T.: Health monitoring of FRP using acoustic emission and artificial neural networks. Computers and Structures, **86**, 367–373 (2008). DOI: 10.1016/j.compstruc.2007.02.015

[10] Siron O., Chollon G., Tsuda H., Yamauchi H., Maeda K., Kosaka K.: Microstructural and mechanical properties of filler-added coal-tar pitch-based C/C composites: The damage and fracture process in correlation with AE waveform parameters. Carbon, **39**, 2065–2075 (2001). DOI: 10.1016/S0008-6223(99)00270-5

[11] Ramirez-Jimenez C. R., Papadakis N., Reynolds N., Gan T. H., Purnell P., Pharaoh M.: Identification of failure modes in glass/polypropylene composites by means of the primary frequency content of the acoustic emission event. Composites Science and Technology, **64**, 1819–1827 (2004). DOI: 10.1016/j.compscitech.2004.01.008

[12] Haselbach W., Lauke B.: Acoustic emission of debonding between fibre and matrix to evaluate local adhesion. Composites Science and Technology, **63**, 2155–2162 (2003). DOI: 10.1016/S0266-3538(03)00193-3

[13] Ni Q-Q., Iwamoto M.: Wavelet transform of acoustic emission signals in failure of model composites. Engineering Fracture Mechanic, **69**, 717–728 (2002). DOI: 10.1016/S0013-7944(01)00105-9

[14] Qi G., Barhorst A., Hashemi J., Kamala G.: Discrete wavelet decomposition of acoustic emission signals from carbon-fiber-reinforced composites. Composites Science and Technology, **57**, 389–403 (1997). DOI: 10.1016/S0266-3538(96)00157-1

[15] Qi G.: Wavelet-based AE characterization of composite materials. NDT&E International, **33**, 133–144 (2000). DOI: 10.1016/S0963-8695(99)00037-7

[16] Loutas T. H., Kostopoulos V., Ramirez-Jimenez C., Pharaoh M.: Damage evolution in center-holed glass/polyester composites under quasi-static loading using time/frequency analysis of acoustic emission monitored waveforms. Composites Science and Technology, **66**, 1366–1375 (2006). DOI: 10.1016/j.compscitech.2005.09.011

[17] Velayudham A., Krishnamurthy R., Soundarapandian T.: Acoustic emission based drill condition monitoring during drilling of glass/phenolic polymeric composite using wavelet packet transform. Materials Science and Engineering: Part A, **412**, 141–145 (2005). DOI: 10.1016/j.msea.2005.08.036

[18] Rao R. M., Bopardikar A. S.: Wavelet transforms introduction to theory and applications. Addison-Wesley, Boston (1998).

[19] Soman K. P., Ramachandran K. I.: Insight into wavelets from theory to practice. Prentice-Hall, New Delhi (2004).

[20] Wojtaszczyk P.: A mathematical introduction to wavelets. Cambridge University Press, Cambridge (1997).

[21] Walnut D. F.: An introduction to wavelet analysis. Birkhäuser, Boston (2002).

[22] Coifman R. R., Wickerhauser M. V.: Entropy-based algorithms for best basis selection. IEEE Transactions on Information Theory, **38**, 713–718 (1992). DOI: 10.1109/18.119732

[23] Brunner A. J., Blackman B. R. K., Williams J. G.: Calculating a damage parameter and bridging stress from GIC delamination tests on fibre composites. Composites Science and Technology, **66**, 785–795 (2006). DOI: 10.1016/j.compscitech.2004.12.040

[24] de Moraisa A. B., Marques A. T.: Mode I interlaminar fracture of carbon/epoxy multidirectional laminates. Composites Science and Technology, **64**, 2261–2270 (2004). DOI: 10.1016/j.compscitech.2004.03.001

[25] Bohse J. Acoustic emission characteristics of microfailure processes in polymer blends and composites. Composites Science and Technology, **60**, 1213–1226 (2000). DOI: 10.1016/S0266-3538(00)00060-9

*eXPRESS Polymer Letters Vol.3, No.12 (2009) 814–820*
*Available online at www.expresspolymlett.com*
*DOI: 10.3144/expresspolymlett.2009.100*

# Properties of solvent-borne acrylic pressure-sensitive adhesives synthesized by a simple approach

*X. Jin*[1], *Y. P. Bai*[1], *L. Shao*[1*], *B. H. Yang*[1,2], *Y. P. Tang*[1]

[1]Department of Polymer Science and Engineering, School of Chemical Engineering and Technology, Harbin Institute of Technology, 150001 Harbin, P.R. China
[2]Northwest Institute of Nuclear Technology, Shanxi Province, 710024 Xi'an, P.R. China

*Received 2 August 2009; accepted in revised form 30 September 2009*

**Abstract.** Acrylic polymers are widely used for fabricating pressure-sensitive adhesives (PSAs) with the inherent unique advantages of transparency and superior intrinsic adhesive properties over other polymer-based adhesives. In this study, we have developed and evaluated a method of obtaining by radical copolymerization PSAs for liquid crystalline (LCD) applications. Various factors including the amount of monomers, amount of cross-linker, coating weight, dwell time and thermal treatment are investigated for further optimizing the properties of acrylic polymer based PSAs to meet the emerging strict requirements for practical uses related mainly to holding powder and peel strength. The results illustrate that novel cross-linking reagents coupled with the thermal treatment at 70°C can make the resultant PSAs with the improved adhesive properties. The coating weight variation from 10 to 40 g/m$^2$ can significantly enhance the peel strength from 4.0 g/25 mm to 12.5 g/25 mm with about 310% increment. If the dwell time of PSAs with cross-linking reagent is more than 10 hrs, the peel strength can be reduced down to a suitable value to meet the criterion for use. Therefore, acrylic PSAs with peel strength less than 20 g/25 mm and holding power above 120 hrs were successfully synthesized by elaborately designing the reaction system, which are practically applicable for advanced industrial applications.

***Keywords:*** *adhesion, radical polymerization, cross-linking, acrylic polymer, peel strength*

## 1. Introduction

With the rapid development of large-format models in liquid crystalline displays (LCD) and the increasing demands on screen-surface functions such as brightness control and shielding ability, various types of optical films have been specially designed and applied, which include the polarizing plate or brightness enhancing film for LCD usage [1]. Before the film assembly on LCD, other processes including punching, transporting and inspecting are necessary. Thus, the application of a protective film is compulsory to protect the surface of the optical films from contaminants or scratching [2]. A sketch of a polarizing plate with a protective film is demonstrated in Figure 1. The substrates of the protective film are typically fabricated using polyethylene (PE) or polyethylene terephthalate (PET) with pressure sensitive adhesives (PSAs) coated on one side. PSAs are viscoelastic materials that can adhere to various substrates upon application of light contact pressure in short contact time. The advantages of PSAs include that the

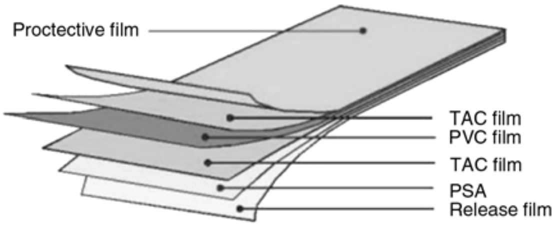

**Figure 1.** A polarizing plate with a protective film

---

[*]Corresponding author, e-mail: odysseynus@hotmail.com

resistance of PSAs to debonding is reasonably moderate and the substrates can be delaminated by a suitable force without destroying the targeted laminate components for most of cases. However, for the high value applications such as the application for LCD protective film, the strict requirements for PSAs must be met which include the appropriate peel strength, defect-free, and anti-curvature so that the optical films can cope with the up-to-date technical trends for high quality products.

It is well known that various materials can be used as adhesives [3–5], among which acrylic polymers are the most popular ones for PSA applications because of the inherent unique properties [6]. Acrylic PSAs are transparent, colorless, anti-aging against solar radiation and resistant to oxidation [7]. In addition, PSAs based on acrylic polymers also exhibit intrinsic adhesive properties superior to most of other polymers. Acrylic PSAs, generally borne in an organic solvent, must possess correspondingly suitable 180° peel strength, high shear strength and appropriate tack [8–10] for optical film applications. The adhesive properties of acrylic PSAs are critically determined by the monomer compositions, the initiators, the cross-linking agents and the tackifiers of acrylic PSAs. To the best of our knowledge, the PSAs used as the surface-protective film for optical film applications have been only reported in some patents. For examples, Tomita [1] has fabricated PSAs comprising the ingredients of: (A) a (meth)acrylic copolymer obtained by copolymerizing 80 to 99 wt% alkyl (meth)acrylate; (B) an isocyanate crosslinking agent. The synthesized PSAs demonstrated a peel force of 20 gf/inch. Niino *et al.* [2] have fabricated a protective tape used as optical membranes which demonstrated a low adhesive property. However, no detailed descriptions on PSAs used for the surface-protective film in optical film have been reported in the patents. Considering the importance of this emerging and promising field for PSA applications, a practical study related to the development of the-state-of-the-art materials for such applications should be carried out.

In this study, a simple, practical method of obtaining PSAs for LCD-applications in particular with the films by radical copolymerization of 2-ethylhexyl acrylate (2-EHA), methyl methacrylate (MMA) and acrylic acid (AA) in a typical organic solvent of ethyl acetate (EA) are investigated. The effects of copolymer composition, cross-linking agent content, coating weight and dwell time on adhesive-cohesive characteristics of synthesized PSAs are studied systematically.

## 2. Experimental

### 2.1. Materials

2-EHA, MMA, AA and EA were purchased from Guoyao Chemical Agent Co. Ltd. (Shanghai, China). Benzoylperoxide (BPO) was supplied by Yixing No. 2 Chemical Agent Co. Ltd (Wuxi, China). Cross-linking agents: SC-200 (containing aziridine groups) was obtained from Shanghai Secure Trading Co. Ltd.. All the chemicals were of analytical grade and used without further purification.

### 2.2. Preparation of acrylic polymers

A solution polymerization technique was applied for PSAs synthesis using BPO as a free radical initiator. The PSAs were synthesized with 50~60 parts of 2-EHA, 50~40 parts of MMA, 2 parts of AA, and 100 parts of EA, along with 0.3 part BPO and the properties and functions of monomers used in this study are listed in Table 1. Monomers (2-EHA, MMA, AA) with the predetermined composition were dissolved in EA solvent and placed in a four necked flask equipped with an overhead stirrer, a condenser, a thermometer and an inlet to purge nitrogen gas (for supplying inert reaction environment). Oxygen was eliminated by purging purified nitrogen gas for 20 minutes before initiators were added into the flask. Under the constant temperature maintained at 80°C, the reaction was continuously carried out for 10 hrs with consistent stirring. The chemical reaction is shown in Figure 2

**Table 1.** Selected monomers

| Monomer | $T_g$ [°C] | Group | Function |
|---|---|---|---|
| 2-EHA | –70 | Tackifying monomer | Provide a certain adhesion |
| MMA | 105 | Hardening monomer | Provide a higher cohesion |
| AA | 106 | Functional groups containing monomer | Provide active cross-linking centers for the later crosss-linking reaction |

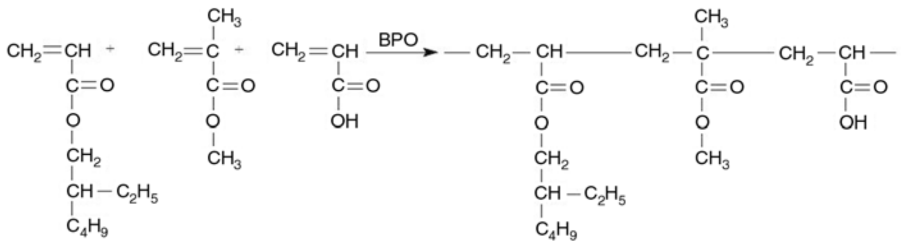

**Figure 2.** Synthesis reaction of PSA copolymers

**Table 2.** Component, viscosity and solid content of synthesized PSAs

| PSA/ No. | Monomers (part) | | | η [mPa·s] | S.C. [%] |
|---|---|---|---|---|---|
| | 2-EHA | MMA | AA | | |
| 1 | 60.0 | 40.0 | 2 | 3832 | 48.1 |
| 2 | 57.5 | 42.5 | 2 | 4108 | 50.3 |
| 3 | 55.0 | 45.0 | 2 | 3910 | 46.7 |
| 4 | 52.5 | 47.5 | 2 | 4214 | 53.3 |
| 5 | 50.0 | 50.0 | 2 | 4048 | 47.9 |

and the properties of synthesized PSAs according to different compositions were shown in Table 2.

### 2.3. Preparation of PSA tapes

Cross-linking reagents were diluted to 10 wt% concentration in EA which was added into the acrylic copolymer solution (about 50% solid content) with high speed stirring for mixing about 20 minutes. The resultant solution was further diluted to a desired concentration (about 30% by weight) to meet the requirement of coating on a PET film. After being dried at 120°C for 3 minutes, PSA tapes with coating weight of 30 g/m$^2$ were ready for characterizations. And the purpose of the 3 minutes drying process is to eliminate the solvent within the PSA and to initiate the cross-linking reaction, in general, to form the product PSA tape.

### 2.4. 180° Peel strength test

Strips of PSA tape samples (25 mm×250 mm) were attached to the surfaces of stainless-steel test panel by rolling twice with a 2 kg rubber roller at a speed of 10 mm per second. The pressed PSA tapes were kept for 20 min at 23°C with 50% relative humidity. 180° peel strength was measured with a peeling speed of 300 mm/min by using an Adhesion/Release Tester AR-1000 (ChemInstrument, USA). The average peel force measured during the entire peeling process was recorded.

### 2.5. Holding power test

A square of PSA coated tape, 25 mm×25 mm, was tightly contact with the surface of the testing plate. Roll twice in each direction with a 2 kg rubber roller at a speed of 10 mm per second. Place the testing plate into the rack of jig and attach the 1 kg weight to the free end of the testing strip after storing for 20 minutes at 23°C with 50% relative humidity. Holding power was expressed as the time taken for the strips to shear from the test plate.

## 3. Results and discussion

### 3.1. Influence of MMA content on properties of PSAs

The main reason that monomer of MMA is used to modify the cohesive strength of PSAs is due to the inherent high $T_g$ of MMA monomers as Table 1 shown [11]. After the comprehensive investigations on the composition during the radical polymerization, the effect of MMA content on the peel strength is illustrated in Figure 3. When the MMA content increases from 40 to 50%, the holding power of PSAs correspondingly increases from around 8 to 36 hrs and the peel strength decreases from 90 g/25 mm to 10 g/25 mm. Therefore, the increment in the MMA content can significantly

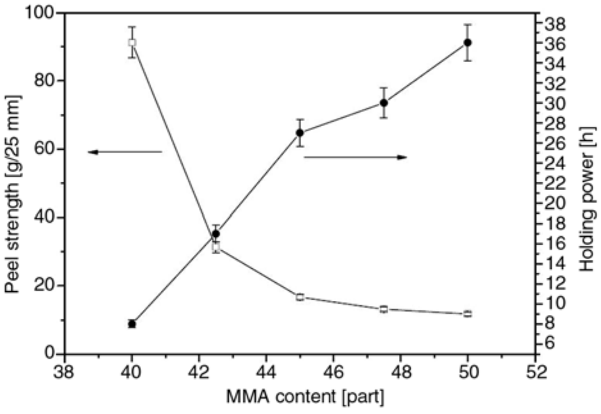

**Figure 3.** Influence of MMA content on peel strength and holding power

enhance the holding power of PSAs and decrease the peel strength of PSAs. Typically, MMA provides the cohesion properties and 2-EHA contributes to adhesion properties of PSAs. The content of 2-EHA decreases with the MMA content which results in the enhanced holding power and the weaken peel strength. However, when the MMA content exceeds 45 part (to 50 part), the decrement of peel strength is not significantly obvious (from around 18 g/25 mm to 10 g/25 mm). Since the purpose of this study is to prepare PSAs with the peel strength less than 20 g/25 mm which can meet the industrial requirements, PSAs with 45 part MMA is enough for peel strength requirements and selected for the following study.

### 3.2. Influence of cross-linking reagents on properties of PSAs

Various chemical compounds [1, 12, 13] including multifunctional isocyanates, multifunctional ethyleneimines and epoxy resins, can be utilized to cross-link PSAs for the manipulation of resultant PSA properties. In this study, cross-linking reagents of SC-200 are specially utilized to achieve high holding power and good heat resistant property. The effects of SC-200 content on the properties of PSAs with or without thermal treatment are demonstrated in Figure 4. The holding power for all PSAs (with or without thermal treatment) containing cross-linking reagents above 0.25 part was enhanced up to above 120 h. For the samples without thermal treatment, the increase of cross-linking reagent content from 0.25 to 1.0 part can decrease the peel strength from 16.7 g/25 mm to 8.3 g/25 mm. To illustrate the reaction mechanism, the chemical structure of SC-200 is shown in Figure 5, in which $R_1$ is an $n$-valent organic or inorganic group and $R_2$ is –H or $-CH_3$. The cross-linking reaction between original PSAs and SC-200 is mainly based on the carboxyl groups offered by the AA functional component within PSA copolymers and the aziridine groups provided by SC-200. During the cross-linking reaction, the carboxyl groups act as proton donors supplying protons to attack the nitrogen atoms for protonation and cause the opening of the enimine rings. Then, a carbocation is generated as an intermediate which is free of the counterion $COO^-$. Based on the above analysis, the sketch of the ring-opening reaction is illustrated in Figure 6, while the mechanism of the entire cross-linking reaction is demonstrated in Figure 7.

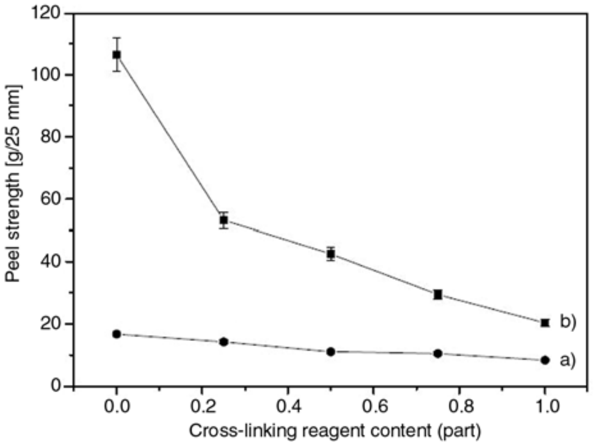

**Figure 4.** Influence of the amount of cross-linker on peel strength of (a) without high temperature treatment and (b) treated at 70°C for 24 h

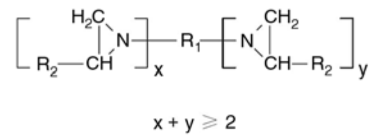

**Figure 5.** Structure of Cross-linker SC-200

As previously mentioned, cross-linking process has been considered as an important factor for the final properties of PSAs for practical applications [14, 15]. The cross-linking reactions drastically inhibit the mobility of polymer molecules by forming chemical bonds among the chains of PSAs and correspondingly increase the molecular weight of polymers. After that, the cross-linked PSAs can not melt any more because of the cross-linked network formed. However, the cross-linked PSAs can become soft at a high temperature. Besides, the cross-linked PSAs undergo decomposition above certain temperatures. Owing to the formation of chemical bonds, an increase in cohesion can be obtained during the curing of the PSA coating layer

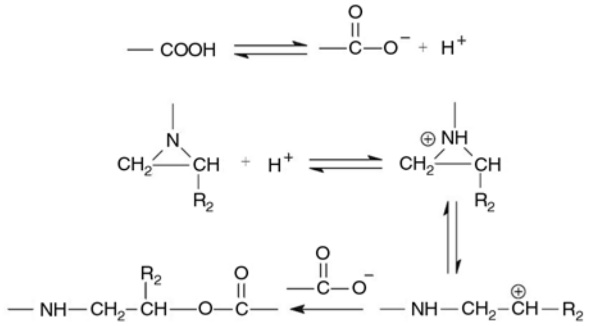

**Figure 6.** Sketch of the ring-opening reaction

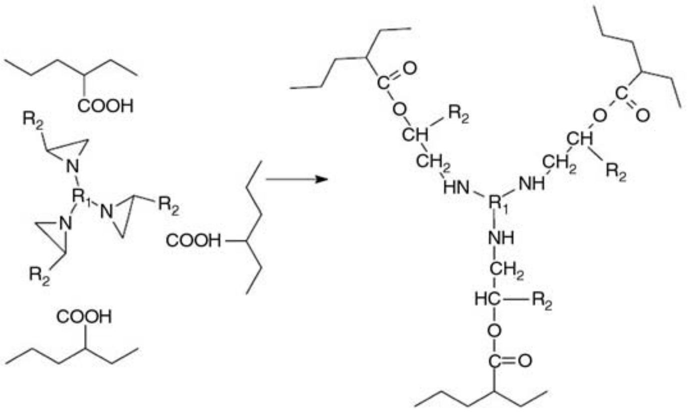

**Figure 7.** Cross-linking of PSA initiated by SC-200

in the drying step, in which the cross-linking reaction occurs [16, 17].

Figure 4 also illustrates the influences of cross-linking reagents on the heat resistance of PSA. After the PSA strips adhered completely on the stainless-steel plates, the specimens were transferred to an oven maintained at 70°C. The high temperature treatment persisted for 24 h. After the specimens cooled to room temperature, peel strength testing was performed to characterize the heat resistant performance of PSAs. Interestingly, after high temperature treatment, the peel strength of PSAs increases significantly. For example, the peel strength of PSA without cross-linking reagent increases about 6 times after 70°C thermal treatment. In addition, cohesive failure shows up during the peel strength test. Gratefully, with the addition of cross-linker, the increment of peel strength decreased which is much suitable for PSA applications.

### 3.3. Influence of coating weight on peel strength

The following investigations are conducted in order to study the influence of the coating weight of PSAs on peel strength. The PSA containing 45 parts MMA is mixed with 0.5 part cross-linker, and then is coated on a piece of PET film. The increase of coating weight from 10 to 40 g/m$^2$ enhances the peel strength from 4.0 g/25 mm to 12.5 g/25 mm which indicates the significant increment of peel strength about 310% (as Figure 8 shown), while the holding power property of each specimen is still up to 120 hrs. The isolation of a PSA tape from a substrate is concomitant with a certain number of non-equilibrium and dissipative processes which include large bulk deformations [18]. In some cases, these deformations involve cavitations and fibrillations, which both significantly contribute to the energy of separation [19]. The increase of the coating weight has a noticeable effect on intensifying the deformations, thus more dissipative the PSA tape exhibits. As a result, the larger peel strength is achieved with the increase of coating weight.

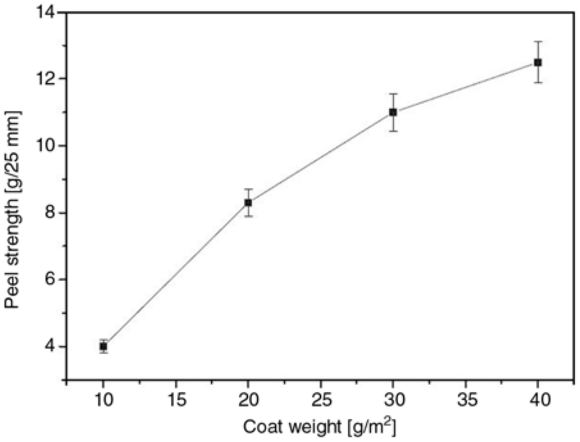

**Figure 8.** Influence of coating weight on peel strength

### 3.4. Dwell time effect on properties of PSAs

Dwell effect of PSAs with cross-linking reagent on peel strength is characterized further for practical applications. The peel strength of nascent PSAs declined gradually with the dwell time. The decreasing trend is not so obvious after 10 hrs since the PSA tapes are prepared (as Figure 9 shown). This phenomenon indicates that an acceptable cross-linking degree in PSAs can be achieved after 10 hrs dwell of nascent PSAs.

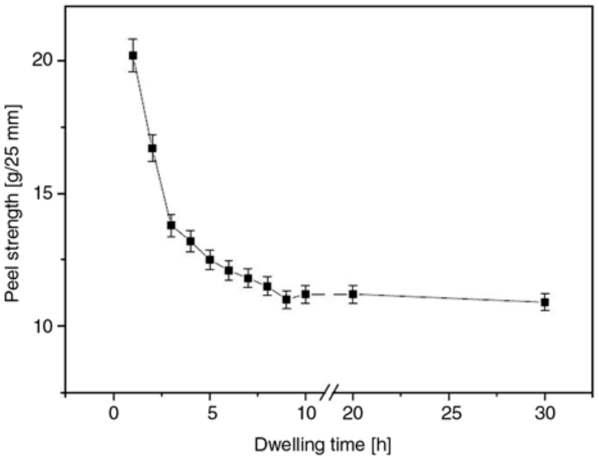

**Figure 9.** The influence of dwell time on peel strength

## 4. Conclusions

In summary, PSAs with properties of peel strength no more than 20 g/25 mm and holding power above 120 hrs are successfully synthesized with a simple radical polymerization method. PSA tapes possessing targeted properties can be fabricated to meet the special requirements for industrial usages. The increase of MMA content decreases the peel strength and improves the holding power. The incorporation of cross-linking reagents of SC-200 is crucial for improving the adhesive properties of acrylic PSAs. The increase of cross-linking reagents decreases the peel strength, improves the holding power (>120 hrs), and enhances the heat resistance. Besides, the increase of coating weight enhances the peel strength of PSAs. Extending the dwelling time of PSA tapes containing cross-linking reagent has a positive effect on decreasing the peel strength.

## Acknowledgements

Dr. Shao thanks for the support from the Specialized Research Fund for the Doctoral Program of Higher Education (20070213004), Harbin Science and Technology Innovation Talent Funds (contract grant number: 2006RFLXG015) and the Scientific Research Foundation for the Returned Oversea Chinese Scholars, State Education Ministry.

## References

[1] Tomita K.: Pressure-sensitive adhesive for surface-protective film and surface-protective film. WO/2005/000989 (2005).

[2] Niino T., Imono S., Okumura K., Sano K.: Protective tape used for optical membrane. US Patent 7270877 B2, USA (2007).

[3] Wei S-Q., Bai Y-P., Shao L.: A novel approach to graft acrylates onto commercial silicones for release film fabrications by two-step emulsion synthesis. European Polymer Journal, **44**, 2728–2736 (2008).
DOI: 10.1016/j.eurpolymj.2008.04.025

[4] Patel H. J., Patel M. G., Patel A. K., Patel K. H., Patel R. M.: Synthesis, characterization and antimicrobial activity of important heterocyclic acrylic copolymers. Express Polymer Letters, **2**, 727–734 (2008).
DOI: 10.3144/expresspolymlett.2008.86

[5] Jeusette M., Peeterbroeck S., Simal F., Cossement D., Roose P., Leclere Ph., Dubois Ph., Hecq M., Lazzaroni R.: Microscopic morphology of blends between a new ‘all-acrylate’ radial block copolymer and a rosin ester resin for pressure sensitive adhesives. European Polymer Journal, **44**, 3931–3940 (2008).
DOI: 10.1016/j.eurpolymj.2008.09.003

[6] Czech Z., Butwin A., Herko E., Hefczyc B., Zawadiak J.: Novel azo-peresters radical initiators used for the synthesis of acrylic pressure-sensitive adhesives. Express Polymer Letters, **2**, 277–283 (2008).
DOI: 10.3144/expresspolymlett.2008.33

[7] Taghizadeh S. M., Mirzadeh H., Barikani M., Yousefi M.: Miscibility and tack of blends of poly(vinylpyrrolidone)/acrylic pressure-sensitive adhesive. International Journal of Adhesion and Adhesives, **29**, 302–308 (2009).
DOI: 10.1016/j.ijadhadh.2008.06.006

[8] Xu G. Z. H., Dong J. P., Zhang J. G., Severtson S. J., Houtman C. J., Gwin L. E.: Characterizing the distribution of nonylphenol ethoxylate surfactants in water-based pressure-sensitive adhesive films using atomic-force confocal Raman microscopy. The Journal of Physical Chemistry B, **112**, 11907–11914 (2008).

[9] Taghizadeh S. M., Mirzadeh H., Barikani M., Yousefi M.: The effect of poly(vinylpyrrolidone) concentration on peel strength of acrylic/PVP pressure sensitive adhesive blends. Iranian Polymer Journal, **16**, 279–285 (2007).

[10] Bai Y-P., Zhao L., Shao L.: Hybrid emulsifiers enhancing polymerization stabilities and properties of pressure sensitive adhesives. Journal of Applied Polymer Science, **115**, 1125–1130 (2009).
DOI: 10.1002/app.31211

[11] Yang Y. K., Lv F. T.: Technical handbook of PSA products. Chemical Industry Press, Beijing (2004).

[12] Gardeski T. F.: A high performance epoxy based coverlay and bond ply adhesive with heat activated cure mechanism. European Patent 0436745A1, EU (1989).

[13] Saiki N., Yamazaki O., Ebe K.: UV/heat dual-durable adhesive tapes for fabricating stacked packages of semiconductors. Journal of Applied Polymer Science, **108**, 1178–1183 (2008).
DOI: 10.1002/app.27663

[14] Yamamoto M., Nakano F., Doi T., Moroishi Y.: Synthesis and PSA performance study for novel acrylic and butyl acrylate block copolymers. International Journal of Adhesion and Adhesives, **22**, 37–40 (2002). DOI: 10.1016/S0143-7496(01)00034-3

[15] Moon J. H., Shul Y. G., Hong S. Y., Choi Y. S., Kim H. T.: A study on UV-curable adhesives for optical pick-up: I. Photo-initiator effects. International Journal of Adhesion and Adhesives, **25**, 301–312 (2005). DOI: 10.1016/j.ijadhadh.2004.09.003

[16] Verdier C., Piau J-M., Benyahia L.: Peeling of acrylic pressure sensitive adhesives: Cross-linked versus uncross-linked adhesives. Journal of Adhesion, **68**, 93–116 (1998). DOI: 10.1080/00218469808029581

[17] Brostow W.: Time-stress correspondence in viscoelastic materials: An equation for the stress and temperature shift factor. Material Research Innovations, **3**, 218–225 (2000). DOI: 10.1007/s100190000054

[18] Wang T., Lei C-H., Dalton A. B., Creton C., Lin Y., Fernando K. A. S., Sun Y-P., Manea M., Asua J. M., Keddie J. L.: Waterborne, nanocomposite pressure-sensitive adhesives with high tack energy, optical transparency, and electrical conductivity. Advanced Materials, **18**, 2730–2734 (2006). DOI: 10.1002/adma.200601335

[19] Zosel A.: The effect of fibrillation on the tack of pressure sensitive adhesives. International Journal of Adhesion and Adhesives, **18**, 265–271 (1998). DOI: 10.1016/S0143-7496(98)80060-2

*eXPRESS Polymer Letters Vol.3, No.12 (2009) 821–831*
*Available online at www.expresspolymlett.com*
*DOI: 10.3144/expresspolymlett.2009.101*

# Properties and structure of SPEEK proton exchange membrane doped with nanometer $CeO_2$ and treated with high magnetic field

*J. Y. Tong*[1,2], *Q. Guo*[1*], *X. X. Wang*[1]

[1]School of Materials Science and Engineering, Shanghai University, Shanghai, 201800, China
[2]School of Wenling, Zhejiang TV University, Wenling, 317500, China

*Received 18 July 2009; accepted in revised form 1 October 2009*

**Abstract.** The membranes of sulfonated polyetheretherketone(SPEEK) doped with rare earth metal oxide nanometer cerium oxide ($CeO_2$) were prepared for direct methanol fuel cell (DMFC) application, which was treated by parallel or perpendicular high magnetic field of 6 Teslas (T) at 100°C. The proton conductivity of membrane specimens increased with temperature raised from 20 to 60°C and decreased with increasing $CeO_2$ contents. The proton conductivity of membrane specimens under treatment with high magnetic field was better than that without treatment. The membrane specimens treated with perpendicular magnetic field demonstrated better proton conductivity than those treated with parallel magnetic field. The methanol permeation coefficient of membrane specimens decreased with increasing $CeO_2$ contents and furthermore reduced by about 20% after treated with perpendicular high magnetic field. The water uptake of membrane specimens decreased with $CeO_2$ doping, but would not be influenced by the magnetic field. Fourier transform infrared spectroscopy (FTIR) and small-angle X-ray scattering (SAXS) revealed certain reaction between oxygen anion in sulfonic groups and cerium cation in the $CeO_2$ which dispersed evenly in the membranes but formed small conglomerates as shown by the atomic force microscopy (AFM) images. X-ray diffraction (XRD) proved the stability of the crystal structure of the nanometer $CeO_2$ in polymer membranes, indicating that the reaction occurred only at the interface between SPEEK resin and $CeO_2$ particles.

***Keywords:*** *polymer membranes, SPEEK/$CeO_2$, high magnetic field, methanol permeability*

## 1. Introduction

Sulfonated polyetheretherketone (SPEEK) has attracted considerable attention as proton exchange membrane (PEMs) for direct methanol fuel cell (DMFC) applications, since it possesses good thermal stability and mechanical property [1–4]. However, increasing degrees of sulfonation (DS) of SPEEK materials have a negative effect on the proton conductivity and methanol permeability of DMFC. The PEMs with high DS have good proton conductivity, and meanwhile they have high methanol permeability [4–6]. Therefore, the comprehensive excellent properties of PEMs can not be obtained at the same time by adjusting DS. Nunes *et al.* [7] claimed a remarkable reduction of the methanol permeability with $SiO_2$, $TiO_2$ or $ZrO_2$ modification in SPEEK. Siliva *et al.* [8] pronounced a reduction of the methanol permeability and proton conductivity via the modification with $ZrO_2$. Chang *et al.* [9] also published a decreasing methanol cross-over by embedding laponite and montmorillonite into SPEEK matrix. However, the proton conductivities of composite membranes decreased somewhat. Good results have been

---

[*]Corresponding author, e-mail: guoq@shu.edu.cn

obtained by introducing $CeO_2$ catalyst in proton exchange membrane fuel cell (PEMFC), the performance of the cathode in cell was also improved [10] and CO was removed from $H_2$ stream without oxidizing excess $H_2$ on the anode [11]. Nobody has reported the PEMs based on SPEEK doped with nanometer $CeO_2$ so far.

The high magnetic field can transfer the energy to the material at the atomic-scale without contact and does not change its components. Brijmohan and Shaw [12] has reported that SPEEK-based membranes doped with *y*-$Fe_2O_3$ exhibited better properties for application in PEMs after 0.1 Tesla (T) magnetic field treatment. To our knowledge, however, the use of high magnetic field has not been reported for PEMs in DMFC before. In this paper, polymer membranes were prepared by introducing nanometer $CeO_2$ in SPEEK, and then treated by high magnetic field parallel or perpendicular to the surface of the membrane, applied for one hour at 100°C. The properties and structure of the polymer membranes were investigated as well as their relative mechanisms.

## 2. Experimental

### 2.1. Membrane preparation and high magnetic field treatments

Poly(etheretherketone) (PEEK) was obtained from Jilin University(Jilin, China), in the form of particle. It was dried in a vacuum oven at 100°C overnight. Thereafter, 20 g of polymers were dissolved in 1 l concentrated sulfuric acid (95–98%) (Sinopharm Chemical Reagent Co., Ltd, Shanghai, China) and vigorously stirred at room temperature for 68 hours. Then, the polymer solution was gradually precipitated into ice-cold water under mechanical agitation. The polymer suspension was left to settle overnight. The polymer precipitate was filtered, washed several times with deionized water until pH 7 was achieved and dried at 60°C for 24 h, further dried at 100°C for 2 h. The DS of SPEEK, 48.3%, was determined by titration [9]. After SPEEK was triturated, it was dissolved in dimethylacetamide (DMAc) offered by Sinopharm Chemical Reagent Co., LtdS(Shanghai, China), to make a 10 wt% solution. The mixture was doped with a certain amount of $CeO_2$ with a particle size of 40–50 nm, offered by Shanghai Huaming Gaona Rare Earth New Materials Co., Ltd (Shanghai, China), and stirred at room temperature for 4 h, afterward at 75°C for 6 h. The pure SPEEK and SPEEK/$CeO_2$ polymer membranes were obtained by casting their viscous solution onto a glass plate. The glass plate was then dried at 60°C for 48 h to remove the solvents, annealed at 120°C for 4 h. The thickness of the dried membranes was about 100 µm.

The membranes were placed in a sample cabin of 6T superconducting magnet, Oxford Instruments (Oxford, UK), at 100°C for 1 h. The magnetic induction lines were perpendicular or parallel to the membrane surface in Figure 1a or 1b, and described with letter *E* or *A* in designation of membrane specimens in Table 1, respectively.

Table 1 shows the designation of membrane specimens, where UNT refers to membranes untreated with high magnetic field and MT denotes high magnetic field treatment. MTA and MTE represent the membranes treated with parallel and perpendicular magnetic field, respectively. The number denotes the mass percent of doped $CeO_2$ particles.

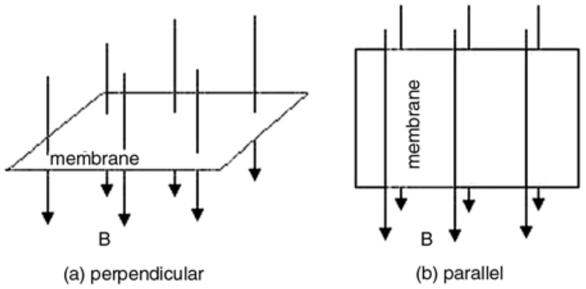

**Figure 1.** Diagram of magnetic vector with surface of membrane specimen (a) perpendicular or (b) parallel

**Table 1.** Designation of membrane specimens

| $CeO_2$ content [wt%] | Untreated with magnetic field (UNT) | Magnetic field treatment(MT) | |
|---|---|---|---|
| | | Perpendicular (E) | Parallel (A) |
| 0 | UNT-0 | MTE-0 | MTA-0 |
| 2 | UNT-2 | MTE-2 | MTA-2 |
| 5 | UNT-5 | MTE-5 | MTA-5 |
| 8 | UNT-8 | MTE-8 | MTA-8 |

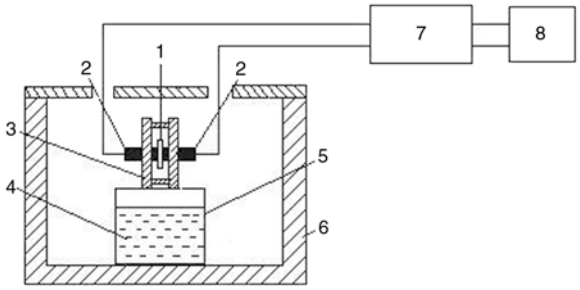

**Figure 2.** Schematic diagram of conductivity measurement device. 1 – membrane, 2 – electrode, 3 – insulator clamp, 4 – water, 5 – beaker, 6 – adiabatic groove, 7 – Solartron Instruments, 8 – computer

## 2.2. Proton conductivity measurements

The proton conductivity of membrane specimens in the traverse direction was measured in a measurement cell using AC electrochemical impedance spectroscopy (EIS), which was composed of a Solartron Instruments 1287 electrochemical interface and a Solartron Instruments 1255B frequency response analyzer (Farnborough, UK), both of which were interfaced via GPIB to a computer as shown in Figure 2. The EIS was recorded over a frequency range of 1–$10^6$ Hz, the amplitude of the sinusoidal modulation voltage was 10 mV, and the temperature ranged from 20 to 60°C. The membrane specimen in a beaker which contains temperature controller was clamped between two gold-plated copper electrodes (home-made, diameter 4.30 mm) with a constant pressure and relative humidity of about 75%. Before the test, all membrane specimens were soaked in deionized water for 24 h. The proton conductivity σ was calculated by Equation (1):

$$\sigma = \frac{l}{AR} \tag{1}$$

where σ [S·cm$^{-1}$] was the proton conductivity, $l$ [cm] and $A$ [cm$^2$] were the thickness and area of the membrane specimen, respectively, and $R$ [Ω] was derived from the high frequency intercepting with the real axis on a complex impedance plane plot.

## 2.3. Methanol permeability and water uptake

A group of different concentrations of methanol solution were prepared. 4.04 ml methanol (density 0.792 g·ml$^{-1}$) from Sinopharm Chemical Reagent Co., LtdS (Shanghai, China) and 95.96 ml deionized water were placed in 100 ml measuring flask to make a methanol solution with molar concentration of 1.00 mol·l$^{-1}$, and then the solution was kept in cryopreservation as a standard solution. Twelve different volumes varying from 25.0 µl to 0.600 ml, with an average increase of 25.0 µl, were drawn from the standard solution, and then placed in 25 ml measuring flask to obtain specific methanol solution with concentration from $1.00\cdot10^{-3}$ to $1.20\cdot10^{-2}$ mol·l$^{-1}$. The retention time and peak area were recorded after injecting 10.0 µl solution taken from the twelve samples in GC9800 gas chromatograph, Shanghai Kechuang GC Instrument Co., Ltd (Shanghai, China), immediately at room temperature, and each experiment was performed five times. The maximum relative error calculated from the average was less than 3.46%, demonstrating the peak area vs. methanol concentration curve could be applied to the quantitative analysis. The standard curve of the different concentration of methanol and the peak area is shown in Figure 3.

The methanol permeability coefficient was determined by a home-made diaphragm diffusion cell, which was identical to that described in [2], consisting of two half-cells separated by a membrane. 70 ml 5 M methanol solution was placed on one side of the diffusion cell and deionized water of the same volume was placed on the other side. Magnetic stirrers were used in both compartments to ensure uniformity. The peak areas were converted into methanol concentration in the compartment of deionized water with a reference to above-mentioned calibration curve in Figure 3. The methanol permeability coefficient $P$ [cm$^2$·s$^{-1}$] was calculated

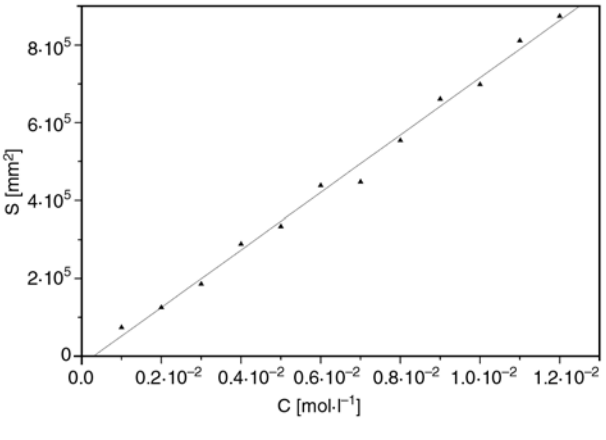

**Figure 3.** The curve of peak area versus methanol concentration

from the Equation (2) derived from the second law of Fick's diffusion:

$$P = \frac{sV_2 l}{AC_{10}} \qquad (2)$$

where $s$ [mol·l$^{-1}$·s$^{-1}$] was the slope of the straight-line plot of the methanol concentration versus permeation time, $V_2$ [ml] was the volume of deionized water, $l$ [cm] and $A$ [cm$^2$] were the thickness and area of membrane, respectively, $C_{10}$ [mol·l$^{-1}$] was the initial concentration of methanol solution. All membrane specimens were immersed in deionized water for 24 h before testing, and then the thickness and area of wet membranes were measured. Thereafter, the membrane specimens were stabilized at test temperature for more than 1 h, and then placed in diffusion cell for the measurement of methanol permeability.

The water uptake ($S_w$) of the membrane specimens was calculated by measuring the weight difference between the dry and hydrous membrane specimens [13]. The dried membrane specimens at 90°C for 24 h were weighed ($mass_{dry}$) and then immersed in deionized water for 24 h. Then the membranes were wiped with blotting paper to remove the surface water and quickly weighed ($mass_{wet}$) again. The $S_w$ was calculated with Equation (3):

$$S_w = \frac{mass_{vet} - mass_{dry}}{mass_{dry}} \cdot 100\% \qquad (3)$$

### 2.4. Structure of morphology

The surface and cross-section morphology of the membrane specimens were investigated by a scanning electron microscope HITACHI S-4800 (SEM) (Tokyo, Japan). The surface morphology was also studied by a scanning probe atomic force microscopy ZL AFM-III (AFM), Shanghai Zhuolun MicroMano Co., Ltd (Shanghai, China) in tapping mode. The surface of the membrane specimens was not pretreated while the cross-section of the membrane specimens was pretreated by freezing dry membrane in liquid nitrogen. The fresh cryogenic fracture of the membrane specimens was sputtered with a thin layer of Au in vacuum prior to SEM measurements.

Fourier Transform Infrared (FTIR) spectra of the dry membrane specimens were collected using a Nicolet-AVATAR380 FTIR, Thermo Nicolet Corporation (Madison, USA), spectrometer in frequency range of 300–2000 cm$^{-1}$. The specimens were prepared by making KBr pellets composed of polymer membrane.

X-ray diffraction (XRD) of the membrane specimens was carried out with a Rigaku D\max2550 (Akishima, Japan), using a Cu-Pd radiation and operated at 40 kV and 200 mA. The XRD patterns were collected with a scan rate of 7°·min$^{-1}$ in the range of from 10 to 70°. The small angle X-ray scattering (SAXS) experiments of membrane specimens were performed at a SAXS MAX 3000 (Rigaku) with CuK$_\alpha$ radiation, collected with a scan rate of 0.09°·min$^{-1}$ at room temperature. The explored $q$ was the range of 0–0.20 Å$^{-1}$ for SAXS measurement, where $q$ was the modulus of the scattering vector.

## 3. Results

### 3.1. Proton conductivity of membranes

Figures 4–7 are the curves of proton conductivity of pure SPEEK and polymer membranes with 2, 5, 8 wt% CeO$_2$ contents at 20–60°C and about 75% relative humidity, respectively. The conductivity of all membrane specimens increased with temperature and was higher than 10$^{-2}$ S·cm$^{-1}$, which is the lowest value for practical interest in fuel cell [13] when the temperature exceeded 40°C in Figure 4. The proton conductivity of specimens treated by high magnetic field increased obviously, and the MTE membrane specimens demonstrated better conductivity than the MTA ones. Compared with pure SPEEK membrane in Figure 4, the conductivity of polymer membranes decreased in Figure 5, which may be due to the introduction of CeO$_2$ into

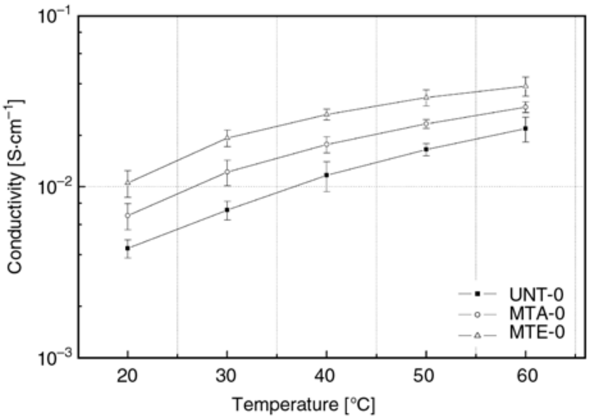

**Figure 4.** Conductivity of pure SPEEK membrane specimens as a function of temperature

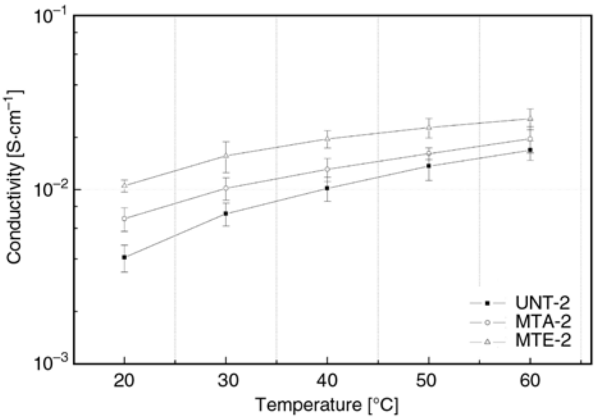

**Figure 5.** Conductivity of 2 wt.% $CeO_2$ membrane specimens as a function of temperature

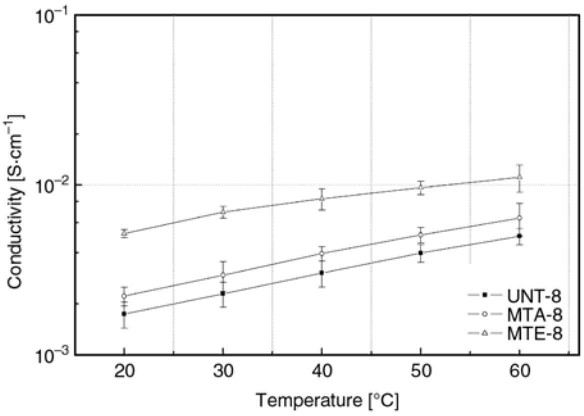

**Figure 7.** Conductivity of 8 wt.% $CeO_2$ membrane specimens as a function of temperature

the SPEEK matrix, resulting in reaction between the $CeO_2$ and the sulfonic groups in SPEEK. However, the conductivities of MTA-2 and MTE-2 were higher than that of the UNT-0 below 50°C. A probable reason was that the polar groups with treatment of high magnetic field played a role in enhancing the proton conduction. As shown in Figure 6, the conductivities of polymer membranes increased with temperature and showed the same tendency in Figure 4 or 5 though with slight improvement. The conductivities of the MTE-5 and MTA-5 within the test temperature both reached $10^{-2}$ S·cm$^{-1}$. The proton conductivity of MTA-8 was somewhat higher than that of UNT-8 but both of them failed to reach $10^{-2}$ S·cm$^{-1}$ in Figure 7. The conductivity of MTE-8 was improved dramatically, approaching $10^{-2}$ S·cm$^{-1}$ at 50°C and exceeding $10^{-2}$ S·cm$^{-1}$ at 60°C.

The test temperature was controlled up to 60°C because the relative error of the conductivities increased with temperature as a whole, particularly above 60°C. As shown in Figures 4–7, the conductivities of all membrane specimens improved with temperature, in particularly UNT-0, reaching $1.688\cdot10^{-2}$ S·cm$^{-1}$ at 60°C, which was five times higher than at 20°C. With $CeO_2$ doped in SPEEK matrix, the conductivities of polymer membranes decreased gradually. However, it was apparent that the conductivities of all membrane specimens remarkably increased after treatment of high magnetic field and were higher than $10^{-2}$ S·cm$^{-1}$ except MTA-8, which proved reorientation or deformation of the polar groups in membrane induced by magnetic field, facilitating the proton conduction. At the same time, it was found that the sensitivity of conductivity versus temperature was weakened with increasing $CeO_2$ contents.

### 3.2. Methanol permeability and water uptake

Figure 8 plots the fitted lines of methanol concentrations for various specimens against time in the compartment of the deionized water by gas chromatography based on the calibration curve shown

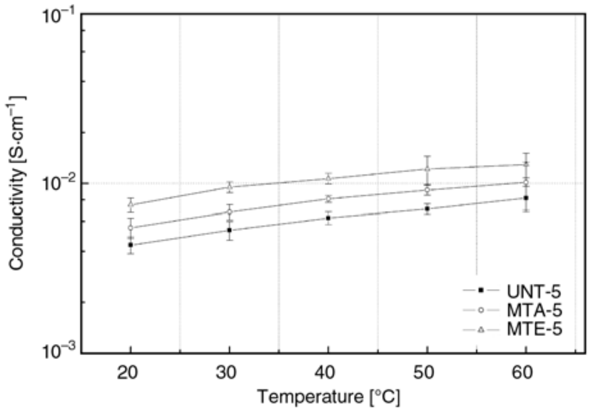

**Figure 6.** Conductivity of 5 wt.% $CeO_2$ membrane specimens as a function of temperature

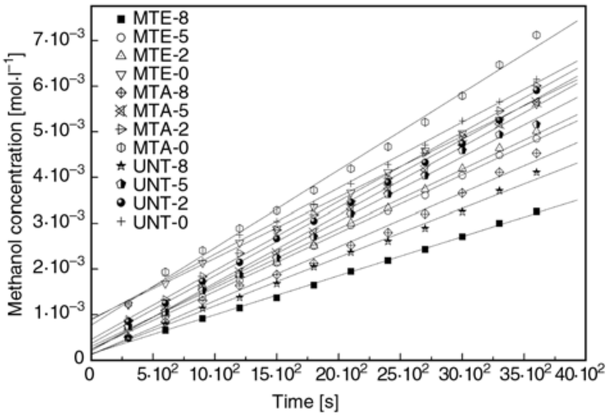

**Figure 8.** The relationship of methanol diffusion versus time at room temperature

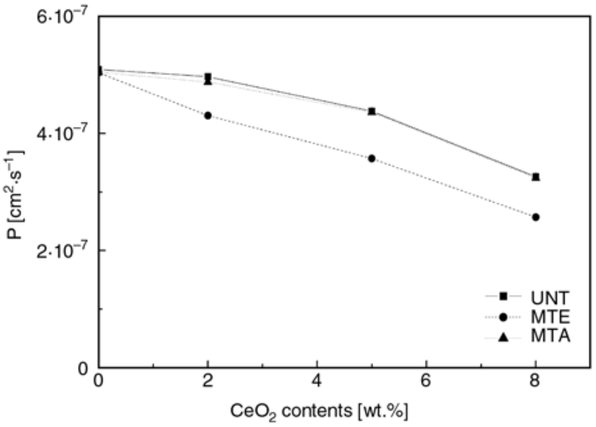

Figure 9. The curve of methanol permeation vs. contents of $CeO_2$

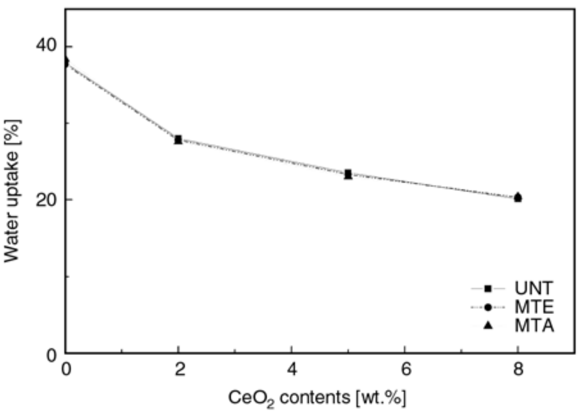

**Figure 10.** The curve of water uptake vs. CeO2 content

in Figure 3. The methanol permeability coefficient *P* was calculated by Equation (2).

Figure 9 shows the relationship of methanol permeability coefficient *P* versus the nanometer $CeO_2$ contents at room temperature. The coefficient of UNT-0 reached $5.092 \cdot 10^{-7}$ $cm^2 \cdot s^{-1}$, which was the highest in all tested specimens but an order of magnitude lower than that of the current commercial fluoride membrane. The methanol permeation resistance has not been influenced by magnetic field in the pure SPEEK membrane, but would increase with more $CeO_2$ doped in polymer membranes, which showed a tendency contrary to the proton conductivity. A possible reason of this is might be that $CeO_2$ reacts with sulfonic groups, decreasing obviously the methanol permeability as well as weakening somewhat the proton conductivity in the polymer membrane. The methanol permeation resistance of polymer membranes has not been influenced by parallel treatment with high magnetic field but was significantly influenced by perpendicular treatment. The main possible reason was that the polar groups were re-orientated or deformed by the magnetic field in parallel treatment, forming the polar network with a random distribution and enhancing the ordering characteristics, promoting the proton conductivity in some extent, but lowering the methanol resistance. After polymer membrane was treated with perpendicular magnetic field, the polar groups also went through the reorientation or deformation, resulting in similarly layered network with improved ordering characteristics. The ordered array of polar groups contributed to the proton conduction and the layered network structure further hindered the methanol diffusion in membrane, not only facilitated the proton conduction but also improved the performance of methanol resistance in membrane.

The water uptake of membranes changed with different $CeO_2$ contents, as shown in Figure 10. The water uptake of the polymer membranes as well as their proton conductivity in Figures 4–7 decreased with $CeO_2$ contents, opposite to their methanol permeability in Figure 9. This was because the amount of hydrophilic sulfonic groups decreased after being doped with alkaline $CeO_2$, resulting in smaller hydrophilic regions, or the proton conduction became restricted by the reaction between the $CeO_2$ and the sulfonic groups, leading to less protons involved in conduction. The water uptake has not been influenced by high magnetic field, which demonstrated the magnetic force only induced the reorientation or deformation but didn't change the amount of the polar groups in accordance with the theoretical expectations.

### 3.3. Structure of membrane

Figure 11 shows the AFM morphology of two dry membrane specimens, (a) MTA-2 and (b) UNT-5. The membrane surface has a nonporous structure, without cracks, groove marks or phase separation, indicating that it was smooth and compact. The nanometer $CeO_2$ was dispersed evenly but aggregation still could be observed, about 300 nm in size. With increasing $CeO_2$ contents, the membrane was denser with lower methanol permeability (as shown in Figure 9), decreased proton conductivity (Figures 4–7) and water uptake (Figure 10).

The typical specimens of UNT-0 and UNT-5 were chosen for the unobserved difference of the MT or

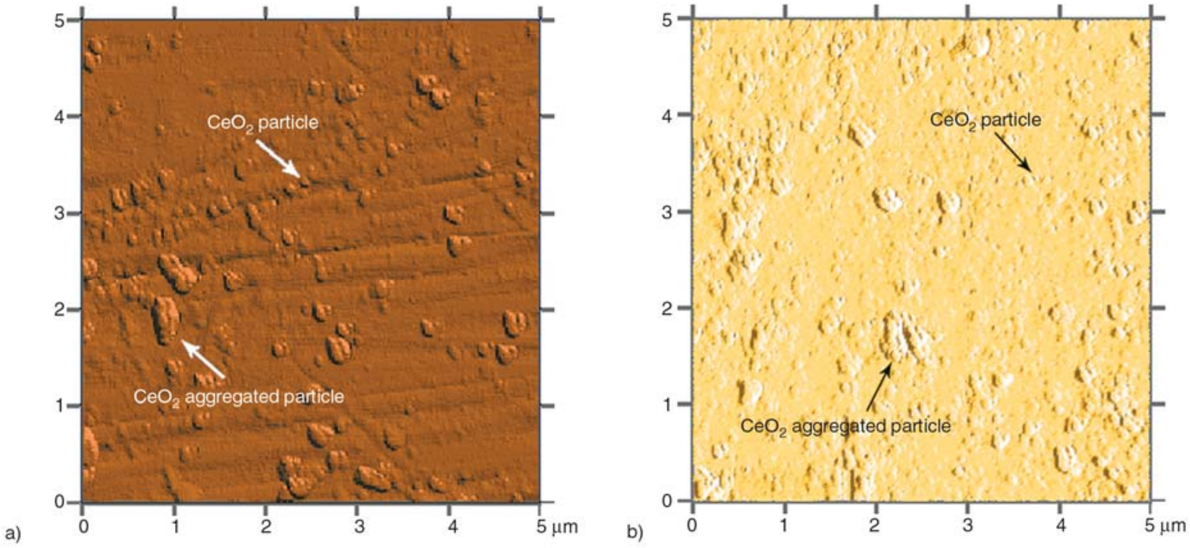

**Figure 11.** AFM of the MTA-2 (a) and UNT-5 (b) membrane specimens

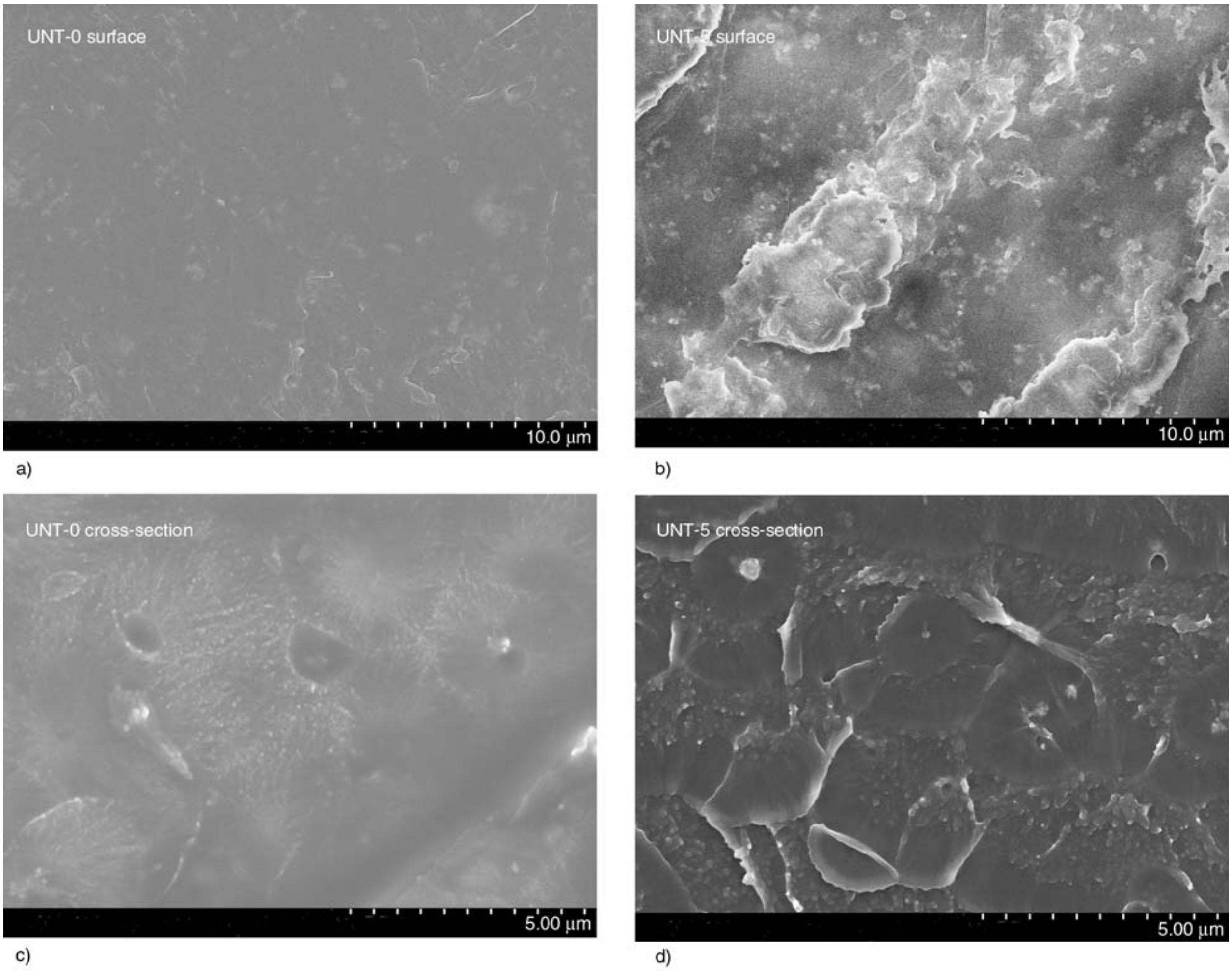

**Figure 12.** SEM of UNT-0 and UNT-5 membrane specimens surface (a, b) and cross-section (c, d)

UNT specimens. Figures 12a and 12b show the surface morphology of UNT-0 and UNT-5 membrane specimens. Some slight wales were observed on the surface of specimens. The surface was essentially smooth in UNT-0 but slight protrusions appeared in UNT-5, which were possibly formed during preparation of membrane. Cracks, flaws or phase separation were not observed in SEM micrographs, similar to the result in Figure 11b, illustrating the compact structure of the specimen.

Figures 12c and 12d show the cross-section of UNT-0 and UNT-5 membrane specimens, which were frozen by liquid nitrogen followed by gold sputtering. White neat border was observed in the fractures with unobvious contrast, illustrating the smooth cross-section and the amorphous structure of membranes. There was no mesh structure or phase separation, indicating that the membrane material was compact. But the holes in the UNT-0 specimen were some blowholes formed during preparation in SPEEK. Neither micro-phase separation nor meshes and pores was observed in UNT-5 specimen, which illustrated that the polymer membrane was more compact, resulting in higher methanol resistance. The agglomeration of nanometer $CeO_2$ was not observed in UNT-5, indicating its good dispersion in polymer membrane.

Figure 13 illustrates FTIR spectra of UNT-0 and UNT-5 dry membrane specimens. Two specific membrane specimens were chosen to compare their structures due to unobserved difference of the MT or UNT specimen in the FTIR spectra. The characteristic peaks at 1659–1638 and 1240 cm$^{-1}$ were attributed to stretching vibration of –Ar–C(=O)–Ar– and –Ar–O–Ar–, respectively. The O=S=O band at 1260 and 1080 cm$^{-1}$ were observed, corresponding to asymmetric and symmetric stretching vibration peaks, respectively. The characteristic peaks of $CeO_2$ appeared at 740 and 413 cm$^{-1}$, shifted from 700 and 400 cm$^{-1}$ reported in [14], proved the coordination occurred probably between cerium cation in the $CeO_2$ and oxygen anion in the sulfonic groups, enhancing the compact structure of membranes (Figures 11 and 12), decreasing the proton conductivity (Figures 4–7) and the methanol permeability (Figure 9).

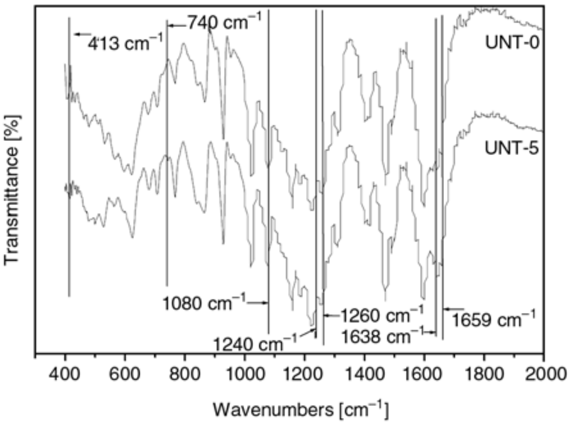

**Figure 13.** FTIR spectra of UNT-0 and UNT-5 membrane specimens

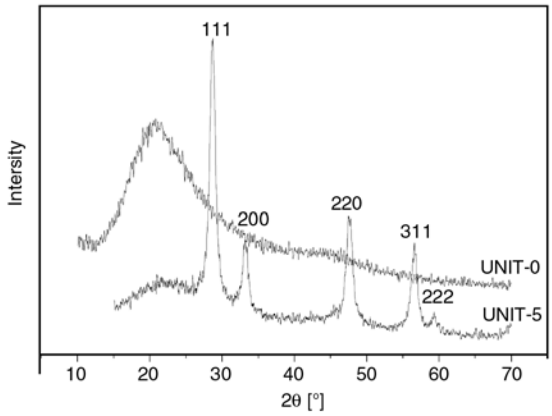

**Figure 14.** XRD pattern of UNT-0 and UNT-5 membrane specimens

The XRD patterns of UNT-0 and UNT-5 dry membrane specimens are shown in Figure 14. Similarly, the UNT-0 and UNT-5 specimens were chosen to demonstrate that there is no significant effect of the magnetic field on the XRD of the membranes. A typical amorphous diffraction peak could be observed in the UNT-0 specimen [15]. And the diffraction peaks at (111), (200), (220), (311) and (222) in UNT-5 specimen were corresponded with $CeO_2$ [16], which shows that coordination occurred only at the interface of the two pahses.

As shown in Figure 15, there were a uniform broad peak and a shoulder at 0.1679 and 0.1842 Å$^{-1}$ in composite membrane specimens, respectively. A broad peak at 0.1622 Å$^{-1}$ was observed but a shoulder disappeared in UNT-0 specimen. The peak in composite membrane specimens shifted towards larger *q*-value compared to the plain SPEEK membrane specimen, which demonstrated relatively smaller Bragg spacing 'center to center distance' between two clusters or crystallites in composite membrane specimens. A reason for this was that

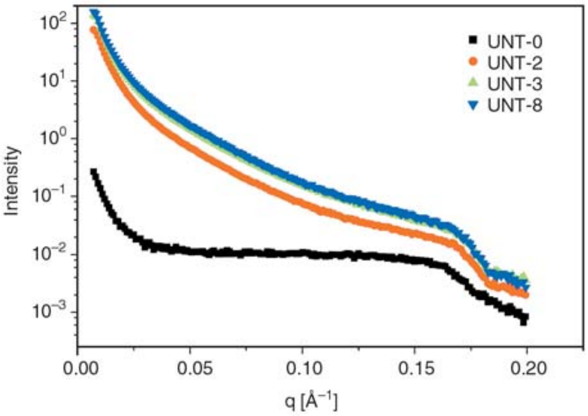

**Figure 15.** The small-angle X-ray scattering of specimens

sulfonic groups were statistically attached to main chain of SPEEK [17, 18] and the reaction occurred between $CeO_2$ and sulfonic groups, which increases the compatibility of organic-inorganic materials, thereby decreasing the proton conductivity and enhancing the methanol permeation resistance of specimens.

## 4. Discussions

There are two mechanisms for proton transport, one via hydrophilic sulfonic groups accompanied by the formation of $H_3O^+$ or $H_5O_2^+$ by the reaction of hydration in the hydrophilic regions, and the other is hopping between the adjacent hydrophilic sulfonic groups by $H^+$ activity. The hydrophilic groups attract water molecules in micro-aqueous phases formed after membrane hydration, increasing the size of hydrophilic regions, shortening the 'effective distance' between sulfonic groups, facilitating the proton transfer in two ways. With increasing temperature, the mobility of proton was enhanced, accelerating transportation between the sulfonic groups gathering in the hydrophilic regions. On the other hand, the water uptake decreased further with temperature, reducing hydrophilic regions in which proton transferred with $H_3O^+$ or $H_5O_2^+$ formation. However, the proton conductivity depended on both of them. Therefore, the curve of the conductivity was nonlinear and parabola-shaped, rising with temperature in Figures 4–7. After $CeO_2$ doping, the AFM of specimens showed that $CeO_2$ was dispersed evenly in Figure 11. The SEM also demonstrated the compact structure of the membranes with no crack or micro-phase separation observed in the images of Figure 12. The FTIR analysis displayed that the coordination occurred between cerium cation in $CeO_2$ and oxygen anion in sulfonic groups in Figure 13. The Bragg spacing of organic-inorganic materials was changed as shown in Figure 15, revealing the reaction between $CeO_2$ and sulfonic groups of SPEEK, decreasing the proton conductivity and methanol permeability, increasing the anti-swelling and mechanical property of polymer membrane, e.g. the methanol permeability of UNT-8 was about 64% and the proton conductivity was 23% of UNT-0 at 60°C, respectively.

It was obvious that the properties of membrane specimens have been influenced by high magnetic field. With appropriate temperature and time, sufficient energy was provided for the polar bonds to rearrange, in particular the ion bonds and the coordination bonds, and the different directions treatment of magnetic field made them to re-orient or deform under the Lorentz forces in certain directions. The high magnetic field with different directions would cause the electron cloud in the polar bonds especially ionic bonds or the coordination bonds to impose different effects on membranes. The change of the electronic cloud shape in polar bonds did not change the chemical structure of the SPEEK and the crystal structure of $CeO_2$, however, it had an effect on the proton conductivity and methanol permeability in polymer matrix, but no influence in water uptake for did not change the amount of the sulfonic groups, according to the micro-structural analysis of AFM, SEM, FTIR and XRD, shown above. According to the previous discussion of the reorientation or deformation to the MTE or MTA specimen, the layered network of the polar groups, especially the hydrophilic sulfonic acid groups, was more effective than the random network on properties like proton conductivity or methanol permeability, so the proton conductivity of the MTE was better than that of MTA, and the methanol resistance of the MTE was also effective in improving performance, e.g. the proton conductivity of MTE-8 at 60°C was 1.83 or 2.20 times of MTA-8 or UNT-8 specimen, respectively. The methanol permeability coefficient of the MTE-8 with $2.571\cdot10^{-7}$ $cm^2\cdot s^{-1}$ was about 79% of MTA-8, and also 79% for the UNT-8. The high magnetic field influenced the properties of the proton conductivity and methanol permeability, respectively, but the relevant characterization method has failed to find the mechanism of this impact which has yet to be further explored.

In this paper, the SPEEK with medium DS was chosen. The conductivity of all MTE membrane specimens reached $10^{-2}$ $S\cdot cm^2\cdot s^{-1}$, with good methanol resistance and water uptake property, the prepared MTE of polymer membrane specimen as PEMs in DMFC has a certain value.

## 5. Conclusions

The proton conductivity of the membrane specimen increased with temperature. In addition, the proton conductivity decreased but methanol resistance improved with doping $CeO_2$ contents in membrane specimen. It is worth noting that the proton conductivities of all membrane specimens treated with high magnetic field increased obviously, and the MTE membrane specimens demonstrated better conductivity than the MTA. The methanol permeability has been significantly influenced by the treatment with perpendicular high magnetic field. The water uptake of membrane specimens decreased with increasing amount of $CeO_2$, but remained at the same value after being treated with the magnetic field. The nanometer $CeO_2$ dispersed evenly in the SPEEK matrix, in which reaction occurred between the cerium cation in $CeO_2$ and oxygen anion in sulfonic group of SPEEK, enhancing the compatibility of polymer. The polymer membranes treated with perpendicular high magnetic field showed adequate proton conductivity, low methanol permeability, and good stability, having good potential for use in DMFC.

## Acknowledgements

The authors gratefully acknowledge Professor Han, C.C. (Institute of Chemistry, Chinese Academy of Sciences, Beijing, China) for the help in SAXS measurements.

## References

[1] Silva V. S., Ruffmann B., Vetter S., Boaventura M., Mendes A. M., Madeira L. M., Nunes S. P.: Mass transport of direct methanol fuel cell species in sulfonated poly(ether ether ketone) membranes. Electrochimica Acta, 51, 3699–3706 (2006).
DOI: 10.1016/j.electacta.2005.10.029

[2] Gil M., Ji X. L., Li X. F., Na H., Hampsey J. E., Lu Y. F.: Direct synthesis of sulfonated aromatic poly(ether ether ketone) proton exchange membranes for fuel cell applications. Journal of Membrane Science, **234**, 75–81(2004).
DOI: 10.1016/j.memsci.2003.12.021

[3] Rikukawa M., Sanui K.: Proton-conducting polymer electrolyte membranes based on hydrocarbon polymers. Progress in Polymer Science, **25**, 1463–1520 (2000).
DOI: 10.1016/S0079-6700(00)00032-0

[4] Zaidi S. M. J., Mikhailenko S. D., Robertson G. P., Guiver M. D., Kaliaguine S.: Proton conducting composite membranes from polyether ether ketone and heteropolyacids for fuel cell applications. Journal of Membrane Science, **173**, 17–34 (2000).
DOI: 10.1016/S0376-7388(00)00345-8

[5] Wilhelm F. G., Pünt I. G. M., van der Vegt N. F. A., Strathmann H., Wessling M.: Cation permeable membranes from blends of sulfonated poly(ether ether ketone) and poly(ether sulfone). Journal of Membrane Science, **199**, 167–176 (2002).
DOI: 10.1016/S0376-7388(01)00695-0

[6] Xing P. X., Robertson G. P., Guiver M. D., Mikhailenko S. D., Wang K. P., Kaliaguine S.: Synthesis and characterization of sulfonated poly(ether ether ketone) for proton exchange membranes. Journal of Membrane Science, **229**, 95–106 (2004).
DOI: 10.1016/j.memsci.2003.09.019

[7] Nunes S. P., Ruffmann B., Rikowski E., Vetter S., Richau K.: Inorganic modification of proton conductive polymer membranes for direct methanol fuel cells. Journal of Membrane Science, **203**, 215–225 (2002).
DOI: 10.1016/S0376-7388(02)00009-1

[8] Silva V. S., Ruffmann B., Silva H., Gallego Y. A., Mendes A., Madeira L. M., Nunes S. P.: Proton electrolyte membrane properties and direct methanol fuel cell performance I. Characterization of hybrid sulfonated poly(ether ether ketone)/zirconium oxide membranes. Journal of Power Sources, **140**, 34–40 (2005).
DOI: 10.1016/j.jpowsour.2004.08.004

[9] Chang J-H., Park J. H., Park G-G., Kim C-S., Park O. O.: Proton-conducting composite membranes derived from sulfonated hydrocarbon and inorganic materials. Journal of Power Sources, **124**, 18–25 (2003).
DOI: 10.1016/S0378-7753(03)00605-0

[10] Yu H. B., Kim J-H., Lee H-I., Scibioh M. A., Lee J. Y., Han J. H., Yoon S. P., Ha H. Y.: Development of nanophase $CeO_2$-Pt/C cathode catalyst for direct methanol fuel cell. Journal of Power Sources, **140**, 59–65 (2005).
DOI: 10.1016/j.jpowsour.2004.08.015

[11] Chang L-H., Sasirekha N., Chen Y-W., Wang W-J.: Preferential oxidation of CO in $H_2$ stream over $Au/MnO_2–CeO_2$ catalysts. Industrial and Engineering Chemistry Research, **45**, 4927–4935 (2006).
DOI: 10.1021/ie0514408

[12] Brijmohan S. B., Shaw M. T.: Magnetic ion-exchange nanoparticles and their application in proton exchange membranes. Journal of Membrane Science, **303**, 64–71 (2007).
DOI: 10.1016/j.memsci.2007.06.066

[13] Li X. F., Liu C. P., Xu D., Zhao C. J., Wang Z., Zhang G., Na H., Xing W.: Preparation and properties of sulfonated poly(ether ether ketone)s (SPEEK)/polypyrrole composite membranes for direct methanol fuel cells. Journal of Power Sources, **162**, 1–8 (2006).
DOI: 10.1016/j.jpowsour.2006.06.030

[14] McDevitt N. T., Baun W. L.: Infrared absorption study of metal oxides in the low frequency region (700–240 $cm^{-1}$). Spectrochimica Acta, **20**, 799–808 (1964).
DOI: 10.1016/0371-1951(64)80079-5

[15] Krishnan P., Park J-S., Kim C-S.: Preparation of proton-conducting sulfonated poly(ether ether ketone)/boron phosphate composite membranes by an in situ sol-gel process. Journal of Membrane Science, **279**, 220–229 (2006).
DOI: 10.1016/j.memsci.2005.12.010

[16] Gu H., Soucek M. D.: Preparation and characterization of monodisperse cerium oxide nanoparticles in hydrocarbon solvents. Chemistry of Materials, **19**, 1103–1110 (2007).
DOI: 10.1021/cm061332r

[17] Prado L. A. S. de A., Wittich H., Schulte K., Goerigk G., Garamus V. M., Willumeit R., Vetter S., Ruffmann B., Nunes S. P.: Anomalous small-angle X-ray scattering characterization of composites based on sulfonated poly(ether ether ketone), zirconium phosphates, and zirconium oxide. Journal of Polymer Science Part B: Polymer Physics, **42**, 567–575 (2003).
DOI: 10.1002/polb.10764

[18] Prado L. A. S. de A., Goerigk G., Ponce M. L., Garamus V. M., Wittich H., Willumeit R., Schulte K., Nunes S. P.: Characterization of proton-conducting organic-inorganic polymeric materials by ASAXS. Journal of Polymer Science Part B: Polymer Physics, **43**, 2981–2992(2005).
DOI: 10.1002/polb.20576